Dipl.-Ing. Markus Stütz, BSc, IWE

On the Welding Behavior of Molybdenum and Its Alloys

DOCTORAL THESIS

to achieve the university degree of

Doktor der technischen Wissenschaften

submitted to

Graz University of Technology

Supervisor

Assoc.Prof. Dipl.-Ing. Dr.techn. Norbert Enzinger

Institute of Materials Science, Joining and Forming

Graz, April 2019

Eidesstattliche Erklärung

Affidavit

Ich erkläre an Eides statt, dass ich die vorliegende Arbeit selbstständig verfasst, andere als die angegebenen Quellen/Hilfsmittel nicht benutzt, und die den benutzten Quellen wörtlich und inhaltlich entnommenen Stellen als solche kenntlich gemacht habe. Das in TUGRAZonline hochgeladene Textdokument ist mit der vorliegenden Doktorarbeit identisch.

I declare that I have authored this thesis independently that I have not used other than the declared sources/resources, and that I have explicitly indicated all material which has been quoted either literally or by content from the sources used. The text document uploaded to TUGRAZonline is identical to the present doctoral thesis.

Graz, _____ _____

Date Signature

In nichts zeigt sich der Mangel an mathematischer Bildung mehr, als in einer übertrieben genauen Rechnung.

— Carl Friedrich Gauss (disputed)

Preface

The present thesis was authored at the Institute of Materials Science, Joining and Forming (IMAT) at Graz University of Technology (TU Graz) and was submitted to the Faculty of Mechanical Engineering and Economic Sciences to achieve the academic degree *Doktor der technischen Wissenschaften (Doctor technicæ)*. The supervisor of the thesis was Assoc.Prof. Dipl.-Ing. Dr.techn. Norbert Enzinger.

The underlying project of the thesis was the *K-project Network of Excellence for Metal JOINing*, short JOIN, which was fostered in the frame of COMET – Competence Centers for Excellent Technologies by BMWFW, BMVIT, FFG, Land Oberösterreich, Land Steiermark, Land Tirol, and SFG. The program COMET was handled by FFG.

I want to thank my project partners and especially the colleagues at *Plansee SE*, *Klaus Raiser GmbH & Co. KG*, and *voestalpine Böhler Welding* for the support and the fruitful discussions over the past years during the project.

During my time at the institute, in the course of this thesis, and my life I was supported, guided, and accompanied by so many wonderful people that I can't possibly comprehend my gratitude in words. I just want to express to my supervisors, colleagues, Master and Bachelor students, to my friends, my family, and of course, to my girlfriend, a huge "Thank You!"

The further I went in my academic career, the more frequently the famos quote of the philosopher *Socrates* came to my mind, *"I know that I do not know."* Occasionally it seemed that for every question answered, three more arose. It occurred to me that in welding molybdenum and its alloys one is constantly fighting metallurgy, physics, and nature as such. However, contrary to E. M. Savitskii's claim that *"in the Soviet Union, the industrial production of molybdenum alloys has been mastered,"* [1] I believe that we can only strive for the better and it will always be a journey rather than reaching a destination. Looking back on the history of welding in the industrial age, I allege that welding of refractory metals is as far advanced as welding of conventional steel was a century ago. May this dissertation be a piece in the puzzle.

Abstract

In the production chain of semi-finished and finished products made of the refractory metal molybdenum and its alloys, welding can play an important role. However, due to metallurgical effects which cause an impairing of the mechanical–technological properties, welding is restricted to a few niche applications. In this work, investigations on the welding behavior of molybdenum and its alloys were led to broaden the applicability of the welding technologies rotary friction welding and electron beam welding.

Molybdenum and its alloys are prone to embrittlement by the re-distribution of precipitates and impurities to the grain boundaries during re-solidification and recrystallization. In the precipitation strengthened Mo-alloy TZM (Titanium–zirconium–molybdenum), these effects are partly reduced and the high temperature strength as well as the recrystallization temperature is raised considerably. In conventional fusion welding processes, melting and re-solidification occurs in the fusion zone as well as recrystallization takes place in the heat affected zone. This causes severe embrittlement which is typically observed in welded molybdenum specimens and discards them for industrial application.

In friction welding, no melting and high plastic deformation occurs in the bonding volume, which benefits the resulting microstructure of Mo and TZM. Experiments in Mo tubes in a heavy-duty rotary friction welding machine revealed a sudden and strong plasticization behavior, which consumed a large amount of drive power. The welding results were assessed by ultrasonic testing and microstructure characterization. To deepen the process mechanisms, laboratory-scale friction welding experiments of Mo and TZM rods were conducted in a friction stir welding machine. Process parameter interactions were studied thoroughly and the finished welds were characterized regarding microstructure and hardness. It was concluded that friction welding of Mo and TZM requires a special design of the process to obtain reproducible and successful welds. Finally, an attempt to numerically simulate the friction welding process was made and the results and shortcomings of the model were discussed.

Electron beam welding offered several benefits for the fusion welding of TZM, all above the available high specific energy input to minimize the usually occurring embrittlement effects in Mo and TZM during fusion welding. Experiments in 2 mm and 5 mm sheet metal were conducted and a parameter optimization study was done. The addition of filler metal into the weld offered possibilities of custom alloying the weld zone to improve the mechanical properties metallurgically. The microstructure was investigated by X-ray testing, light optical-, and scanning electron microscopy. The welds were further characterized by tensile strength and hardness lines. A reliable process for filler metal addition was developed and the effects of vanadium, vacuum arc cast TZM, and finally a novel cored wire filler were investigated. Especially with a cored filler wire, vast possibilities for future investigations arose.

Contents

1 Introduction

Refractory metals like molybdenum possess unique properties, like high melting point, creep resistance and preservation of their mechanical properties towards elevated temperatures [1]. For these reasons, they are highly attractive in high temperature applications in mechanical engineering [2, 3].

The majority of Mo is used as an alloying element in the production of various high-strength steels, as it narrows the austenite area, is able to build carbides, and enhances quenchability and corrosion resistance [4–6]. In contrast, only about 6% of molybdenum is processed into base material [7]. Mo and its alloys are used in furnace and glass melting components, power semiconductor heat sinks, sputtering targets, isothermal forging dies, injection molding tooling, X-ray targets, and metalworking tools, among others. In the lighting industry, molybdenum parts serve supportive purposes of lighting filaments and reflectors of halogen lamps [3,8]. Figure 1.1 shows two examples of Mo-based products. Molybdenum also serves diverse tasks in nuclear technology; in fission reactors as cooling elements [9] and in probe fusion reactors as divertors [10]. Further, molybdenum coatings are in commercial application for example as lubricity layer and abrasion protection coating of piston rings [3, 11].

In the processing of molybdenum, welding is of major interest. Unfortunately, the high thermal conductivity, the lack of lattice transformation which makes a grain refinement by newly built grains during transformation impossible, and the agglomeration of impurities on the grain boundaries lead to a severe embrittlement of the welds [1]. Molybdenum–rhenium alloys show a satisfactory weldability, although these alloys are too cost intensive due to rhenium's high raw price [13].

With distinct process parameters and heat treatment of pure molybdenum and the widespread titanium–zirconium–molybdenum alloy TZM, the negative effects of welding can be reduced, but have not yet been eliminated entirely [13, 14]. Therefore, a deeper investigation of different welding technologies for molybdenum, the interaction of process parameters, and the underlying metallurgical and physical phenomena is required.

(a) (b)

Figure 1.1: Examples for molybdenum applications: (a) Rotating X-ray anode and (b) hot zone crucibles [12]

1.1 K-Project Network of Excellence for Metal JOINing (JOIN)

Joining and especially welding of metals is considered a key technology in Austria. For this reason, the Institute of Materials Science, Joining and Forming (IMAT) of TU Graz collaborated with numerous industrial companies to advance the technology of welding in a number of fields and applications. The project metal JOINing was originated as a follow-up to the two previous projects JOIN and JOIN4+, continuing some research fields and emerging new aspects, welding technologies, and new materials as well. The aim was to understand joining processes and the respective material behavior in more detail for improved production processes and more sophisticated industrial products. The Österreichische Forschungsgesellschaft FFG granted financial support for the project metal JOINing over the course of four years (September 2014 to August 2018) which enabled the planned comprehensive research in the field of welding. The project metal JOINing is branched in two main areas; Area 1: "Materials" and Area 2: "Processes," which are both sub-divided into several projects [15].

1.2 Advanced Welding Technologies for Molybdenum and its Alloys (MOLY)

Project 1.1 of Area 1 "Materials" concerns the welding of molybdenum and its alloys. In numerous applications, successful welding increases the attractiveness for Mo products. The driving idea was to investigate and further the weldability of two main molybdenum semi-finished products:

1. **Mo tubes** are used as sputter targets in the coating of solar cell panels and flat screens. Due to the sintering process route, these tubular parts are limited in dimension and therefore the idea is to join them via welding to produce a larger scale of targets without the need of a flange joint.

2. Crucibles and furnace equipment as well as other products made from **TZM sheets** are in industrial application. If welded rather than conventionally joined by mechanical fixation or brazing, more flexible designs and lower production cost are possible for these products.

Joining by welding of molybdenum and its alloys was proven possible but not without comprising a number of difficulties: In solid state welding, good material properties were achieved, but fundamental knowledge of the interaction of welding parameters which yield the final weld quality were not yet established. In fusion welding, the main issue was grain coarsening accompanied by a re-distribution of impurities on the grain boundaries. The result was insufficient ductility and strength [15].

1.2.1 Motivation

To address the above mentioned issues, the project MOLY consists of two main work packages. For tubular formats, rotary friction welding was the obvious choice, while power beam welding processes seemed more practical for sheet base metal:

1. In rotary friction welding, some problematic issues are avoided since this welding process operates below the melting point of the involved metals. Based on reference parameters in the literature [7,14] and preliminary experiments [16], a parameter study and a simulation of the process is conducted. Moreover, heat treatment procedures prior and after the welding process are included in the research.

2. In the process of power beam welding, the melting of the base material results from a laser beam (LBW) or an electron beam (EBW). On account of the high energy densities of laser- and electron beam welding it is possible to fuse molybdenum and its alloys, however, accompanied by a decline of the weld's mechanical properties [17]. Therefore, evaluating the influence by alloying elements and elaboration of different filler materials are the main focus of this research package.

1.2.2 Objectives

The project MOLY addresses two welding techniques, their influencing parameters are identified and the metallurgical activity of the material is described. Supported by statistical design and analysis of experiment, the following goals are pursued:

1. Deepening of the knowledge about welding technologies of molybdenum
2. Improvement of the mechanical properties of molybdenum-based weld designs
3. Development of a suitable welding filler material for fusion welding of molybdenum

With these defined tasks and distinct goals, new knowledge shall be generated which contributes to the ongoing development of joining technologies of molybdenum.

1.2.3 Academic output

In the course of the project MOLY a series of academic work emerged, including the present dissertation. The following list compiles all Bachelor's and Master's theses, international conference contributions, and journal publications.

1.2.3.1 Supervised and co-supervised Bachelor's theses

- Christian Voglreiter, *Einbringung von Zusatzwerkstoffen für das Elektronenstrahlschweißen von Kupfer*, 2015.
- Christian Helmreich, *Implementierung und Evaluierung eines Rotationsreibschweißprozesses in ABAQUS*, 2016.
- David Oblak, *Simulation eines Rotationsreibschweißprozesses mittels DEFORM*, 2016.
- Adrian Aumayr, *Charakterisierung von EBW-Kupferschweißnähten mit Zusatzwerkstoff Zinn*, 2016.
- Maximilian Meisterl, *Elektronenstrahlschweißen von 5 mm Blechen aus TZM mit und ohne Schweißzusatz*, 2018.
- Simon Elmiger, *Erprobung eines Mo-Fülldrahtes für das Elektronenstrahlschweißen von TZM-Blechen*, in progress.

1.2.3.2 Supervised Master's theses

- Diogo Brízido Caldas Oliveira, *Electron Beam Welding of TZM Plates*, 2015.
- Johann Sebastian Kramer, *Elektronenstrahlschweißen von TZM mit Schweißzusatz*, 2017.
- Florian Kogler, *Simulation eines Rotationsreibschweißprozesses*, 2018.
- Florian Pixner, *Rotary Friction Welding (RFW) of Molybdenum*, 2018.

1.2.3.3 Conference contributions

- M. Stuetz, D. Oliveira, M. Ruettinger, N. Reheis, H. Kestler, N. Enzinger. *Electron Beam Welding of TZM Sheets*, Thermec Intl. Conf., Graz, Austria, June 2016.

- M. Stuetz, J. Wagner, N. Reheis, H. Kestler, E. Raiser, N. Enzinger. *Rotary Friction Welding of Large Molybdenum Tubes*, Intl. Conf. on Trends in Welding Research, Tokyo, Japan, October 2016.

- F. Pixner, M. Stuetz, J. Wagner, N. Reheis, N. Enzinger. *Vergleichende Rotationsreibschweißversuche mit Molybdän und Stahl auf einer FSW-Anlage*, SLV Reibschweißtagung, Munich, Germany, March 2017.

- M. Stuetz, F. Pixner, J. Wagner, N. Reheis, E. Raiser, H. Kestler, N. Enzinger. *Rotary Friction Welding of Molybdenum Components*, 19$^{\text{th}}$ Plansee Seminar, Reutte, Austria, June 2017.

- J. S. Kramer, M. Stuetz, M. Ruettinger, M. Koegl, N. Reheis, H. Kestler, N. Enzinger. *Enabling TZM Sheet Welds by Proper Filler Metal Addition*, EUROMAT Intl. Conf., Thessaloniki, Greece, September 2017.

- M. Stuetz, M. Meisterl, M. Ruettinger, N. Reheis, T. Woehry, T. Willidal, N. Enzinger, C. Sommitsch. *Advanced Electron Beam Welding of TZM Sheets Using Filler Metal*, 64. Metallkunde-Kolloquium, Lech am Arlberg, Austria, April 2018.

- R. Buzolin, M. Stuetz, F. Pixner, C. Poletti, N. Enzinger, C. Sommitsch. *Advanced Characterization of Friction Welded Molybdenum and TZM Alloy*, 15. Internationale Metallographie Tagung, Leoben, Austria, September 2018.

- M. Stuetz, F. Kogler, J. Wagner, K.-H. Leitz, N. Reheis, N. Enzinger. *Numerical Simulation of Rotary Friction Welding of Molybdenum*, 12$^{\text{th}}$ International Seminar Numerical Analysis of Weldability, Seggau, Austria, September 2018.

1.2.3.4 Journal publications

- M. Stuetz, D. Oliveira, M. Ruettinger, N. Reheis, H. Kestler, N. Enzinger. *Electron beam welding of TZM sheets*, Materials Science Forum 879, pp. 1865–1869, 2016.

- M. Stuetz, F. Pixner, J. Wagner, N. Reheis, E. Raiser, H. Kestler, N. Enzinger. *Rotary friction welding of molybdenum components*, Intl. J. of Refractory Metals & Hard Materials 73, pp. 79–84, 2018.

- M. Stuetz, R. Buzolin, F. Pixner, C. Poletti, N. Enzinger. *Microstructure development of molybdenum during rotary friction welding*, Materials Characterization 151, pp. 506–518, 2019.

- F. Kogler, M. Stuetz, J. Wagner, K.-H. Leitz, N. Reheis, N. Enzinger, *Finite Elemente Simulation des Rotationsreibschweißens von TZM*, accepted.

1.2.4 Outline

The present dissertation is arranged in three main parts: First, an introduction to refractory metals with the focus on molybdenum is given and investigations concerning the flow stress behavior of pure Mo are discussed. The second part concerns friction welding and in more detail rotary friction welding of pure molybdenum and TZM, the problems that occurred, and possible solutions are presented. Third, fusion welding by the means of electron beam welding in TZM sheets is presented and experiments with different filler metals to improve the mechanical properties are investigated.

2 Molybdenum

In this chapter, molybdenum and the titanium–zirconium–molybdenum (TZM) alloy are discussed in detail. The unique characteristics of refractory metals are elaborated, recovery and recrystallization as well as hardening mechanisms are explained, and experiments concerning the flow stress behavior at different temperatures and strain rates are presented. A possible modeling of the flow stress concludes this chapter.

2.1 State of the art

2.1.1 Refractory metals

The definition of refractory metals varies throughout the literature. In general, refractory metals are considered metals with an elevated melting point and which sustain their mechanical properties at higher temperatures [1, 2, 18]. They are transition elements, situated in the groups 4 to 10 in the periodic table.

Figure 2.1 shows the melting point of transition metals in relation to their position in the periodic table. It is observed that the melting points of the elements of the periods 5 and 6 reach a maximum at the elements of group 6, being Mo and W, with an atomic configuration of six electrons in the outer shells [1]. All elements with a melting temperature above 2,000°C are listed in table 2.1.

Table 2.1: List of refractory metals and their melting points [1, 4]

Chemical symbol	Name	Melting point °C
Tc	Technetium	2,172
Hf	Hafnium	2,222
Ru	Ruthenium	2,250
Ir	Iridium	2,445
Nb	Niobium	2,468
Mo	Molybdenum	2,610
Ta	Tantalum	3,000
Os	Osmium	3,045
Re	Rhenium	3,180
W	Tungsten	3,380

Among the refractory metals of table 2.1, only four are in wide commercial use: Niobium, molybdenum, tantalum, and tungsten [1, 2].

2.1.1.1 Density

In general, refractory metals possess a high density, with osmium being the densest metal in the periodic table (22.6 $^{g}/_{cm^2}$). Remarkable therefore is molybdenum's low density of 10.22 $^{g}/_{cm^2}$—

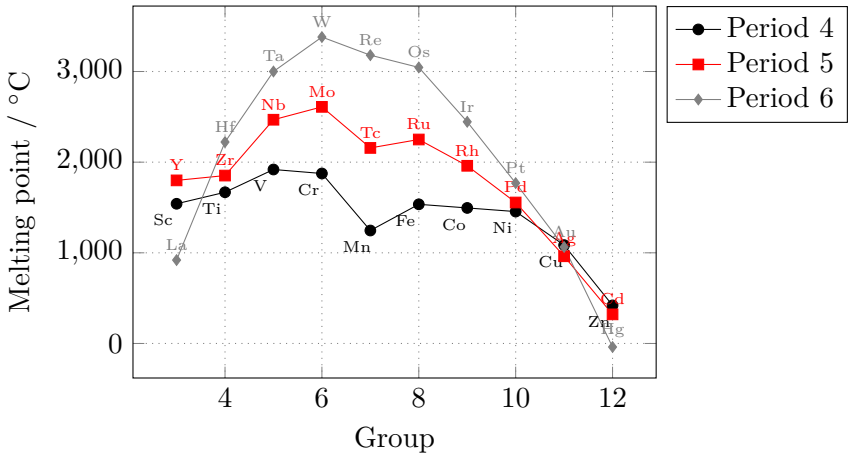

Figure 2.1: Melting points vs. periodic table position of metals from groups 3–12 [1, 4]

compared to tungsten's 19.25 g/cm^2, it only accounts to about half the specific weight, with solely niobium being lighter at 8.57 g/cm^2 [1, 4].

2.1.1.2 Crystal lattice

The elements of group 6 (Cr, Mo, W) have a body-centered cubic (bcc) lattice and are monomorphic. Bcc structures are less ductile than face-centered cubic (fcc) lattices, as they have fewer slip systems and only one slip direction in <111> [19] and resist dislocation movements better [20]. The lack of lattice transformation means it cannot be hardened by martensitic transformation and substantial grain growth takes place at high temperatures and during solidification [1, 4].

2.1.1.3 Thermodynamics

As per definition, the melting and boiling points of refractory metals are high. Tungsten has the lowest vapor pressure among refractory metals [21]. Tantalum's and molybdenum's is also low compared to chromium. Figure 2.2 shows the vapor pressure of refractory metals in dependence of the temperature in vacuum.

In general, the specific heat increases with increasing temperature. Especially molybdenum increases steeper than the other metals [1].

2.1.1.4 Thermal expansion

Refractory metals stand out with their low coefficients of thermal expansion (α), with tungsten having the lowest. Table 2.2 shows a comparison between Al, Fe, and refractory metals. A correlation between the melting point and α is observed. α also depends highly on the degree of purity, traces of impurities increase α drastically [1].

2.1.1.5 Mechanical properties

In general, metals with a cubic lattice show a better workability than hexagonal lattice. Molybdenum and niobium preserve their specific mechanical strength better than tantalum and tungsten up to 1,370°C, as depicted in figure 2.3. Mo, W, Re, and Os also keep their hardness close to their melting points [1].

Table 2.2: Coefficient of thermal expansion α of selected elements at room temperature [1]

Element	α $10^{-6}\,\mathrm{K}^{-1}$
Al	23.1
Fe	11.8
Ti	8.35
Nb	7.1
Ta	6.3
Mo	4.98
W	4.59

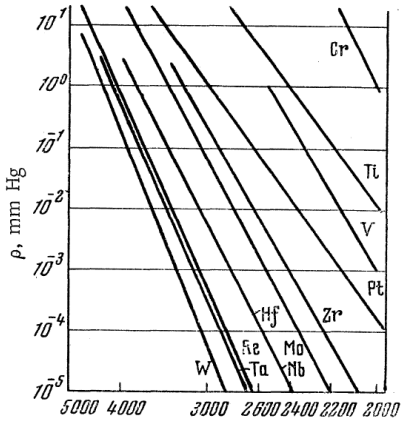

Figure 2.2: Vapor pressure in dependence of temperature in vacuum [1]

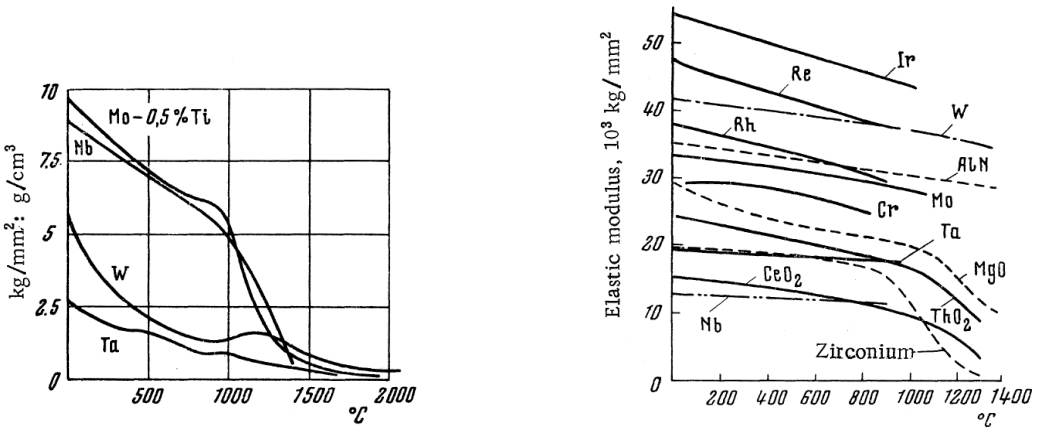

(a) (b)

Figure 2.3: (a) Specific strength of Nb, W, and Ta compared to a Mo–0.5%Ti alloy and (b) course of the modulus of elasticity of refractory metals and selected materials over temperature [1]

2.1.2 Molybdenum

Pure molybdenum was first successfully produced in 1782 by reducing molybdenum trioxide (MoO_3), which was priorly obtained from molybdenite (MoS_2), by K. W. Scheele in 1778. Initially, molybdenite was mistaken for blue lead (PbS), hence the name "*μολυβδος*" ("*molybdos*"), which is greek for lead [4]. Table 2.3 lists the most important physical and mechanical properties of pure molybdenum metal in untreated condition.

Table 2.3: Physical and mechanical properties of Mo in untreated condition [1, 4]

Crystal structure	bcc
Density	10.28 $^{g}/_{cm^3}$
Melting point	2,620°C (1 bar)
Boiling point	4,825°C (1 bar)
Thermal conductivity (20°C)	138 $^{W}/_{m\,K}$
Specific heat capacity (20°C)	254 $^{J}/_{kg\,K}$
Young's modulus (20°C)	329 GPa
Ultimate tensile strength	324 MPa
Fracture elongation	10-15%

2.1.2.1 Recrystallization

Refractory metals possess a high recrystallization temperature due to their strong inter-atomic bond. Figure 2.4 depicts recrystallization diagrams of molybdenum. It is observed that in Mo produced by vacuum arc casting (VAC), recrystallization does not commence below 1,300°C, regardless of the degree of deformation. In powder metallurgically (PM) produced Mo the threshold temperature is around 1,000°C. Typically, a critical degree of deformation in the magnitude of 5–20% is characteristic in all metals, at which a substantial grain growth is observed. As observed in figure 2.4, the critical degree of deformation is 7.5% for VAC Mo [1] and around 5%

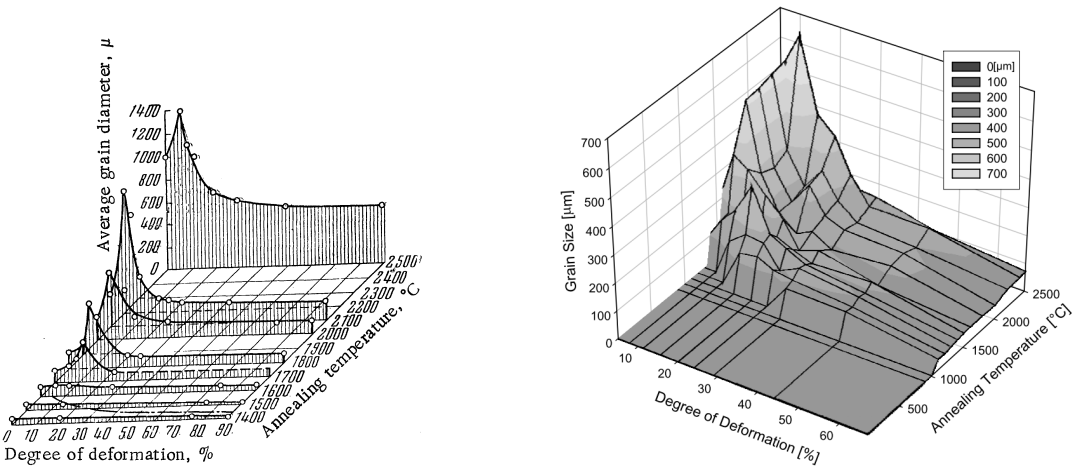

(a) (b)

Figure 2.4: Recrystallization diagrams of molybdenum: (a) vacuum arc cast Mo [1] and (b) powder metallurgically produced Mo [22]

for PM Mo [22].

In theory, the recrystallization of a metal causes a reduction in strength along with an increase in plasticity. However, recrystallization annealing of chromium, molybdenum, and tungsten leads to an embrittlement due to the re-distribution and the resulting precipitations of impurities on the grain boundaries. Smaller grains increase the total length of grain boundaries, which dilutes the precipitation amount on the latter, thus increasing the mechanical properties [19,20]. Similarly, a high purity of refractory metals results in an increased plasticity of recrystallized materialF [1].

Mo possesses a high stacking fault energy of 0.3 $^{J}/_{m^2}$ [23, 24], in general recovery processes dominate recrystallization processes [25]. Primig et al. assumed that recrystallization nucleated by the coalescence of recovered subgrain regions [22]. After extensive investigation of the recovery and recrystallization behavior of commercially pure Mo, Primig formulated a summary of her findings (table 2.4) [19].

Table 2.4: Main results of recrystallization behavior of pure Mo by Primig [19]. LD stands for loading direction.

deformation temperature	cold deformation T_R	warm deformation $< 0.5 \cdot T_M$	hot deformation $> 0.5 \cdot T_M$
level of dynamic recovery	no dynamic recovery	moderate	strong
deformation texture	strong <111>//LD 2nd strong <001>//LD weak <others>//LD	strong <111>//LD 2nd <001>//LD weak <others>//LD	*if* $\varphi > 0.5$ *and* $\mathrm{d}\varphi/\mathrm{d}t = 1$ strong <001>//LD 2nd strong <001>//LD weak <others>//LD
predominant nucleation of recrystallization mechanism	nucleation of <111>//LD via extended recovery (subgrain growth and coalescence)	successful nucleation and growth of <others>//LD due to absence of orientation pinning; moderate success of <111>//LD and <001>//LD	nucleation of <001>//LD via strain induced boundary migration
annealing texture	strong <111>//LD moderate <001>//LD weak <others>//LD	volume fraction of <others>//LD increased moderate <111>//LD moderate <001>//LD	strong <111>//LD weak <111>//LD weak <others>//LD

2.1.2.2 Mechanical properties

Brosse et al. [26] conducted bending tests of high purity Mo samples and investigated the fracture surfaces by Auger electron spectroscopy (AES) and scanning electron microscopy (SEM). They found no precipitates and argued that the intergranular brittleness of Mo is an intrinsic property of Mo. D. Stein [27] as well found that a higher purity level of single crystal Mo did not increase the ductility.

The progression of various tensile properties of Mo can be observed in figure 2.5. The ductile–brittle transition temperature (DBTT) may be specified according to the total reduction in area. Taking into account the variation in the literature [3, 12, 28], the DBTT is given between 0°C and 200°C. Figure 2.6 shows the results from a three point bend tests to illustrate the DBTT.

Mechanical deformation like rolling or forging, above all, strengthens molybdenum alloys up to a factor of four. Annealing on the other hand reverts the strengthening effect, due to the

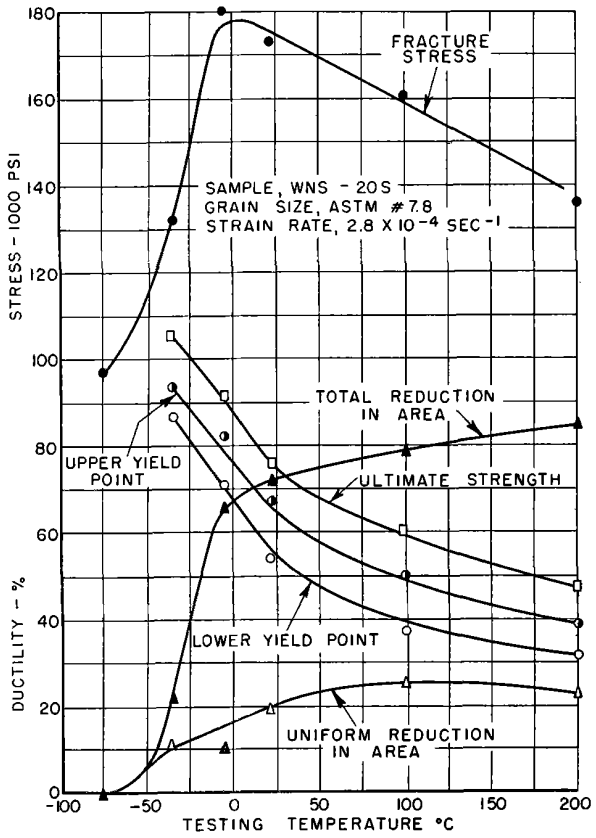

Figure 2.5: Tensile properties of molybdenum depending on the temperature [28]

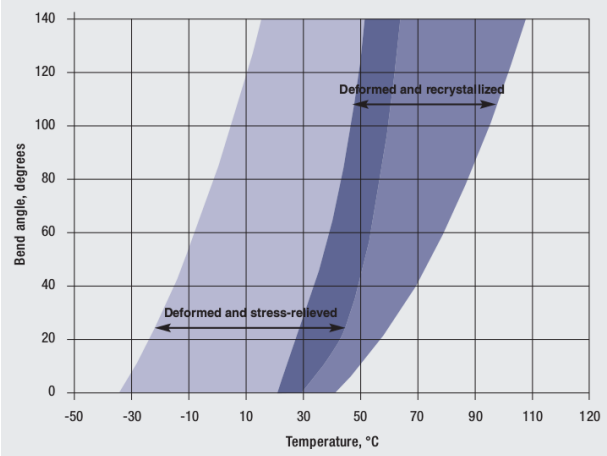

Figure 2.6: DBTT behavior of Mo sheet metal in deformed and stress-relieved condition and deformed and recrystallized resulting from a three point bend test [3]

negative effect of re-distribution of impurities on the grain boundaries by recrystallization, as discussed before [1, 3].

Figure 2.7 shows the evolution of the hardness in relation to the annealing temperature and the prior deformation state [22]. First, it is observed that the higher the deformation, the higher the initial hardness of the material. Depending on the deformation state, a hardness drop is

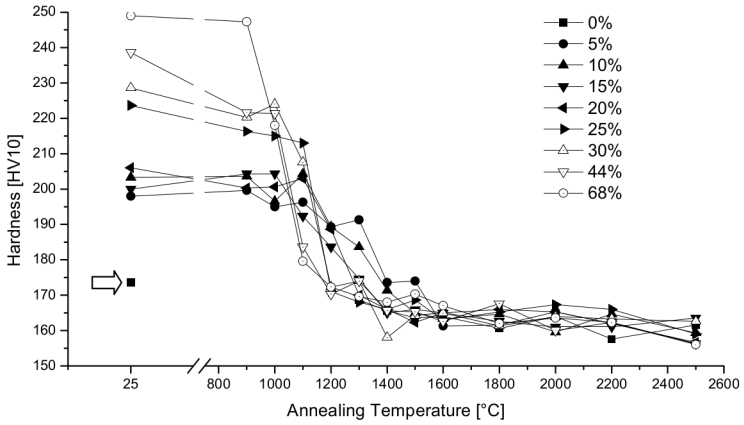

Figure 2.7: Resulting hardness of different deformation states after annealing. It is observed that depending on deformation state, between 1,000 and 1,400°C the hardness drops to a similar level [22].

observed between 1,000°C and 1,400°C, where eventually the hardness reaches the level of the undeformed state.

2.1.2.3 Chemical properties and corrosion

Oxygen and nitrogen cause embrittlement by segregations and precipitations along grain boundaries. Carbon segregation, on the other hand, has the opposite effect and increases the grain cohesion. Therefore, it is suggested that the heat induced embrittlement can be opposed to by improving the intergranular bonding [17].

Molybdenum is resistant to corrosion in atmosphere with a humidity below 60% at room temperature [12]. Both fresh-, and sea water do not cause remarkable corrosion, however, molybdenum's resistance to water drops significantly as the temperature exceeds 260°C [9]. Furthermore, Mo reacts instable in aqueous alkaline and oxidizing solutions [3].

Refractory metals in general are prone to oxidation at elevated temperatures. Molybdenum and tungsten produce highly volatile oxides which result in substantial material loss. Exposed to the atmosphere, Mo and Mo-based alloys experience an accelerated oxidation from about 550°C onwards and form MoO_3 which subsequently sublimates [3, 8, 9].

Molybdenum resists hydrogen, argon, and helium atmospheres without any effect, and nitrogen and carbon dioxide exposure up to 1,100°C [9].

2.1.2.4 Precipitation strengthening mechanisms

It is well established that oxygen (O) in small amounts of a few ppm has a strongly negative impact on most refractory metals, especially on W and Mo. Oxygen segregates to the grain boundaries and lowers the binding energy which leads to a tendency of intergranular fracture [1, 13, 20]. To countervail this effect, two strategies are possible: (1) the addition of elements that sufficiently bind oxygen, and (2) to prevent the re-location of O to the grain boundaries [20].

To address the first point, zirconium is added to the Mo matrix. Due to Zr's high affinity to oxygen, ZrO_2 is formed in particles of up to 10 µm in size. These particles are easily observed in light optical microscopy (LOM) and scanning electron microscopy (SEM) images as for example in figure 2.8 [29].

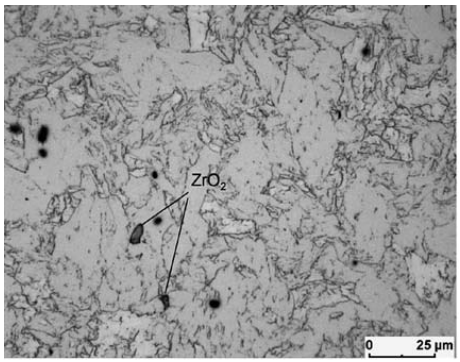

Figure 2.8: ZrO_2 particles observed by SEM in a TZM material [29]

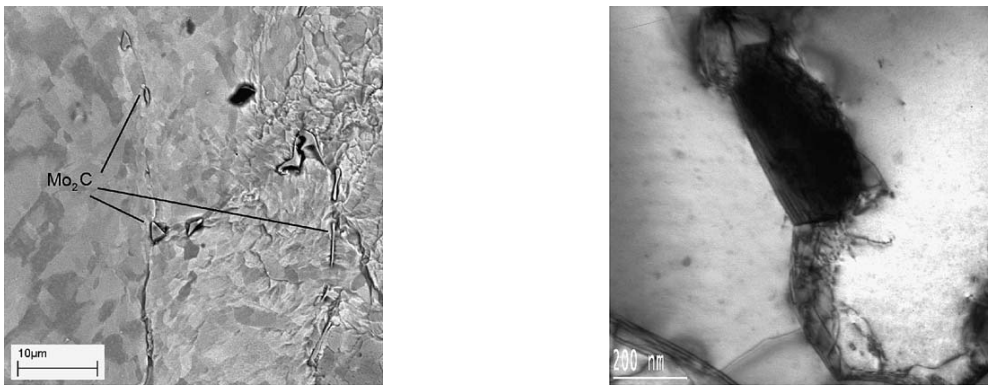

(a) (b)

Figure 2.9: TEM images of (a) Mo_2C and (b) $(Mo,Ti)_xC_y$ [29]

Concerning the second point, carbon (C) is reported to be very effective in inhibiting O from relocating to the grain boundaries by reducing the segregation driving force and by trapping O atoms in the bulk material [30,31]. Carbon forms Mo_2C and $(Mo,Ti)_xC_y$ particles which usually segregate on the grain boundaries. Their size is below 1 µm as observed in figure 2.9 [29]. By pinning the grain- and subgrain boundaries and thus hindering the movement of dislocations, the small precipitates increase the recrystallization temperature of Mo up to 1,500°C [3, 12, 29, 32].

The role of boron is also to inhibit oxide formations on grain boundaries [13, 33, 34] and is accounted an effect of increasing the grain boundary cohesion [35,36]. An atom probe investigation showed that Zr, C, and also B hinder O to segregate on GBs, as observed in figure 2.10 [33].

By a series of segregation kinetics simulations, Scheiber et al. [37] demonstrated that not only the amount of impurities but also the cooling rate has direct influence on the amount of elements segregated on the grain boundaries. They described the empirical equation $T(t) = T_0 \cdot e^{-r\sqrt{t}}$ with the characteristic cooling constant r in $s^{-1/2}$. It is shown that at low cooling constants the segregation depends mostly on the affinity of the single elements to grain boundaries, with O dominating C [38]. A high cooling constant, however, forces a ratio more towards the absolute content of elements [37]. Figure 2.11 depicts this tendency assuming bulk Mo with 100 ppm C and 20 ppm O.

Apart from former grain boundaries and coalesced, recovered subgrains, Silva et al. observed recrystallization in the molybdenum alloy MZ17 (Mo matrix with 1.7 wt.% ZrO_2) as an effect of particle stimulated recrystallization [39]. Hereby, particles induce large misorientation gradients in the deformed material which act as initiation sites for recrystallization [40, 41]. Given that

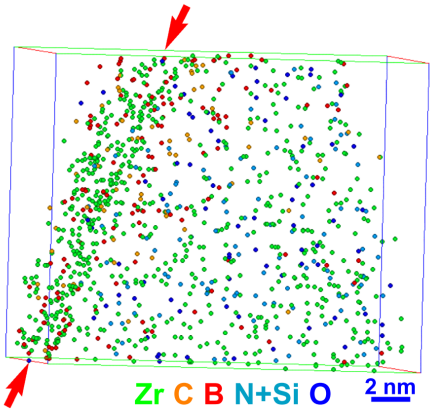

Figure 2.10: Atom probe investigation of a grain boundary of Mo (indicated by red arrows) alloyed with C, B, and Zr [33]. It is observed that oxygen is repressed at the GBs by the alloying elements.

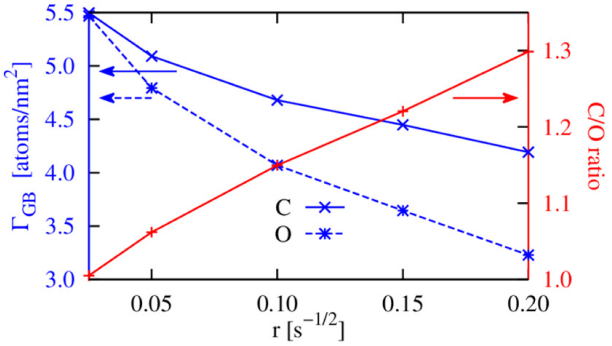

Figure 2.11: Amount of atoms per area on the grain boundaries Γ_{GB} as a function of the characteristic cooling rate r [37]. It is observed that at higher cooling rates the ratio of C to O increases.

TZM contains ZrO_2 particles also, this effect may occur as well.

2.1.2.5 Deformation behavior

As mentioned before, Mo possesses a high stacking fault energy, which means that recovery usually predominates recrystallization. Further, low cycle fatigue tests by Samoilov et al. [42] suggested a work softening behavior of Mo at high temperatures. Chaudhuri et al. [43] did hot compression tests in Mo with different strain rates ($0.01–10\,s^{-1}$) up to a true strain of 0.6 and in a temperature range from 1,400°C to 1,700°C. Figure 2.12 shows the resulting stress–strain flow curves. First, it is observed that work hardening occurred at high strain rates regardless of temperature. Steady-state or work softening was observed at lower strain rates. Additional investigations showed that at high strain rates the microstructure consisted of deformed grains with high misorientation, while EBSD investigations indicated that the main mechanism was dynamic recovery at low strain rates. Recrystallization only occurred sparsely and at specific temperature / strain rate combinations of $0.1\,s^{-1}$ / 1,600°C and $1\,s^{-1}$ / 1,700°C. A schematic map of their findings is drawn in figure 2.13 [43].

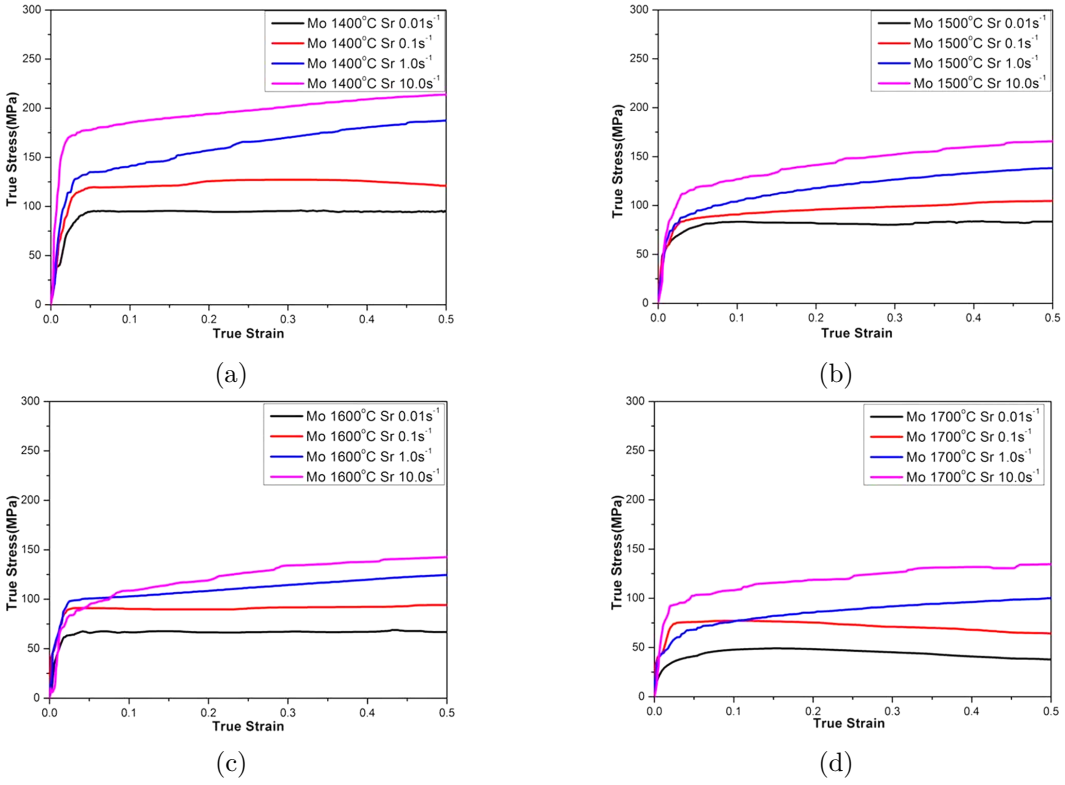

Figure 2.12: Flow curves of Mo in the range of 1,400–1,700°C and 0.01–10 s^{-1} strain rate [43].

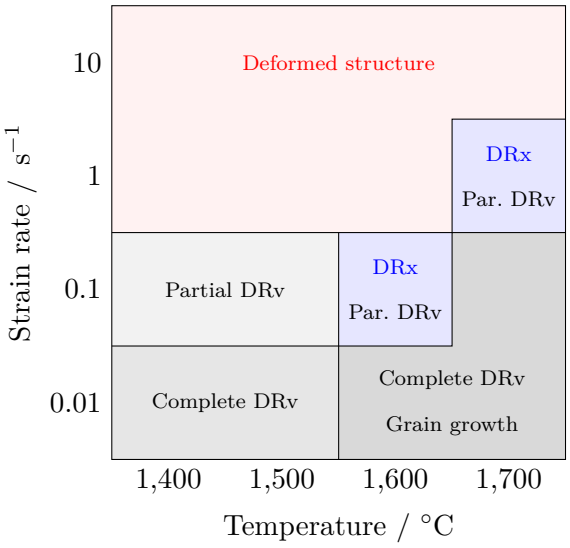

Figure 2.13: Schematic compilation of the restoring mechanisms during the hot deformation at different temperatures and strain rates of molybdenum. Operating mechanisms are dynamic recrystallization (DRx), partial and full dynamic recovery (DRv), and grain growth [43].

2.1.3 Molybdenum alloys

To further increase the high melting point, high modulus of elasticity, and low coefficient of thermal expansion, among others, molybdenum is alloyed with a number of elements. In general, three main alloy types are used among molybdenum [17]:

1. Solid solution strengthening alloys (e.g. Mo–Re)
2. Composite metal alloys (e.g. Mo–Cu)
3. Precipitation strengthening alloys (e.g. TZM)

2.1.3.1 Main alloying elements

Boron and silicon increase the hardness both at room and at elevated temperatures. Titanium (Ti), zirconium (Zr), niobium (Nb), tantalum (Ta), and vanadium (V) decrease the hardness by de-oxidation, but increase the recrystallization temperature by a few hundred degrees, as figure 2.14 illustrates. With an appropriate distribution of these additions, it is possible to achieve a recrystallization temperature for molybdenum up to 1,500°C [1].

Lanthanum (La) or yttrium (Y) can be added in the form of the oxides La_2O_3 or Y_2O_3 to form oxide dispersion strengthened alloys which exhibit reduced oxidation rates [12, 18].

Carbon contents up to 0.06 wt.% result in an increased ductile–brittle transition temperature, while the ductile state during hot forming is sustained. As observed in the Mo–C phase diagram in figure 2.15, with a carbon content up to about 0.2 wt.% the basic molybdenum α phase is preserved, in excess of that, Mo_2C is formed [1]. Titanium (Ti) or hafnium (Hf) additions can also form carbides which result in carbide strengthened molybdenum alloys.

2.1.3.2 Solid solution strengthening alloys

Solid solution strengthening alloys are the basic type of substitutionary alloys, where the alloying elements replace some of molybdenum's lattice positions. Most commonly rhenium, tungsten, tantalum, or niobium are used to enhance the properties of molybdenum [3]. Figure 2.16 shows phase diagrams for Mo–Re [44, 45] and Mo–V [46]. It is observed that Mo–Re forms a quasi-solid solution crystal up to 39 wt.% Re, while Mo–V is fully solid solution over the entire concentration domain. Alloys of rhenium and molybdenum ranging from 15–41% Re yield ductile fusion welds, which possess similar mechanical properties like the base metal [9, 10, 47]. These alloying

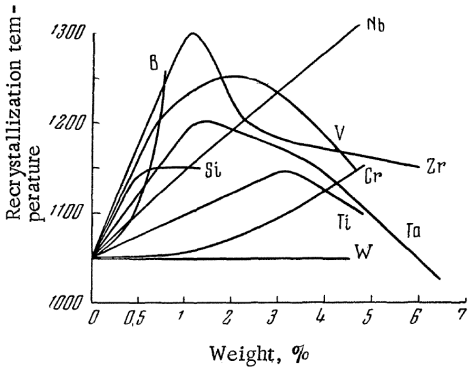

Figure 2.14: Recrystallization temperature of molybdenum with different alloying additions [1]

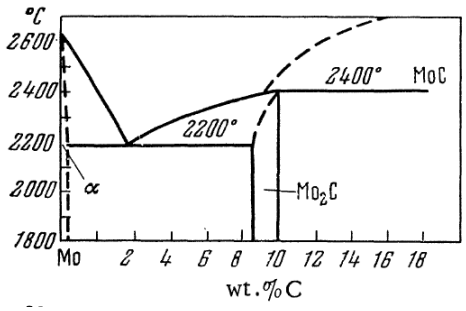

Figure 2.15: Molybdenum–carbon phase diagram [1]

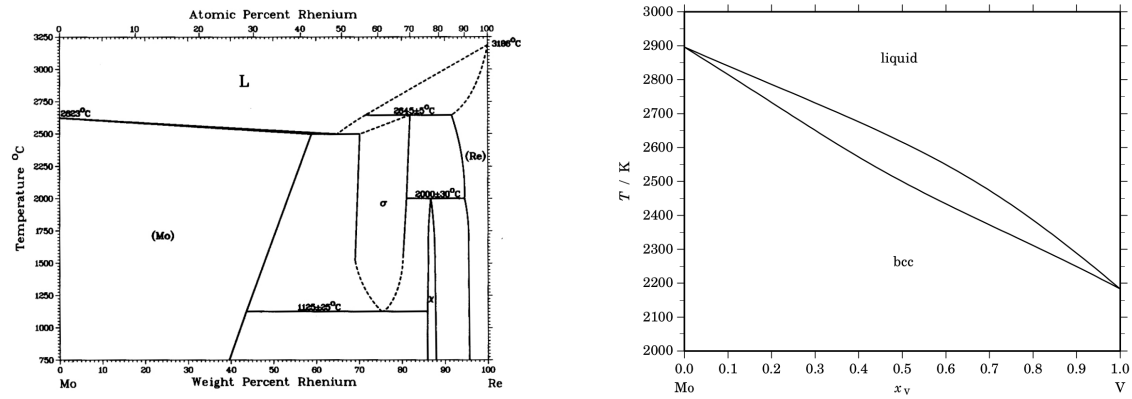

(a) (b)

Figure 2.16: (a) Phase diagram for molybdenum–rhenium [44] and (b) a calculated phase diagram for molybdenum–vanadium [46]

elements, however, increase the already high price of molybdenum further, which makes the application of Mo–Re and other refractory metal alloys a question of investment.

2.1.3.3 Composite metal alloys

Composite metal alloys can be produced by blending powder prior to sintering. Material combination with molybdenum may be built with copper, titanium, or sodium. Furthermore, Mo–Cu composites are produced by infiltrating a pre-sintered molybdenum skeleton with liquid copper. This technique results in an outstanding combination of the properties of both components, since the molybdenum base frame possesses an adequate lattice. Moreover, the porosity of the finished composite is kept to a minimum, given that the Mo skeleton has a sufficiently open porosity for admitting the copper melt [3].

2.1.3.4 Carbide strengthening alloys and molybdenum alloy TZM

Low Ti and Zr additions result in small carbide and oxide precipitates, which increase the strength of material and the creep resistance at high temperatures. The carbide precipitates act as inhibitors for recrystallization by obstructing grain growth and elevate the recrystallization temperature from pure molybdenum's 1,100°C to 1,400°C [3, 10, 12, 48]. To sustain the technological ductility, the maximum quantity of alloying elements in precipitation strengthened molybdenum is limited to tenths of a percent [1].

Molybdenum–hafnium–carbon (MHC) is an important Mo base alloy with 1.2 wt.% Hf and 0.1 wt.% C. The dispersion of hafnium carbides strengthens the Mo base metal considerably, as observed in figure 2.17. Further, the recrystallization temperature is increased to 1,550°C [12].

Titanium–zirconium–molybdenum alloys are called TZM alloys and also belong to the dispersion strengthened Mo-alloys. Their typical composition is listed in table 2.5. Compared to pure Mo, the mechanical properties are increased, as listed in table 2.6 [1, 12]. The creep rate of TZM is illustrated in figure 2.18, demonstrating the significant difference of TZM to pure Mo.

Table 2.5: Typical composition of TZM alloy [12, 48]

Element	content
Molybdenum, Mo	balance
Titanium, Ti	0.5 wt.%
Zirconium, Zr	0.08 wt.%
Carbon, C	0.01–0.04 wt.%

Young's moduli of most molybdenum alloys including TZM are comparable to pure molybdenum's. The ultimate tensile strength (UTS) of TZM is higher than pure Mo but lower than

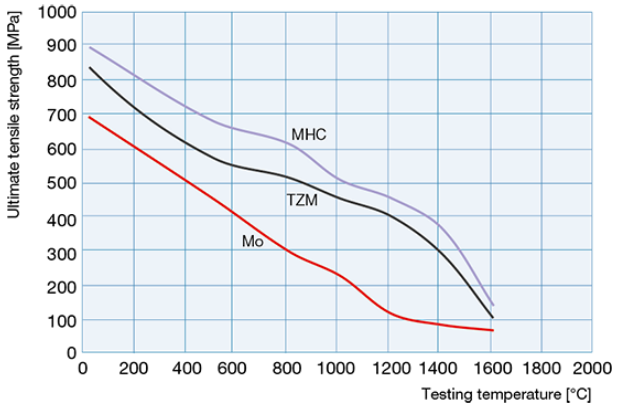

Figure 2.17: Typical UTS values for Mo, TZM, and MHC (molybdenum–hafnium–carbon) bar material in stress relieved condition [12]

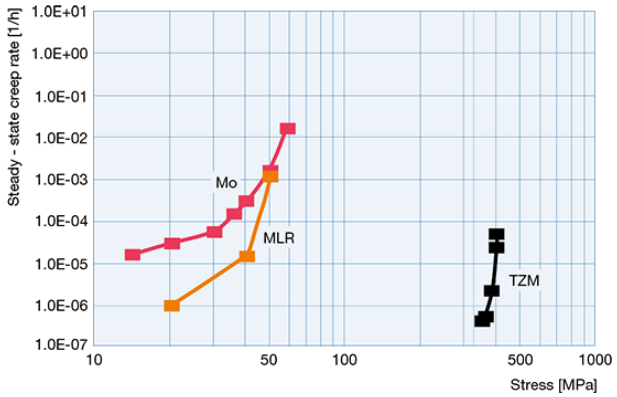

Figure 2.18: Steady-state creep rates of Mo, TZM, and MLR (molybdenum–lanthanum recrystallized) sheet metal at 1,100°C [1, 12]

Table 2.6: Mechanical properties of TZM [1]

	20°C	1,200°C
Yield strength [MPa]	734	173
Ultimate tensile strength [MPa]	897	345
Elongation [%]	8	10

MHC and decreases similarly with temperature, as depicted in figure 2.17. In the temperature range from 600°C to 1,600°C, TZM possesses a significantly higher UTS than pure Mo.

The ultimate tensile strength of a work-hardened TZM alloy is 150% higher, and the creep strength of the latter is 300% higher than in untreated, pure molybdenum [1]. The grain growth resistance effect of the Ti and Zr carbide particles improves the weldability as the resulting grain size is limited [10].

2.1.4 Processing

2.1.4.1 Production route

The main ores for molybdenum are molybdenite MoS_2 and wulfenite $PbMoO_2$, which occur mostly in North America and Norway, but also in Chile and Germany [4, 12]. Molybdenite are oxidize roasted at 400–650°C in air (equation 2.1) leading to molybdenum trioxide (MoO_3). Pure Mo powder is obtained by the reduction of MoO_3 with hydrogen, either in one (equation 2.2) or in multiple steps via MoO_2 and MoO [4].

$$MoS_2 + 3\frac{1}{2}\,O_2 \rightarrow 2\,SO_2 + MoO_3 \tag{2.1}$$

$$MoO_3 + 3\,H_2 \xrightarrow{1000°C} Mo + 3\,H_2O + 112\,kJ \tag{2.2}$$

2.1.4.2 Production of technical Mo-alloys

The Mo powder is mixed with alloying components where applicable and then further processed by vacuum arc melting, electron beam melting, or powder metallurgy. Today, 97% of all molybdenum based materials is processed by powder metallurgy [18]. Figure 2.19 shows a schematic flow of Mo processing by powder metallurgy. Here, after mixing and pressing, the sintering process leads to Mo metal blanks, which are then hot or cold rolled to reduce the porosity. The final step of stress relief annealing concludes the production process of technical Mo and Mo-alloys [12].

2.1.4.3 Machining

Molybdenum and TZM are machinable by turning, milling, and drilling by means of high speed steel (HSS) and hard metal (HM) tools, preferably with a cutting edge geometry similar to machining aluminum. In any case, a much higher wear of the tools is expected, as molybdenum is considerably more abrasive than steel at similar hardness values [9, 12].

2.1.4.4 Joining

Molybdenum and its alloys can be joined mechanically by riveting or bolting.

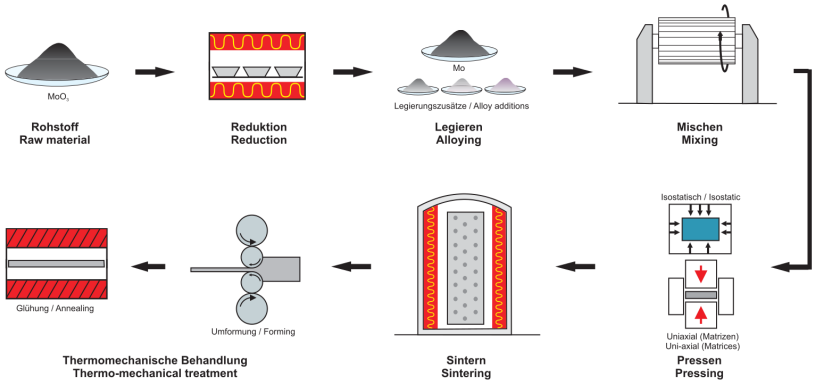

Figure 2.19: Schematic flow of the production of powder metallurgically produced semi-finished products [12]

Material joints by brazing with AgCu based brazing alloys up to 1,000°C, alloys of Ni and precious metals at 1,400°C, and Ti, Zr, Ru, Pd, Co, and Pt based alloys up to 2,000°C are in commercial use [9, 12, 49].

Due to its high melting point and the required total energy input, welding is only possible by techniques with high specific powers, or by solid state welding, which operates below liquidus [17, 50]. Solid state welding has also the advantage of a short process time, which results in fine grains due to recrystallization. Friction welding of molybdenum is applied industrially and has also been the content of some scientific research [7, 51, 52].

Investigations of welding TZM with different welding techniques showed that pores and cracks were produced, if the heat input dropped below a certain level. Oxygen and nitrogen were accounted for causing cavities [17]. Even small amounts of O and N, caused by an improper welding atmosphere, lead to embrittlement in the joint [9]. Moreover, the welding zone shows a substantial grain growth [17].

Experimental results of a four-pass tungsten inert gas (TIG) weld of Mo with a Mo–Re filler material showed improved mechanical properties compared to pure Mo welds. The base material was alloyed with traces of zirconium, carbon, and boron. Hereby, the fracture elongation was increased from 3% to 20% compared to regular molybdenum welds. Zirconium, boron, and carbon acted as getter elements for the present oxygen and nitrogen and inhibited a segregation on the grain boundaries. On this account, the ductility vastly increased and the fracture mode changed from intergranular failure to transgranular failure [13].

The high affinity to oxygen resulted in cracks in a TIG weld under argon atmosphere with 0.05% oxygen contamination and to crater cracking at 0.02% oxygen [20].

Electron beam welding of molybdenum and its alloys has been investigated to a considerable extent [10, 17, 47]. It was reported that molybdenum alloys are preferable to pure molybdenum because of its less tendency to form coarse grains. Mo–Re showed the best weldability with sustained ductility of the welds.

2.1.5 Modeling of material behavior

As discussed previously, the deformation behavior of metals and alloys is a function strongly dependent on temperature, strain, strain rate, and therefore the underlying metallurgical mechanisms [53]. Mathematical models may be used to depict the the flow stress behavior of different metals. Strictly empirical or semi-empirical models using a power law approach and simpli-

fied assumptions of thermally activated flow are widely in use [54, 55]. Other authors pursued a more phenomenological approach of describing the flow kinetics, as for example Mecking and Kocks [56], or adapted existing models to enhance the fit to observed flow stress behaviors [57–59].

2.1.5.1 Johnson–Cook flow stress model

One of the first approaches to model flow stress numerically was delivered by Gordon R. Johnson and William H. Cook in 1983 [54]. The model includes effects of strain hardening, strain rate hardening, and thermal softening. Although strictly empirical, the model covers a wide range of materials to an often satisfactory extent. The *von Mises* flow stress is written as

$$\sigma = (A + B\varepsilon^n)(1 + C \ln \dot{\varepsilon}^*)(1 - T^{*m}), \tag{2.3}$$

where the homologous temperature in the form of

$$T^* = \frac{T - T_r}{T_m - T_r} \tag{2.4}$$

is comprising the melting temperature T_m and room temperature T_r. The strain rate is normalized to $\dot{\varepsilon}_0 = 1\,\mathrm{s}^{-1}$ by $\dot{\varepsilon}^* = \dot{\varepsilon}/\dot{\varepsilon}_0$. The material constants A, B, n, C, and m can be obtained experimentally.

2.1.5.2 Zerilli–Armstrong flow stress model

Frank J. Zerilli and Ronald W. Armstrong formulated a semi-empirical model for flow curves and therein two separate equations for fcc and bcc metals [55]. First it is stated that the thermal activation can be assumed independent of strain for bcc crystals. The thermal part of the equation can therefore be written disregarding the plastic strain ε as

$$\sigma_{th} = c_1 \cdot e^{-c_3 T + c_4 T \ln \dot{\varepsilon}}. \tag{2.5}$$

Analogously to the Johnson–Cook equation, $\dot{\varepsilon}$ is again normalized to $\dot{\varepsilon}_0 = 1\,\mathrm{s}^{-1}$. Combined with the athermal part, which is represented by an assumed power law in the form of

$$\sigma_{ath} = c_5 \cdot \varepsilon^n + c_6, \tag{2.6}$$

the full model for flow stress of bcc crystals is

$$\sigma = c_1 \cdot e^{-c_3 T + c_4 T \ln \dot{\varepsilon}} + c_5 \cdot \varepsilon^n + c_6. \tag{2.7}$$

Note that c_2 occurs only in the equation for fcc crystals, and is missing in the present equation for reasons of continuity with literature.

While the J–C model is strictly empirical but often sufficient to fit a certain material behavior, the Z–A model possesses an underlying physical interpretation of thermal activation of dislocations [60, 61]. Most authors argue that compared to the J–C model, the Z–A model is able to represent the strong flow stress dependency of bcc metals on temperature and strain rate better and is therefore preferable [62, 63]. However, Liang et al. pointed out that since most metals exhibit a work-hardening behavior that is dependent on temperature and strain rate, which the Z–A model ignores, it is not ideal [64].

Zerilli and Armstrong themselves stated that the model was developed for modeling Taylor cylinder impact tests with strain rates of 10^4–$10^6\,\mathrm{s}^{-1}$ and temperatures up to one half of the melting temperature in absolute (for Mo that is 1,174°C) [55].

Table 2.7: Z–A constants for Mo [65, 66]

	c_1 / MPa	c_3 / MPa	c_4 / K^{-1}	c_5 / K^{-1}	c_6 / MPa	n
Scapin 1	4,030	$6.449 \cdot 10^{-3}$	$3.073 \cdot 10^{-4}$	524	0	0.110
Scapin 2	2,833	$5.203 \cdot 10^{-3}$	$2.639 \cdot 10^{-4}$	485	0	0.135
Chen	1,030.115	$7.45 \cdot 10^{-4}$	$2.9389 \cdot 10^{-5}$	−48.3076	−16.515	−0.49119

Scapin et al. [65] and Chen et al. [66] published sets of coefficients for different, commercially available Mo products for the Zerilli–Armstrong (Z–A) model, which are as follows in table 2.7.

It is apparent that the values of Scapin and Chen differ largely from one another. First, Scapin presupposed that c_6 equals zero, thus reducing the degree of freedom for the variable optimization. Second, if n is a negative value as in the case of Chen, the characteristics of the function switches from parabolic to hyperbolic, although it remains monotonously increasing as long as c_5 is negative as well. It appears that the high degree of freedom for the optimization of six variables allows largely different outcomes, which may also depend on the starting values of the iterative optimization procedure.

If the exponential term of the thermal part of the Z–A model

$$e^{-c_3 T + c_4 T \ln \dot{\varepsilon}} = e^{(-c_3 + c_4 \ln \dot{\varepsilon}) \cdot T} = e^{c(\dot{\varepsilon}) T} \tag{2.8}$$

is examined, it becomes apparent that with rising temperature the change of the flow curve decreases, as long as

$$-c_3 + c_4 \ln \dot{\varepsilon} < 0, \tag{2.9}$$

which is the case because usually $c_3 \gg c_4$. The limit of the exponential function then is

$$\lim_{T \to \infty} e^{c(\dot{\varepsilon}) T} = 0 \tag{2.10}$$

and hence the limit for the full Z–A model is the athermal part σ_{ath} which is independent from the strain rate with

$$\lim_{T \to \infty} \sigma_{ZA} = c_5 \cdot \varepsilon^n + c_6. \tag{2.11}$$

This results in congruent flow curves at sufficiently high temperatures. Figure 2.20 shows the progression of the thermal part of the Z–A model (equation 2.5), calculated with the coefficients of table 2.7. It is observed that with both sets of coefficients of Scapin et al., the thermal stress drops to neglectable values at approximately 1,000°C (1,273 K), while with Chen's coefficients, the drop is slower and sufficiently high thermal stress values until (hypothetical) 6,000 K are sustained. Scapin's coefficients therefore work sufficiently up to 1,000–1,100°C, as reported [65], whereas at higher temperatures both the temperature dependency as well as the strain rate sensitivity of the model is lost. At the relatively low strain rates and high temperatures present in friction welding the model with the coefficients of Scapin is expected to deviate substantially from experimental data.

For TZM it is, reported that the influence of the strain rate on the flow stress is greater at low temperatures [67].

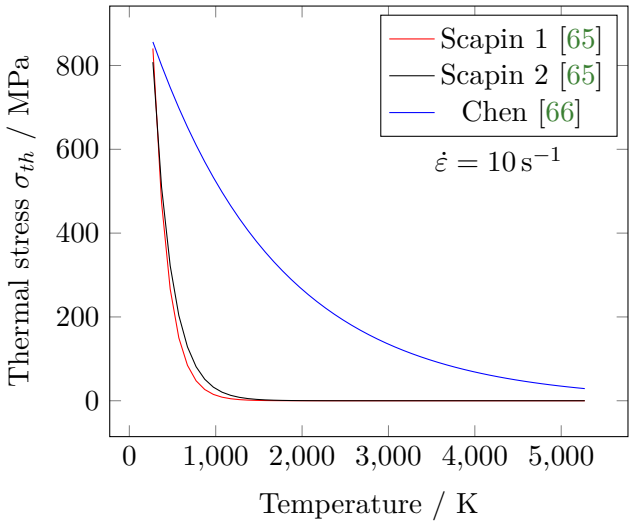

Figure 2.20: Course of the thermal part of the Z–A model with different coefficients at $\dot{\varepsilon} = 10\,\mathrm{s}^{-1}$

2.2 Experimental

To characterize molybdenum's flow stress behavior, isothermal compression experiments were planned and executed in a wide temperature range and at different strain rates.

2.2.1 Flow curve acquisition

For modeling of rotary friction welding processes, or any deformation process for that matter, temperature- and strain rate dependent material data is necessary. Literature states multiple results for refractory metals and molybdenum with according flow stress models [65, 66, 68], but mostly for high strain rates ($\dot{\varepsilon} > 10^4\,\mathrm{s}^{-1}$) and low temperatures ($T < 0.5 \cdot T_m$). In welding processes, temperatures up to the melting point have to be modeled, and also the welding behavior determining processes are expected to be in the high temperature / high deformation area. Therefore, comprehensive knowledge and data of molybdenum's deformation behavior is required. For this reason, a series of compression experiments was planned and executed on a *Gleeble 3800* simulator at the institute to acquire flow curves of commercially pure molybdenum.

The Gleeble machine can work with true strain and calculate the required stroke accordingly. As drawn in figure 2.21, if the deformation reference is the start length l_0, we consider the

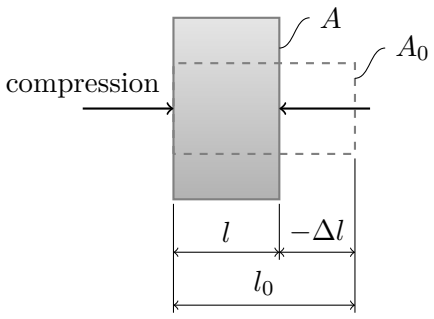

Figure 2.21: Uniform deformation of a Gleeble sample

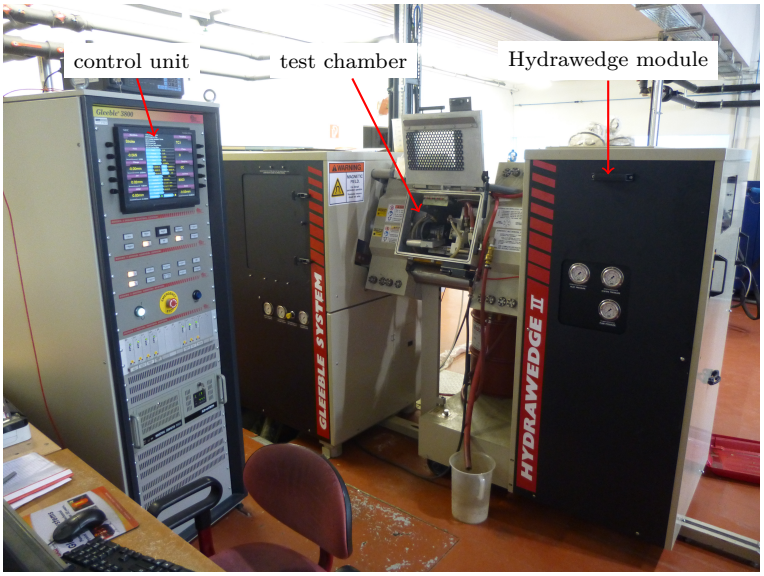

Figure 2.22: The *Gleeble 3800* with the installed *Hydrawedge II* module at the IMAT

engineering strain as

$$\varepsilon_E = \frac{\Delta l}{l_0}. \tag{2.12}$$

The true strain then is per definition

$$\varepsilon = \ln(\varepsilon_E + 1), \tag{2.13}$$

and thus

$$\varepsilon = \ln\left(\frac{\Delta l + l_0}{l_0}\right). \tag{2.14}$$

The true stress is calculated assuming a uniform, cylindric deformation (also figure 2.21). The preservation of volume

$$A \cdot l = const. \tag{2.15}$$

and the definition of stress

$$\sigma = \frac{F}{A} \tag{2.16}$$

lead to

$$\sigma = \frac{F \cdot (\Delta l + l_0)}{A_0 \cdot l_0}. \tag{2.17}$$

Note that because a compressive deformation is considered, Δl is negative.

Figure 2.22 shows the Gleeble machine setup at the institute, in figure 2.23 the schematic setup of a compression test is sketched. Another feature is the closed control loop of the Gleeble machine which controls the temperature of the sample during the experiment. This way, the occurring adiabatic heating of the samples which results from deformation, can be absorbed to some extent.

Figure 2.24 depicts the schematic procedure of the experiments. The specimen is heated to the experiment temperature with a heating rate of 10 $^{\mathrm{K}}/_{\mathrm{s}}$ and then the temperature is held for 120 s to facilitate a uniform temperature field in the sample. Subsequently, the deformation

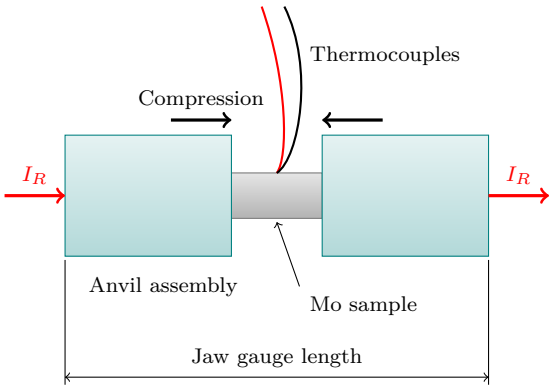

Figure 2.23: Schematic setup of a Gleeble test

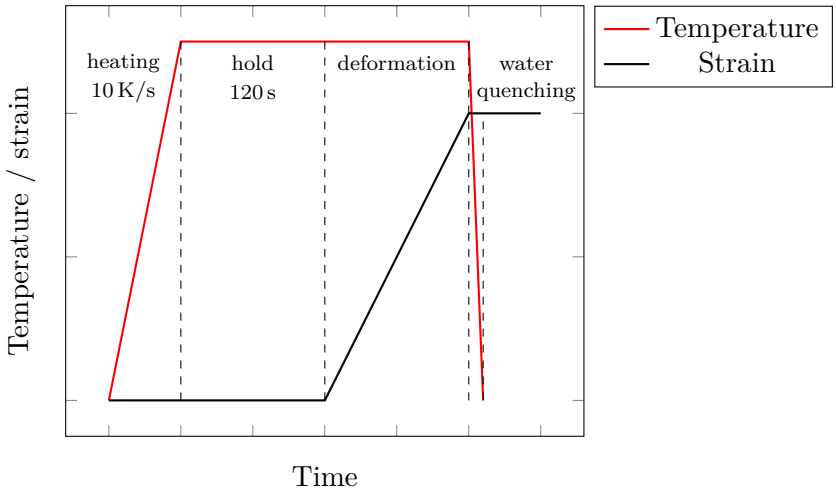

Figure 2.24: Schematic courses of temperature and strain of a Gleeble test

experiment starts and continues to a total true strain of 1 with a constant true strain rate. Finally, the specimen is water quenched and the experiment is finished.

Commercially pure Mo rod samples were used. The sample production route was sintered, cogged, and machined to the final dimensions of ∅6 × 12 mm. The compression tests were executed at four different strain rates: 0.01, 0.1, 1, and $10\,s^{-1}$. Test temperatures were set in 11 levels at 200, 400, 600, 750, 900, 1,100, 1,200, 1,300, 1,450, 1,600, and 1,700°C. The current Gleeble configuration at the institute does not allow experiments to exceed 1,750°C. K-type thermocouples under vacuum were used for all experiments up to 1,100°C, while S-type thermocouples and argon shielding gas were used for the experiments of 1,200°C and above.

2.3 Results

2.3.1 Flow curve acquisition

Collecting all experiments, flow curves at constant strain rates 0.01, 0.1, 1, and $10\,s^{-1}$ are plotted in figure 2.25. Comparing the four subfigures, a number of things are observed.

A distinct peak in flow stress is observed at all experiments at 900°C and below while the experiments from 1,100°C onwards do not show this effect. These peaks are also observed by Nemat-Nasser et al. [53]. They are accounted on the change in microstructure due to static

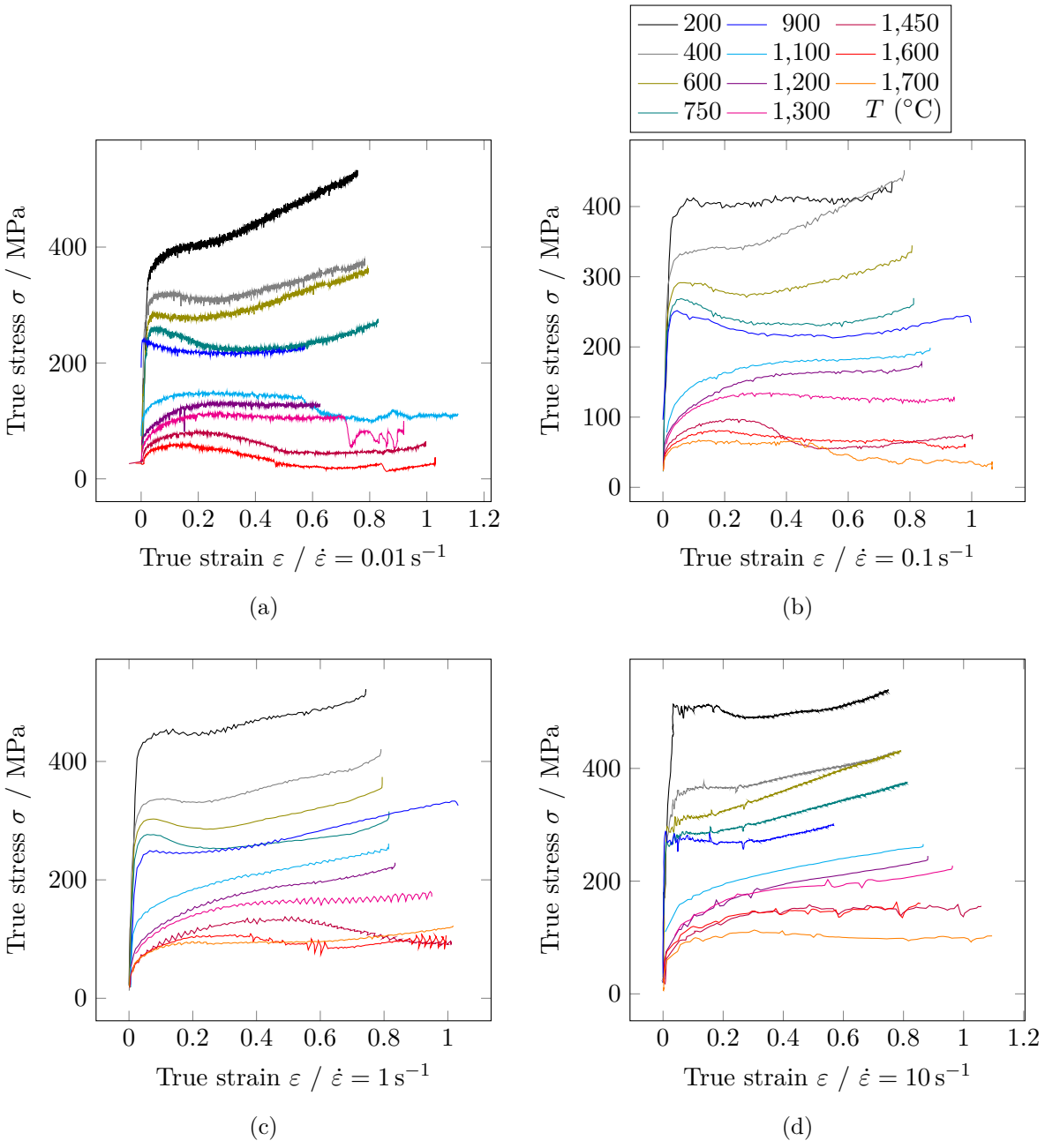

Figure 2.25: Stress-strain curves true strain Gleeble experiments at various temperatures and constant strain rates of (a) $\dot{\varepsilon} = 0.01\,\mathrm{s}^{-1}$, (b) $\dot{\varepsilon} = 0.1\,\mathrm{s}^{-1}$, (c) $\dot{\varepsilon} = 1\,\mathrm{s}^{-1}$, and (d) $\dot{\varepsilon} = 10\,\mathrm{s}^{-1}$

recrystallization during the thermal soaking before the deformation of all experiments of 1,100°C and above. Figure 2.26 shows the resulting flow stress of two experiments, one with a holding temperature of 900°C and one was heated to 1,200°C, subsequently cooled back to 900°C, and finally deformed. In the as-received specimen the peak in flow stress has disappeared and the flow stress is also lower. This is explained by the microstructure in figure 2.27, where two deformation specimens were heated to (a) 900 and (b) 1,200°C, held for 120 s, and cooled back to room temperature without any deformation. It is observed that after 120 s at 1,200°C the

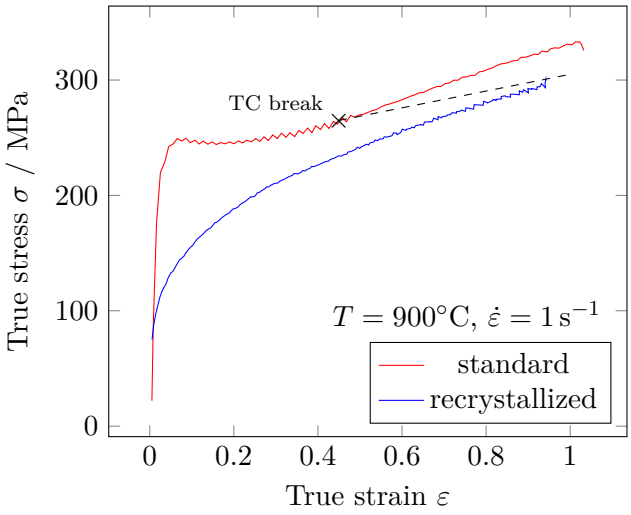

Figure 2.26: Standard and recrystallized experiments

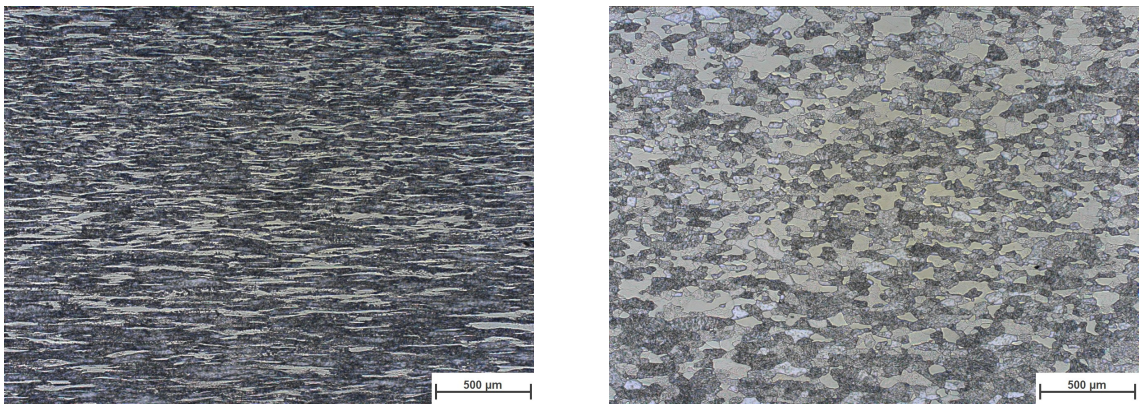

(a) (b)

Figure 2.27: Microsection of Gleeble samples after (a) 120 s at 900°C and (b) 120 s at 1,200°C thermal cycle

cross section shows a highly recrystallized microstructure, while at 900°C almost no change from as-received base material is visible. In the case of the 900°C-sample, during deformation dynamic recovery occurs that opposes the deformation, which in the regime from strain 0–0.2 is responsible for the peak, subsequent drop, and strain hardening thereafter. If the microstructure is already fully recrystallized the process obviously starts from a different basis and the resulting flow stress deviates from the previous one.

At higher temperatures and low strain rates (0.1 and 0.01 s^{-1}) a trend towards strain softening is observed, as for instance observed at 1,300 and 1,600°C in figure 2.25a and b. This is in accordance to literature [43] and the work softening behavior is accounted on dynamic recovery. In the temperature range of 200 to 1,300°C, strain hardening is observed at higher strain rates.

A high sensitivity to strain rate is observed especially at high temperatures. Exemplary the flow stress at 1,600°C is 55 MPa at 0.01 s^{-1} and 150 MPa at 10 s^{-1}, which is almost triple.

2.3.2 Flow curve modeling

The Zerilli–Armstrong model is suitable for materials with a distinct strain hardening characteristic like molybdenum at low and medium temperatures. The results from the Gleeble experiments can be analyzed and fitted to obtain the coefficients for the flow stress model. The command prompt tool *gnuplot* can be used to fit an arbitrary function to a dataset using a nonlinear least-squares Marquardt–Levenberg algorithm [69, 70]. The dataset of all Gleeble experiments of Mo were compiled and fed into the *gnuplot* algorithm to obtain a set of coefficients for all recorded flow curves and thus obtaining a least-square optimized set of Z–A coefficients. The coefficients published by Scapin et al. [65] were used as starting point for the calculation.

Table 2.8 lists the result of the fit. It is observed that the values differ largely from the values obtained by Scapin et al. [65] and notably from Chen et al. [66].

Table 2.8: Fitted *Z–A* constants for the obtained Gleeble flow curves

	c_1 / MPa	c_3 / MPa	c_4 / K^{-1}	c_5 / K^{-1}	c_6 / MPa	n
Value	773.79	$1.11 \cdot 10^{-3}$	$4.86 \cdot 10^{-5}$	46.35	0	0.5853

Figure 2.28 shows an assessment of the resulting flow curves in comparison to the according Gleeble experiments. It is observed that the flow stress is slightly overpredicted at 400°C and as well at 1,600°C (figure 2.28a and c), while it is lower than the experimental data at 900°C. While the modeled flow curve at 1,600°C and strain rate $10\,s^{-1}$ is in good agreement, the experimental data shows that the flow stress is lower at lower strain rates. Figure 2.29 shows the resulting local maxima of flow stress of the Gleeble experiments in the interval of $\varepsilon = [0, 0.25]$, the flow stress of the Z–A models by Scapin et al., Chen et al. [66] (table 2.7), and the fitted Z–A model with the coefficients of table 2.8. The flow stress of the three sets of Z–A coefficients represent the stress at a strain of 0.25.

First, it is observed that the coefficients of Scapin lead to an asymptotic development of the flow stress, regardless of strain rate. For the fitted coefficients the limit is 20.59 MPa. Apart from the absolute value, the difference between the two sets of coefficients is that the asymptote is reached at a much lower temperature in Scapin 2 than in the fitted coefficient set. The resulting flow stresses of Chen et al. differ strongly from those of Scapin and show no asymptotic limit in the observed temperature interval. The investigated material, however, appeared to differ from the material used in this work.

Second, it is observed that the stresses drop significantly between 900 and 1,100°C, which is a result of the aforementioned different material condition prior to deformation. At 900°C the state of the material remains unchanged, while after a holding time of 2 min at 1,100°C the material is fully (statically) recrystallized. This metallurgic difference results in the "kinks" observed in the experimental lines in figure 2.29.

Third, the strain rate sensitivity declines with increasing temperature in the fitted Z–A model, while in the experiments suggest a tendency to increased strain rate sensitivity.

In general, strain hardening is observed at temperatures below 1,100°C, which extends to higher temperatures the higher the strain rate. At $\dot{\varepsilon} = 10\,s^{-1}$ strain hardening is still observed at 1,300°C. Steady-state behavior of the flow stress is observed at temperatures from 1,100°C ($\dot{\varepsilon} = 0.01\,s^{-1}$) to 1,600°C ($\dot{\varepsilon} = 10\,s^{-1}$). Finally, a first transition to strain softening is observed at 1,300°C at $\dot{\varepsilon} = 0.1\,s^{-1}$. The steady-state and softening behavior is accounted to intensive recovery processes, which is more restricted if the deformation is faster, which explains the transition at different temperatures at different strain rates.

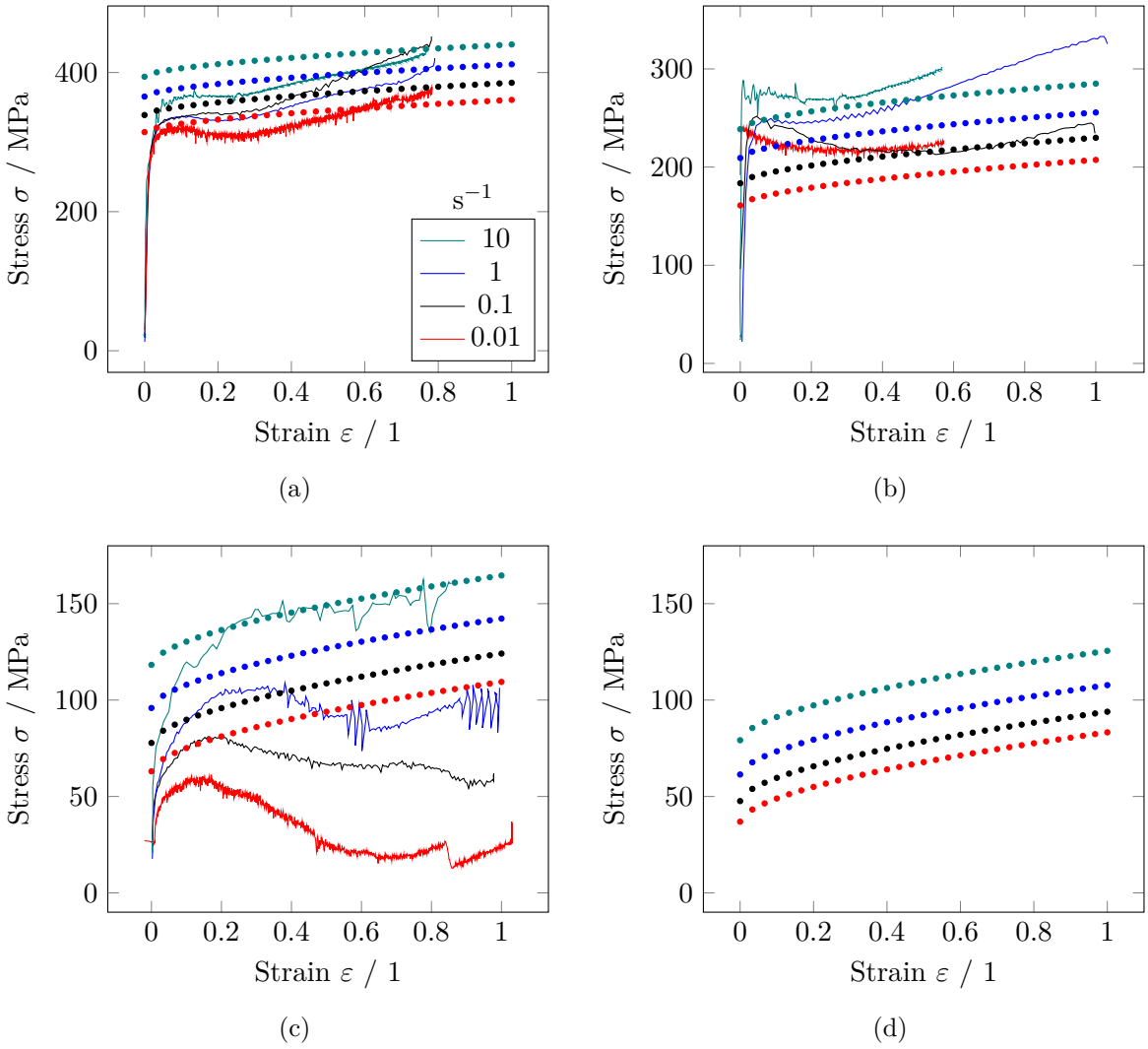

Figure 2.28: Comparison between experimental data and modeled Z–A flow curves at various strain rates and (a) 400°C, (b) 900°C, (c) 1,600°C, and (d) extrapolated to 2,000°C

To sum up, the Zerilli–Armstrong flow stress model allows a rough representation of the flow stress behavior of molybdenum from room temperature to melting temperature, although multiple effects—including the latter list—remain unconsidered.

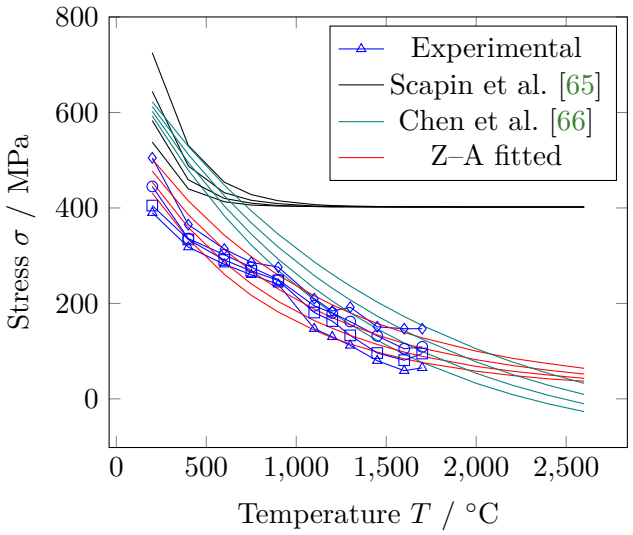

Figure 2.29: Comparison of the flow stress of the Gleeble experiments to the Z–A model of Scapin et al. [65], Chen et al. [66], and the fitted Z–A model

3 Friction Welding

To understand the mechanisms of friction welding, this chapter gives an overview of the technology and the process parameters. Effects on the resulting welds are discussed in general and more specifically on molybdenum and its alloys. Experiments were conducted in tube format and on a laboratory scale in rod format in molybdenum and TZM. Especially the observed atypical friction welding behavior of molybdenum is discussed thoroughly and first steps in the numerical simulation of the process are presented.

3.1 State of the art

Welding with application of force and temperature, with or without filler material, is summarized as solid state welding. Heating facilitates an adhesive bond of the parts, although the liquidus temperature of the material is never exceeded (figure 3.1) [71–73].

Friction welding is a combination of an applied force and the resulting heat generated by the friction between two parts in relative motion to each other. Advantages of the process compared to common fusion welding processes are:

1. No melting and therefore no solidification effects
2. Less heat input than fusion welding and therefore a smaller heat affected zone
3. Fast process—short cycle time
4. No special weld seam preparation necessary
5. Dissimilar joints are possible, even such as metals to ceramics [74]
6. Filler material and shielding gas are optional

On the other hand, some drawbacks of friction welding can be enumerated also:

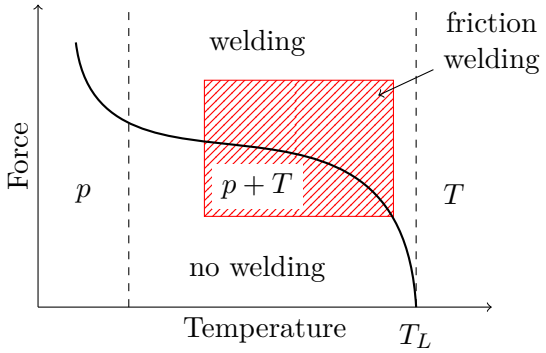

Figure 3.1: Qualitative area of friction welding: p ... pressure only; $p+T$ ... pressure and heat; T ... heat only; T_L ... liquidus temperature

1. Formation of a flash—post weld machining may be required

2. Welding machine is stationary

3. High clamping and process forces

Conventional friction welding can be classified into three main techniques: Rotary friction welding (RFW), orbital friction welding (OFW), and linear friction welding (LFW). All three process principles are depicted in figure 3.2. At RFW, a rotating part is pressed against a stationary part. This process requires at least one of the two parts to be axially symmetrical or at least quasi symmetrical (e.g. hexagonal). In contrast, two parts are pressed together and oscillated linearly at LFW or orbitally at OFW. With this technique, unsymmetrical parts can be joined, but because of the oscillating movement, the process is more complicated to implement than RFW. Another disadvantage of RFW compared to LFW is that the relative velocity varies over the area (see figure 3.2) which leads to a non-uniform heat generation and consequently to a varying thickness of the HAZ [75].

With friction stir welding (FSW), a new variant of friction welding was developed in the early 1990's by TWI. In this process the base material is stirred with a rotating non-consumable tool. It is used to join aluminum, copper, titanium, and steel similarly and dissimilarly [76, 77].

3.1.1 Rotary friction welding

In rotary friction welding, two technical approaches exist: direct or continuous drive friction welding (DDFW) and inertia drive friction welding (IFW). In North America, IFW has established, where a flywheel is accelerated priorly to the welding process which releases its energy for welding. In Europe, DDFW is more common. In this technique, an electric motor directly drives the spindle and continuously delivers the required welding energy.

3.1.1.1 Inertia friction welding

The welding parameters in inertia friction welding are the available welding energy $E(t)$, which is stored in the flywheel, and the friction pressure $p(t)$. The total process time t_t and welding energy directly depend on the pressure and the initial speed n_0. Figure 3.3 represents a typical inertia weld cycle for TZM. Here, the process is divided into two stages with two pressure levels: 39 MPa and 96 MPa. In IFW, the heat generated in the friction surface is solely withdrawn from

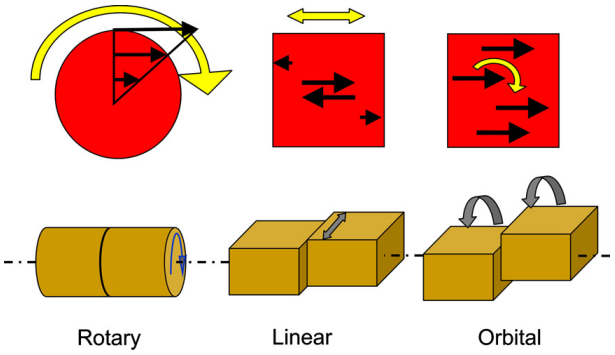

Figure 3.2: Three variants of friction welding: The black arrows in the upper pictures indicate the relative velocities causing the heat generation [75].

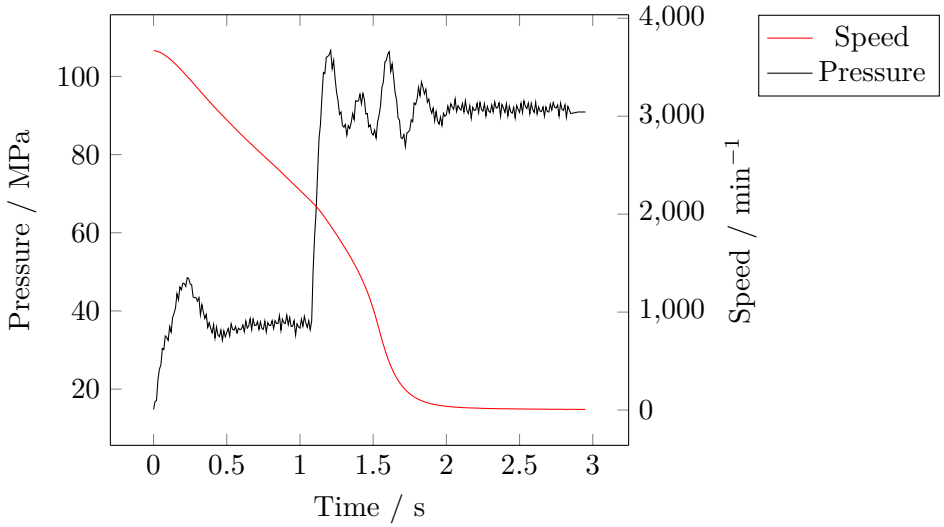

Figure 3.3: Welding speed and axial pressure of an inertia welding process of a TZM tube

the flywheel with the moment of inertia J and its speed $\dot{\varphi}$, hence the consideration

$$E(t) = \frac{1}{2} J \dot{\varphi}(t)^2 \tag{3.1}$$

$$P(t) = \frac{\mathrm{d}E(t)}{\mathrm{d}t} = J \dot{\varphi}(t) \ddot{\varphi}(t) \tag{3.2}$$

leads to a simple calculation of the current weld power $P(t)$ as the temporal derivate of speed $\dot{\varphi}(t)$ [78]. Figure 3.4 depicts the calculated weld power and the course of the upset. It is observed that the generated power reaches a 200 kW peak early in the process, but the larger upset occurs at lower power levels of 150 kW.

Scaling the size (that is, the friction cross section A) within IFW processes of a certain material

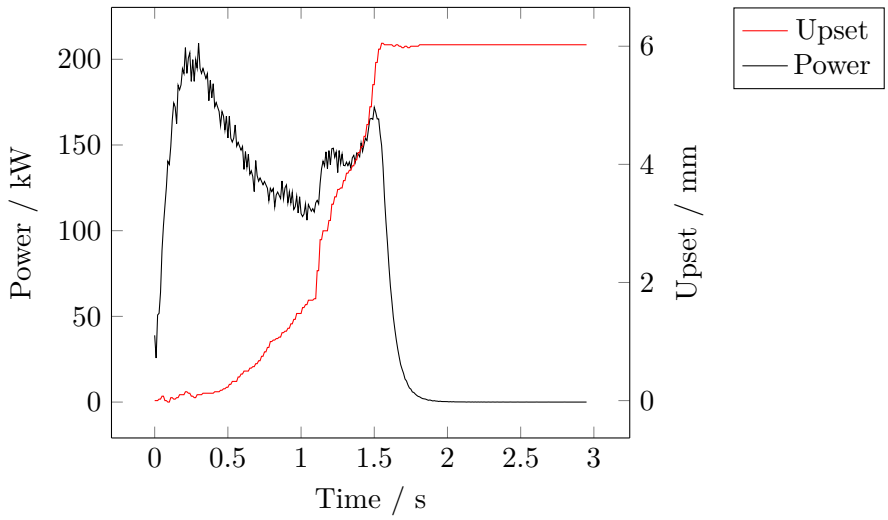

Figure 3.4: Upset and calculated power of an inertia welding process of a TZM tube

can be done by setting specific weld energy constant [78]:

$$\frac{E}{A} = const. \tag{3.3}$$

This approach could be adapted to roughly scale DDFW processes, too.

3.1.1.2 Direct drive friction welding

The process of direct drive rotary friction welding is split into three stages (figure 3.5): First, at the heat-up stage, the two parts are brought together and heated up through friction between them. Then, burn-off initiates, where the material starts to flow plastically and upsetting takes place. Finally, the relative motion stops and the two parts are forged together with an increased force until upsetting ceases and the welding process is completed.

In direct drive friction welding, friction time and speed are independent from friction pressure. Therefore, more welding parameters have to be determined, which may render finding a suitable set of parameters more challenging but simultaneously it is more versatile in process parameter variations. Compared to IFW in general, welding times are longer and friction pressures are lower owing to the limited torque and motor power [50].

The specific weld energy is the relevant parameter in IFW processes. This parameter can be calculated for DDFW process from the product of motor load and speed over time. However, due to the longer process times of DDFW, the heat dissipation becomes more significant compared to IFW. Defining the relevant time period to calculate the specific energy is essential to allow

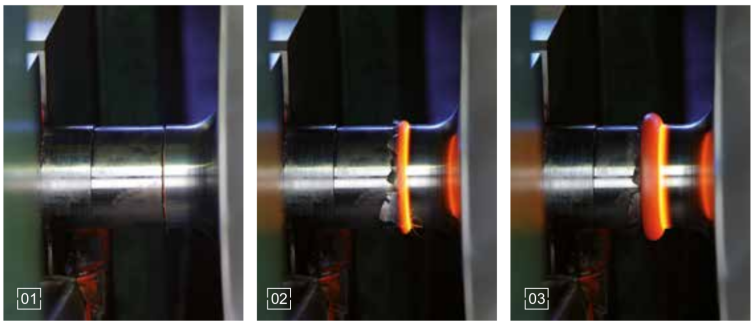

Figure 3.5: Three stages of RFW: (1) Heat-up, (2) burn-off, (3) forging [79]

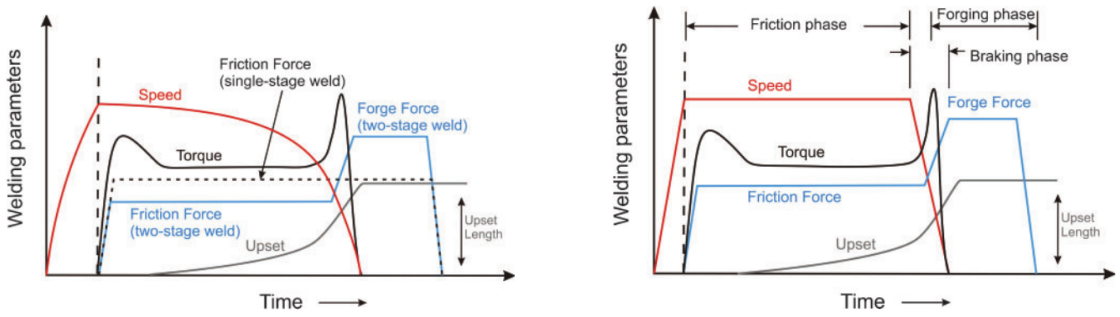

(a) (b)

Figure 3.6: Process parameter courses speed, torque, axial force, and upset of (a) IFW and (b) DDFW [80]

a rough comparison. As a consequence, a more detailed analysis of the power progression is necessary. Figure 3.6 shows typical process parameter courses of IFW in comparison to DDFW.

3.1.1.3 Process parameters of RFW

The DIN EN ISO 15620 standard [81] classifies welds of RFW according to the parameters listed in table 3.1.

Table 3.1: RFW parameters according to DIN EN ISO 15620 [81]

A) Raw part information		
B) Machine parameters		
Friction speed	n	min^{-1}
Pressure (heat-up)	p_{t1}	MPa (bar)
Pressure (rubbing)	p_{t2}	MPa (bar)
Friction force	F_t	kN
Pressure (burn-off)	p_{s1}	MPa (bar)
Upsetting force	F_f	kN
Time (heat-up)	t_{t1}	s
Time (rubbing)	t_{t2}	s
Upset	s	mm
Pressure (brake)	p_{s2}	MPa (bar)
Upsetting rate	r_s	$^{\mathrm{mm}}/_{\mathrm{s}}$
Instant of braking	t_{s1}	s
Instant of forging	t_{s2}	s
Time (forging)	t_f	s
C) Welded part information		
Upset total	s_w	mm
Weld time total	t_w	s

For easier denotation, we declare

$$\mathbf{p} := \begin{bmatrix} p_{t1} & p_{t2} & p_{s1} & p_{s2} \end{bmatrix} \tag{3.4}$$

and

$$\mathbf{t} := \begin{bmatrix} t_{t1} & t_{t2} & t_f \end{bmatrix}. \tag{3.5}$$

3.1.2 Friction

The fundamental understanding of friction dates back to *Leonardo da Vinci* (15^{th} century), *Guillaume Amontons*, and *Charles-Augustin de Coulomb* (both 17^{th} century), who first described the nature of friction as an effect of surface irregularities. As a result Amontons' law of friction (equation 3.6) was formulated, which is still a fundamental part of elementary mechanics [71, 82, 83].

$$F_R = \mu \cdot N \tag{3.6}$$

For dynamic friction this law declares that the force F_R resisting the movement is equal to the coefficient of friction μ times the normal load N, which is the force acting perpendicularly

to the touching surfaces. For basic kinematic problems, the friction coefficient can be assumed as a constant.

In reality, dry friction is a complex mechanism with many influencing factors, which is not fully understood yet. According to Stribeck [82], the friction coefficient is a function of sliding speed, as depicted in figure 3.7. The effect of the Stribeck curve on friction welding is that depending on the radial distance from the centerline the local heat generation varies. Moreover, a variation in welding speed shifts the maximum heat generation radially and the macroscopically observed heat source forms differently, as schematically drawn in figure 3.8.

Experimental data show that μ can both increase (Al–Al, Al–Cu, Al–brass) [84] or decrease (Al–steel) [85] with increasing normal loads and sliding speeds. In the latter experiments, μ increased and asymptotically converged [84, 85]. This diversity in literature is also observed in the friction coefficient of titanium; Lésniewski collected courses of the friction coefficient over temperature from different sources and found large differences, as observed in figure 3.9 [86]. It was further reported that in friction welding of mild steel, depending on friction speed, the coefficient of friction initially increased until a relative sliding speed of 0.5–1 $^{\mathrm{m}}/_{\mathrm{s}}$ before it continuously dropped with increasing speed [87].

As the temperature at the interface rises and approaches the melting point or the solidus temperature, respectively, the shear yield limit is reached and exceeded. In this case the relative motion between the welding interfaces ceases, sticking condition is present, and the material in the contact volume is plastically flowing. In this scope, the process of friction welding takes place.

If mostly the establishing temperature field is investigated, Amontons' law is often used successfully to describe the heat generation in friction welding [16, 90, 91]. Khosa found that the friction coefficient for a friction stir welding process of an Al6082 alloy correlates to the evolution of the yield strength over temperature and modeled the course of the coefficient accordingly [92],

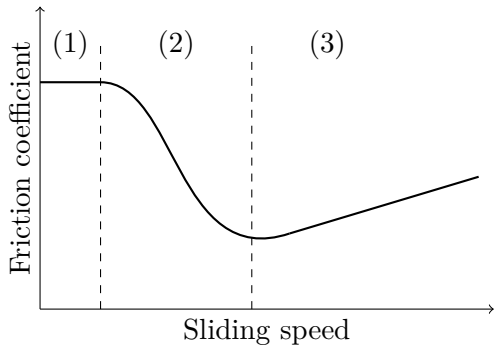

Figure 3.7: The Stribeck curve for solid friction with the three regions of (1) solid friction, (2) mixed friction, and (3) fluid friction [82, 83]

Figure 3.8: Heat generation in relation to speed: (a) High speed forms a heat "lens," while (b) low speed results in more heat generation in the outer region [50, 88, 89].

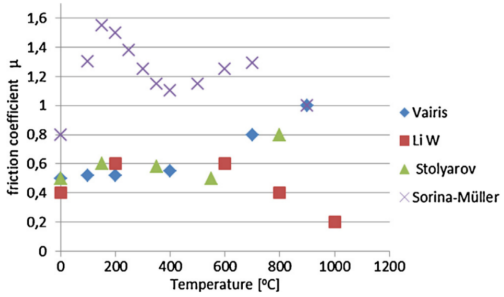

Figure 3.9: Course of the friction coefficient over temperature for Ti according to different sources, as collected by Lésniewski [86]

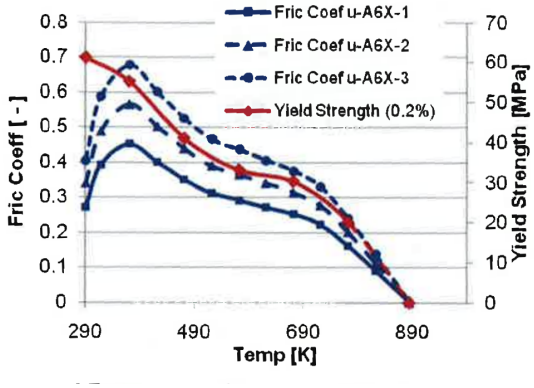

Figure 3.10: Assumed friction coefficient modeled to fit the yield stress for Al6082-T6 [92]

as depicted in figure 3.10. However, because the tool in friction stir welding does not melt and only deforms elastically, the assumption that heat is generated by Coulomb friction with a resulting, but thermally detached plastic flow of the material from the tool is justifiable.

3.1.3 Plastic flow

The assumption that the heat $\mathrm{d}Q$ (here in differential form) is generated solely from the dissipation by the friction force μN times the path-dependent distance δs in the form of

$$\mathrm{d}Q = \mu(T) N \delta s \tag{3.7}$$

is not only insufficient but physically incorrect [75, 80, 93, 94]. Basically, the closer the melting temperature T_m is approached, the more heat is generated by dissipation of inner stresses. If the plastically deforming volume is interpreted as a fluid flow, the dissipation of shear stresses is written as

$$\dot{q} = \nabla \left(\boldsymbol{\tau} \cdot \mathbf{u} \right), \tag{3.8}$$

containing the shear stress tensor $\boldsymbol{\tau}$ and the flow velocity vector $\mathbf{u}$. Then, depending on temperature and condition, in friction welding the conversion of drive power into heat writes as

$$P = \mu(T) N \frac{\delta s}{\mathrm{d}t} + \int_V \nabla(\boldsymbol{\tau} \cdot \mathbf{u}) \mathrm{d}V, \tag{3.9}$$

where $\frac{\delta s}{\mathrm{d}t} = r\dot{\varphi}$ in case of rotary motion and $\mathbf{u}$ is the material flow velocity vector field in the plastically deforming zone. In a certain stage of the welding process we can assume sticking

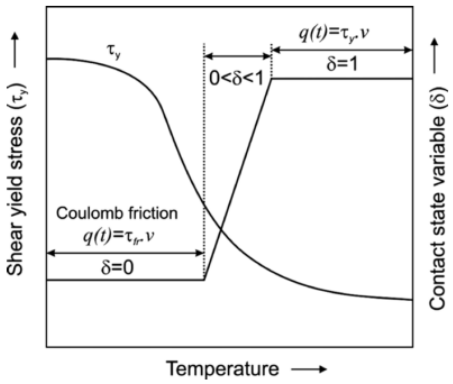

Figure 3.11: Transition from Coulomb friction to plastic flow as a function of temperature [95]

condition at the interface, which means that the entire domain can only generate heat from shear dissipation. Maalekian et al. [75, 95] argued that the transition from Coulomb friction to plastic flow can be modeled by employing a state variable δ that gradually changes from 0 to 1 in the proximity of the shear yield stress τ_y, as depicted in figure 3.11.

3.1.3.1 Continuum mechanics and fluid dynamics approach

In Newtonian fluids the dynamic viscosity η is independent from the deformation rate [83]. Then the shear stress tensor $\boldsymbol{\tau}$ can be written as

$$\boldsymbol{\tau} = \eta \nabla \mathbf{u}. \tag{3.10}$$

For η as a function of temperature, Osborne Reynolds [96] proposed a simple empirical model in form of the exponential function

$$\eta(T) = \eta_0 \cdot e^{-bT}, \tag{3.11}$$

with the coefficients η_0 and b.

Since the plastic flow in rotary friction welding is non-Newtonian, the relation between shear stress and motion has to be described differently, for instance according to the Ostwald-de-Waele law, with

$$\tau = \eta(\nabla \dot{\varphi})^n. \tag{3.12}$$

For FSW, Roubidoux and Mendez et al. [97, 98] noted that the constitutive equation

$$\dot{\gamma} = A\tau^n e^{-\frac{B}{T}}, \tag{3.13}$$

based on the constitutive equation of Sellars and McTegart [99], yields a sufficient relation of the shear rate $\dot{\gamma}$ to the shear stress τ using the empirical constants A and B.

Schmicker et al. formulated a viscoplastic material model based on Carreau's fluid consitutive assumption [100, 101]:

$$\eta(\dot{\varepsilon}_{vM}, T) = \left(1 + \left(\left(\frac{\sigma_0(T)}{3\dot{\varepsilon}_0\mu_0}\right)^{\frac{n}{1-n}} \frac{\dot{\varepsilon}_{vM}}{\dot{\varepsilon}_0}\right)^2\right)^{\frac{1-n}{2n}} (\eta_0 - \eta_\infty) + \eta_\infty \tag{3.14}$$

This enables to approximate friction by a virtual viscosity depending on the *von Mises* strain rate and the temperature and therefore it is non-Newtonian. The von Mises strain rate is

$$\dot{\varepsilon}_{vM} = \sqrt{\frac{2}{3}\mathbf{D} : \mathbf{D}} \tag{3.15}$$

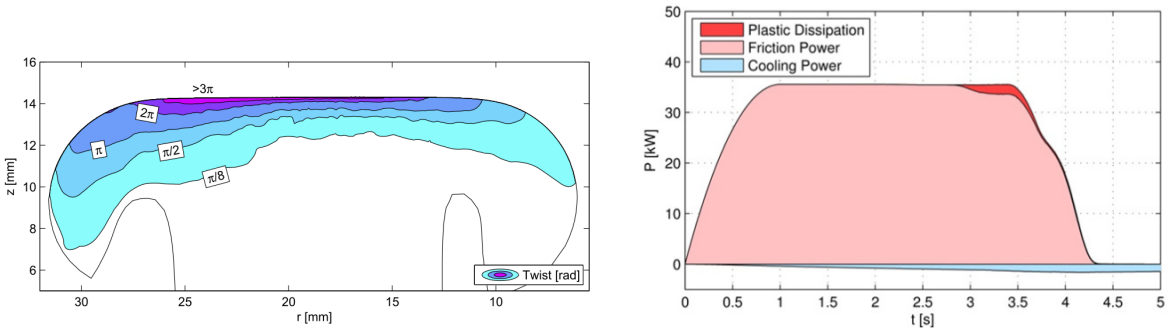

(a) (b)

Figure 3.12: (a) Modeled rotary shear deformation ("twist") of the weld and (b) exemplary graph of the heat generation by plastic dissipation and friction, and also cooling by convection, radiation, and conduction in a RFW simulation [101, 102]

with the Frobenius inner product of the strain rate tensor $\mathbf{D}$ with itself and thus takes into account the shear strains [101, 102]. Boundary conditions of saturation viscosities η_0 and η_∞ enable a modeling of the course despite the singularities of $\dot{\varepsilon}_{vM} \to 0$, $\dot{\varepsilon}_{vM} \to \infty$, and temperatures higher than T_m. Schmicker's approach yielded good qualitative results and showed that the rotary shear deformation is multiple magnitudes above the deformation in the r–z plane, as shown in figure 3.12a [101]. It was stated as well that shear stresses should not be neglected although it appears from figure 3.12b [102] that the generated heat is much less than from friction, which would be a direct contradiction to the work of Zhang [94] and Maalekian [75, 95]. Considering that friction is represented by $\eta(\dot{\varepsilon}_{vM}, T)$ (equation 3.14), the friction heat also results from a viscous flow involving the *von Mises* strain rate. This means that this model does not directly state the part that results from shear deformation.

3.1.3.2 Estimation of shear rates in the plasticized zone

Sellars and McTegart introduced a constitutive power law relation between the shear rate $\dot{\gamma}$, the shear stress τ, and the temperature T [99]. Roubidoux and Mendez et al. suggested that for a rough estimation of the occurring shear rates in FSW, the relation can be divided into two regimes: one with negligible shear and one that bears the entire deformation [97, 98]. Figure 3.13 shows the relation schematically, with the melting temperature T_m and the temperature at the interface between pin and substrate T_s. In this model, the material starts to plasticize if a certain temperature threshold T_0 is exceeded. The temperature T_0 which divides the two regimes is then calculated by a linear approximation of the Sellars–McTegart power ansatz.

For the following approximation, RFW of a thin-walled tube is examined. The approach of Mendez et al. [98] is slightly changed; T_{max} shall be the temperature at the welding interface, thus the maximum occurring temperature instead of necessarily the melting temperature. Labeling the maximally occurring shear rate $\dot{\gamma}_{max}$ at T_{max}, the linear interpolation of the shear-rate-to-temperature relation writes as

$$\dot{\gamma}(T) = \frac{\dot{\gamma}_{max}}{T_{max} - T_0} \cdot (T - T_0). \tag{3.16}$$

Further, because a thin-walled tube is considered, the temperature can be assumed constant in r-direction. In literature, the temperature distribution in x-direction in the shearing weld parts is often assumed as a Gaussian normal distribution function [103], schematically sketched

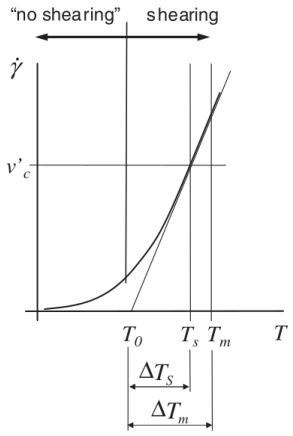

Figure 3.13: The shear rate $\dot{\gamma}$ as a function of the temperature T. The exponential relation is divided into two regimes and linearized between T_m and T_s to determine T_0 [98].

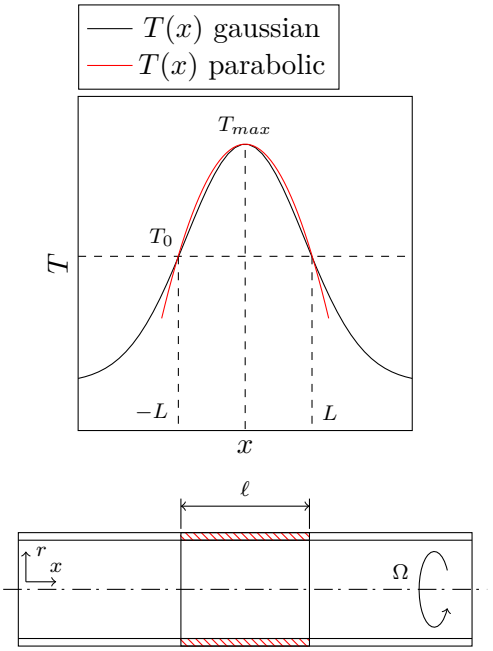

Figure 3.14: Temperature course in the plasticizing zone of the welding parts approximated by a parabolic function

in figure 3.14. For mathematical simplification, the temperature distribution in that interval is fitted by a parabolic function, as drawn in red in figure 3.14. The deforming volume is contained in the interval $[-L, L]$ which exceeds the critical temperature T_0. Using the boundary conditions $T(-L) = T(L) = T_0$ and $T(0) = T_{max}$, the temperature course is

$$T(x) = \frac{T_0 - T_{max}}{L^2} \cdot x^2 + T_{max}. \tag{3.17}$$

Combining equations 3.16 and 3.17 gives the shear rate as a function of x with

$$\dot{\gamma}(x) = \dot{\gamma}_{max} \left(1 - \frac{x^2}{L^2}\right), \tag{3.18}$$

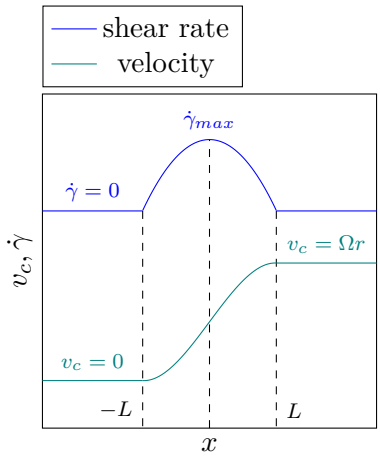

Figure 3.15: Shear rate and local circumferential velocity in the plasticizing zone

wherein only $\dot{\gamma}_{max}$ remains unknown. Naturally, the course of the shear rate is also parabolic, as drawn in blue in figure 3.15.

In the rotary part the speed Ω is constant and the circumferential velocity is calculated with

$$v_c = \Omega r. \tag{3.19}$$

Considering figure 3.15, the speed of the stationary part is zero, therefore the cumulated shear rate in the interval $[-L, L]$ must yield the velocity v_c, mathematically expressed as

$$\int_{-L}^{L} \dot{\gamma}(x)\mathrm{d}x = v_c. \tag{3.20}$$

This integral bears the required boundary condition and can be calculated using equations 3.18. After some algebra and re-substituting equation 3.19, the maximum occurring shear rate is finally given with

$$\dot{\gamma}_{max} = \frac{3\Omega r}{4L} = \frac{3\Omega r}{2\ell}. \tag{3.21}$$

It is noteworthy that this equation is explicitly independent of the values T_{max} and T_0 and only a function of the welding speed Ω, the tube radius r, and the length of the deforming volume $\ell = 2L$. Using this insight, a rough estimation of the maximum occurring shear rate is possible, determining ℓ as the visibly deformed microstructure from macrosections of welded specimens.

The calculation of the shear rate becomes more complex, if a full cross section is considered instead of a thin-walled tube. However, presupposing a constant temperature distribution in r-direction, the maximum shear rate can be expected to occur on the perimeter of a full cross section.

3.1.4 Material behavior in friction welding

In the previous section theoretical considerations about friction welding were discussed. It was shown that it is rather complex to describe the behavior on a theoretical basis. Duffin and Bahrani [87] considered various experiments to study the influence of welding parameters on the friction welding behavior of mild steel tubes. More specifically, they discussed the response of the different welding phases to welding parameter changes. Figure 3.16 shows typical courses of the main process parameters speed, pressure, torque, and upset with the different phases of the process indicated.

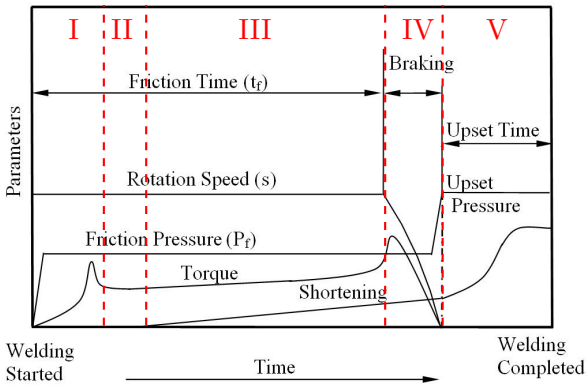

Figure 3.16: Direct drive friction welding parameters over time, with indicated stages (I) heat-up, (II) burn-off, (III) equilibrium, (IV) transition, and (V) forging [87, 104]

3.1.4.1 Phase I: contact

The initial contact of the material results in abrasion and flattening of the joining areas. This results in the torque rising rapidly and subsequently falling down to a lower value. These phenomena are called initial peak torque and equilibrium torque and are observed in every material [80, 87]. In mild steel, Duffin observed that the initial peak torque reached a maximum between 0.8 and 1.0 $^{m}/_{s}$ mean rubbing speed. With rising speed, the initial torque decreased [87].

3.1.4.2 Phase II: upset start

After a short period in equilibrium torque, the volume close to the rubbing interface exceeds the shear strength and axial shortening (upsetting) commences.

3.1.4.3 Phase III: equilibrium

As material gets displaced, cooler material is pushed towards the rubbing interface and a constant upset rate attunes.

The magnitude of the upset rate was reported to be in close connection with the torque and was high at low speeds and low at high speeds, respectively. At low speeds, high upset rates were observed, whereas at high speeds, low upset rates occurred. A different behavior of mild steel depending on welding speed manifested in a way that low speeds caused a viscous flow and high speed resulted in a forge-like behavior. The lower speed threshold of the process was also increased if the axial force was increased [87].

3.1.4.4 Phase IV: transition

After the friction phase, the rotary motion is halted quickly and the axial force is increased from friction level to forge level. In general, two strategies exist: Conventional transition, where the motion is halted and subsequent increase of the force, and "forging into the turning spindle," where the force is increased while the rotary part is still in motion. The delay of the spindle stop shall be denoted as the "deceleration delay" Δt_d in seconds difference between spindle braking start and axial force increase.

The transition from welding speed to zero inflicts the aforementioned effects of rubbing at lower speeds, which causes a higher upset rate. The connected peaking of resisting torque is called

terminal torque. Combined with a higher axial force in the case of forging into the turning spindle, the latter effect is magnified even further. The details of this phase have only been investigated to some extent, but mostly the focus of investigations lied on friction and forge phases [80, 87].

3.1.4.5 Phase V: forging

The increased force results in a rapid plastic deformation and the final formation of the displacement collar, the so called welding flash. The forge force is held and the weld cools down as no more energy is fed into the joint. The upsetting stops and the process is complete.

3.1.4.6 Thermo-mechanically affected zone

At friction welding no melting occurs. Therefore the thermo-mechanically affected zone (TMAZ, i.e. heat affected zone) becomes the weld. As an effect of the process parameters, the material properties, and the process boundary conditions, the entire TMAZ experiences large deformation with larger deformation in regions with higher temperature. Figure 3.17 illustrates the different regions [80].

1. **Contact zone:** friction reaction and heat generation, severe plastic deformation, high strain, full recrystallization, fine grains
2. **Fully plasticized zone:** considerable plastic deformation, dynamic recrystallization, refined grains
3. **Partly deformed zone:** lower strain rate, temperature, and plastic deformation than in zone (2), grain coarsening
4. **Undeformed zone:** no plastic deformation, possibly grain growth or phase transitions depending on the material and the temperature level
5. **Base metal:** thermo-mechanically unaffected base metal

3.1.5 Molybdenum and its alloys

For IFW, literature states a minimum critical specific welding power of 144.38 $^{W}/_{mm^2}$ with a minimum critical initial welding speed of 10.2 $^{m}/_{s}$ [50]. Felix et al. published comprehensive welding parameters and results for IFW of various Mo–Re alloys [51].

Ambroziak [7] welded similar-metal Mo and TZM under a liquid coolant (oil IME 82) and reported that the microhardness increased from 220–230 HV0.05 to 260HV 0.05 in the area of the weld zone of Mo–Mo joints. Also a very fine-grained, recrystallized microstructure was observed.

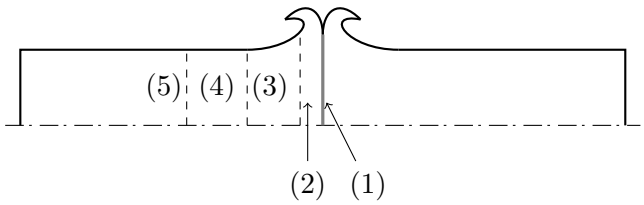

Figure 3.17: Different zones of a RFW weld: (1) Contact zone, (2) fully plasticized zone, (3) partly deformed zone, (4) undeformed zone, and (5) base metal [80]

Comparing Mo–Mo to TZM–TZM joints, a wider heat affected zone (HAZ) developed in TZM–TZM, due to the lower friction coefficient of TZM, causing a steadier rise of temperature. TZM–TZM also showed a decrease in microhardness, from 350 HV0.05 to 250 HV0.05 in the weld zone and 220 HV0.05 in the HAZ. The welding process was conducted with the parameters $n = 1500\,\mathrm{min}^{-1}$, $\mathbf{p} = \begin{bmatrix}27 & 41 & 82 & 102\end{bmatrix}$ MPa, and $\mathbf{t} = \begin{bmatrix}3.5 & 16.4 & 30\end{bmatrix}$ s.

Tabernig and Reheis [14] reported on direct drive RFW of TZM and MHC alloys. They welded ⌀15 mm and ⌀20 mm rod material at speeds between 2,500 and 6,000 min^{-1} at 60–70 MPa friction pressure, 100 MPa forge pressure (TZM), and 180–225 MPa for MHC, respectively. Comparable mechanical properties of the welds to the base metal were observed. Further, an up-scale and transfer to ⌀100 mm tube material with a thickness of 12 mm welded by IFW was successfully achieved.

Caldwell et al. discussed the same rotary friction welds of ⌀15 mm TZM rod material [14], as observed in figure 3.18 [52][1]. Post-weld heat treatment was reported to relief residual stresses from welding and was therefore recommended.

In the course of a Master's thesis at the IMAT [16], RFW of TZM was investigated. The specimens were preheated to 390°C, welded, and finally post weld heat treated in a high-vacuum furnace at 1,550°C for 1.5 h. The resulting hardness values showed an increase from 180 HV10 in the base material to about 220–230 HV10 in the weld zone, although similar welding parameters n =1,500 min^{-1}, $\mathbf{p} = \begin{bmatrix}- & 63 & - & 268\end{bmatrix}$ MPa, and $\mathbf{t} = \begin{bmatrix}- & 3 & 10\end{bmatrix}$ s as in Ambroziak's experiments. First, apart from different hardness measuring levels (HV0.05 vs. HV10), the base metals apparently differed from each other, regarding the hardnesses. Second, since the temperature of post-weld heat treatment of the latter experiments was well above the the recrystallization temperature of TZM, and Ambroziak apparently conducted no post-weld heat treatment, the results differ.

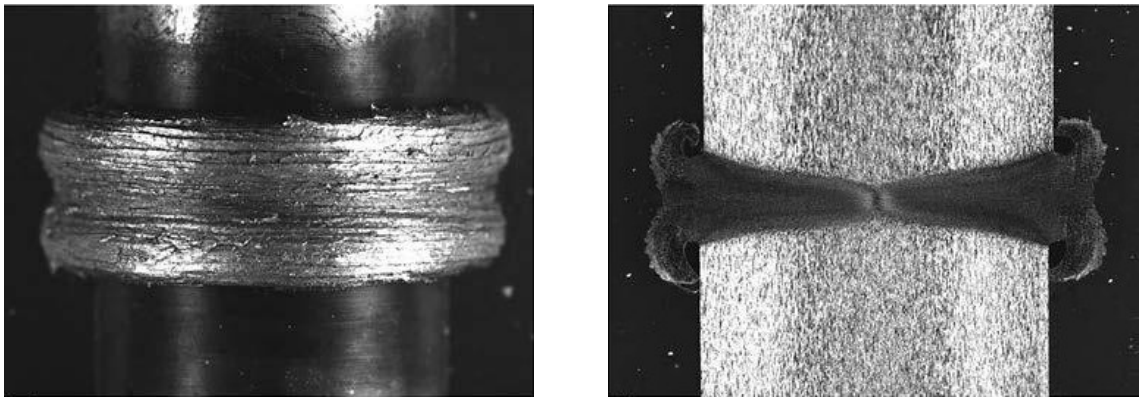

(a) (b)

Figure 3.18: Images of RF welded ⌀15 mm TZM rod material: (a) flash morphology and (b) macrosection [14, 52]

[1] In this article, RFW is misquoted as "friction stir welding."

3.2 Experimental

3.2.1 Tube format friction welding

Pure Mo sputter targets are made from large tubes of 5,000 mm^2 and more. Pure Mo tubes and S235 structural steel tubes with a dimension of $\varnothing 130 \times 10$ mm were selected to carry out welding experiments on a heavy duty direct drive rotary friction welding machine at the project partner *Klaus Raiser GmbH & Co. KG*, located in Eberdingen, Germany.

The machine *HR 1250* has a maximum capability of 1,250 kN axial force, 900 min^{-1} speed, and 150 kW drive power. The clamping of the Mo tubes is shown in figure 3.19. Pre-heating of the samples was conducted in a separate furnace to 450°C. The machine was fitted with measuring equipment to record the most relevant experimental data axial force, upset, motor load, motor speed, spindle speed, and temperature profiles in different positions. With this setup, a maximum specific welding power of 34.1 $^{W}/_{mm^2}$ at 850 min^{-1} was achievable.

The results of the successful welds were characterized using visual inspection, ultrasonic tests, metallographic investigations, and hardness measurements. Apart from the latter, no mechanical testing was done, as the main challenge proved to be to deliver a successful welding process in general.

3.2.2 Rod format friction welding

The recordable and adjustable welding parameters in the industrial welding machine at *Klaus Raiser GmbH & Co. KG* were limited, due to its main purpose of serial production. To investigate the RFW behavior of pure Mo and also TZM further, an extensive investigation on the friction stir welding (FSW) machine at the institute was implemented. For that purpose, the *MTS I-STIR BR4* FSW machine was adapted to conduct rotary friction welding.

The experiments in laboratory size bore a number of benefits: First, the FSW machine at the institute comprises comprehensive parameter recording like spindle speed, axial force, torque, motor power, or axial travel. Further, a precise control of speed, deceleration, force, and force gradients was available. The maximum machine capabilities were an axial force of 35.6 kN, a spindle speed of 3,200 min^{-1}, a torque of 180 Nm, and an effective axial travel of 16 mm. Due to the limited power compared to the *HR 1250* machine, the format had to be changed to a smaller dimension.

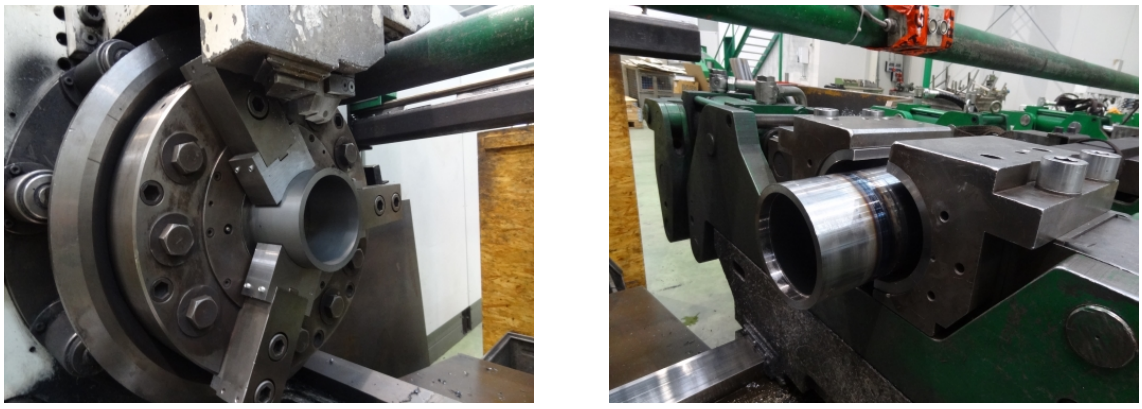

(a) (b)

Figure 3.19: Clamping in the *HR 1250* RFW machine, (a) the rotary part clamped by a 3-jaw chuck in the spindle and (b) the stationary part clamped by semi-shells

Pure Mo rods of ∅12 mm and TZM rods of ∅9 mm were selected and welded. The available power for the given cross sections equaled 159 $^{W}/_{mm^2}$ for ∅12 mm and 287 $^{W}/_{mm^2}$ for ∅9 mm. On the downside, the small diameters meant that a maximum circumferential speed of only 2 and 1.5 $^{m}/_{s}$, respectively, was possible.

Figure 3.20 shows a schematic setup of the FSW machine for the RFW experiments: The FSW tool was replaced by a clamping sleeve that held the rotary part. Fixation was accomplished by a bolt that pressed against a flat section of the part. The stationary part was clamped by a three-chuck jaw that was fixed on the machine table. Photographs of the experimental setup are shown in figure 3.21.

The main emphasis was to study the process parameter interactions and their influences on the welding result. The final welds were characterized by visual inspections, metallographic investigations, and hardness maps in selected cases.

3.2.3 Simulation of friction welding

The goal of the simulation was to reproduce an existing RFW process numerically.After a first assessment, the software suite DEFORM was utilized for the simulation of RFW of molybdenum. A series of adaptations was necessary, as the high temperature behavior of Mo was unknown and a proper heat source model was missing. The simulation was based on a rod format experiment of which comprehensive welding parameter records existed [105].

The material behavior was modeled with temperature-dependent data of Young's modulus, density, specific heat capacity, and thermal conductivity [12]; The temperature- and strain rate dependent flow stress resulted from a Zerilli–Armstrong flow stress model with the obtained coefficients in table 2.8 on page 28 of chapter 2. Although the flow stress of the Z–A model does not recognize an asymptote of zero stress at the melting temperature, one could argue that since the melting temperature is not reached in friction welding, sufficiently accurate flow stress could be predicted by this model.

On the other hand, because the material flow behavior was modeled and strictly extrapolated without experimental validation, it seemed too unreliable to invoke a heat source based on the

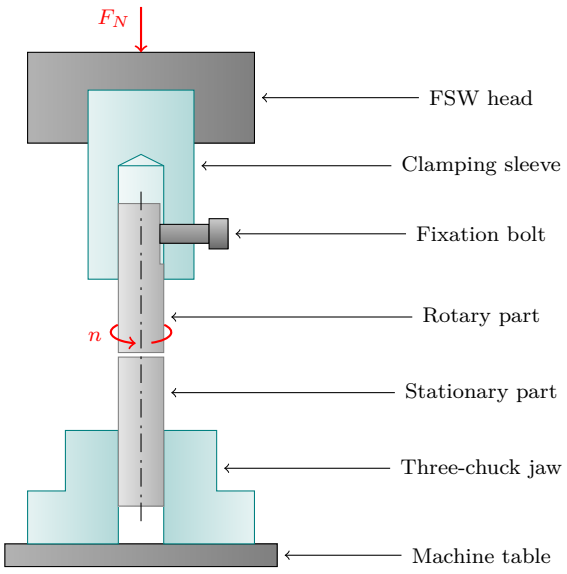

Figure 3.20: Schematic setup of the FSW for RFW experiments

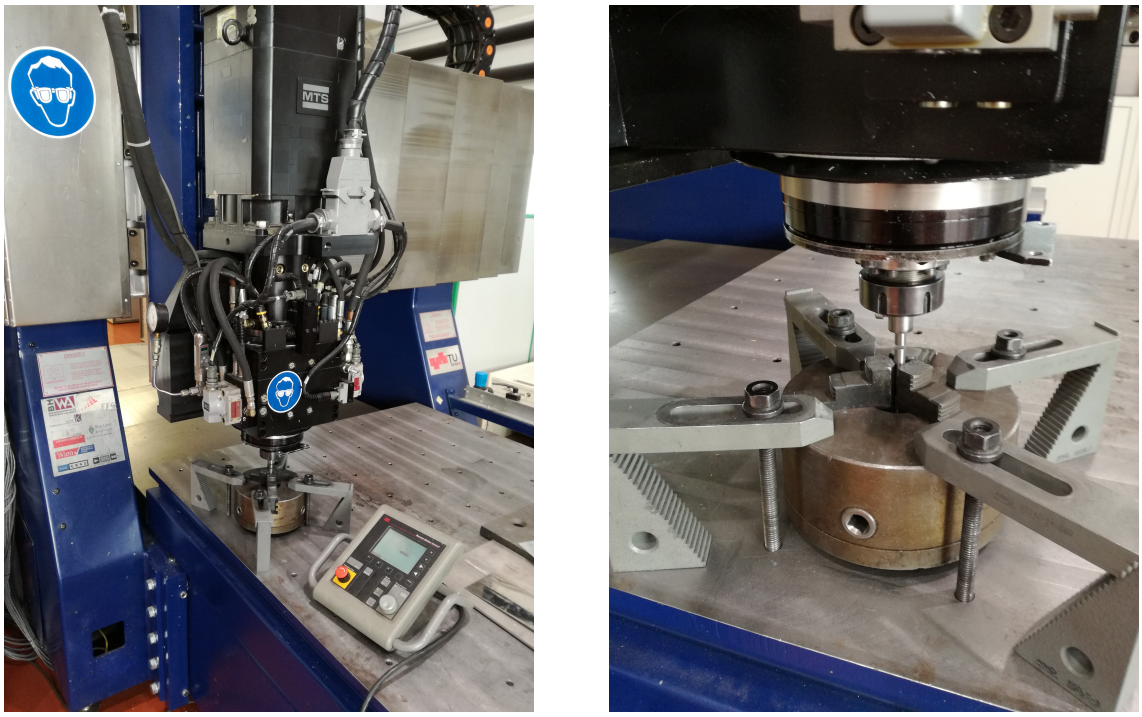

(a) (b)

Figure 3.21: Setup of the FSW machine for RFW experiments [105]

deformation, although it yielded good results in the literature [101,102,106]. Therefore, the heat source model was replaced by an area heat source with the power course values obtained by the experiment [105]. The second input parameter was upset, that is the recorded axial displacement of the experiment, as depicted in figure 3.22.

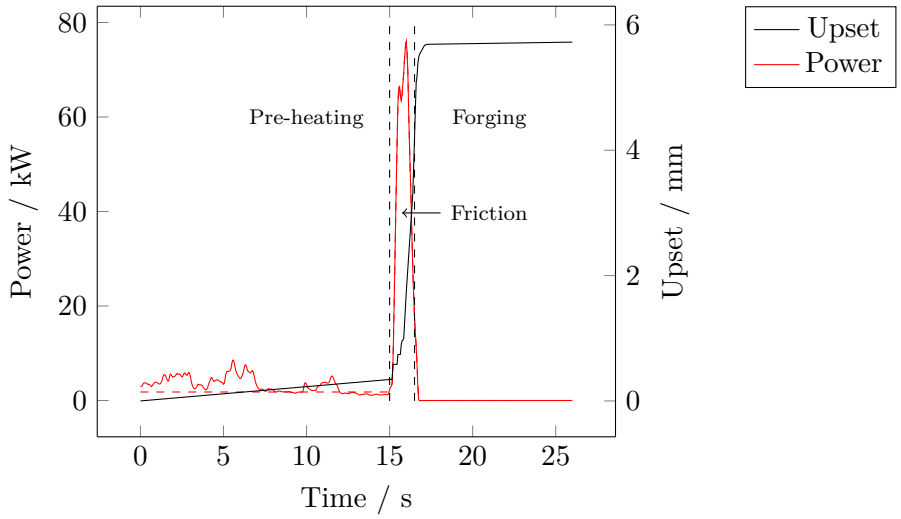

Figure 3.22: Input parameters for the simulation: Power and upset; the power course was flattened in the pre-heating phase (dashed line)

The process was simplified on two symmetry accounts: First, the symmetry on the rotary axis, which leads to a 2d axisymmetric model. Second, due to the equal deformation of the two parts the rotating counterpart was replaced by a rigid part without heat transfer and friction. The simulation setup itself was a 2.5d model which takes into account the increasing volume and contact area with increasing radial distance from the rotary axis. The model consisted of 1,000 rectangular elements with a refined mesh at the contact zone and a variable step width of 0.03 s from 0–15 s and 18–26 s, and 0.005 s from 15–18 s, accounting to a total of 1,366 simulation steps. The DEFORM built-in remeshing sequence was also incorporated to enable larger strains. Boundary conditions were set as follows and depicted in figure 3.23.

1. The heat source $\dot{q}$ was equally distributed over the top surface and the power course was adopted from a rod format experiment, reduced by the losses of the drive train, as observed in figure 3.22. The pre-heating stage at a low friction pressure was included to establish the temperature field prior to the welding stage, which is observed with a low power value from 0 to 15 s. Note that the power values of the experiment have to be halved for the input value of the simulation because of the symmetry of the stationary and rotating part.

2. The rotating part is replaced by a rigid body which acts as a "mirror." The friction and heat transfer between top die (rotating part) and workpiece was therefore set to 0.

3. Heat exchange with ambience was modeled with a convection coefficient of 20 $^{\mathrm{W}}/_{\mathrm{mm^2\,K}}$ and an emissivity of 0.18.

4. $\lambda = 15\ ^{\mathrm{W}}/_{\mathrm{mm\,K}}$ was used for the heat conduction to the bottom die which acts as a heat sink that represents the clamping system.

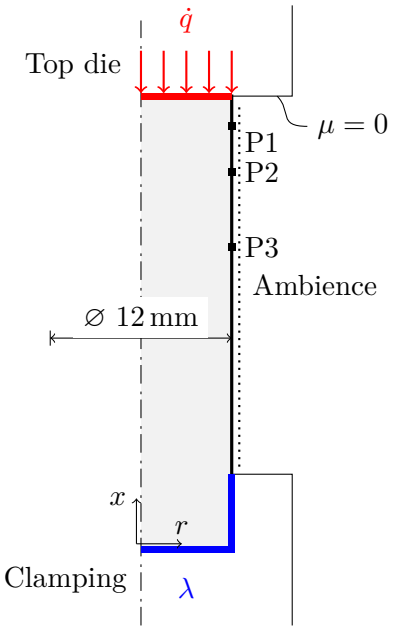

Figure 3.23: Schematic setup of the numerical simulation of RFW

3.3 Results

3.3.1 Tube format friction welding

3.3.1.1 Welding parameters

For a better basis of the Mo investigations, preliminary welding experiments using conventional S235 steel tubes were performed. Figure 3.24 shows a schematic of the axial pressure courses and the speed. At the process start the friction pressure level was approached by a pressure ramp to soften the initial torque peak. The forge pressure was initiated when the spindle came to a stop.

3.25 shows the axial pressure and the resulting upset course of experiment R0-02. The process design was at a welding speed of 765 min^{-1}, an axial pressure ramp of 0 to 30 MPa (0–130 kN) over 3 s to overcome the initial torque peak, then the friction phase for 9 s at an axial pressure of 52 MPa (230 kN), and finally a 3 s-ramp to the final forge pressure of 239 MPa (1,050 kN). As observed, the upsetting started right with the increase to friction force and within 2 s an equilibrium upset rate of 1.4 $^{\mathrm{mm}}/_{\mathrm{s}}$ established. The final upset was 22.4 s. The process ran stably and reproducibly, with an objectively good final welding result.

For molybdenum tubes the process parameters had to be altered: The first experimental series showed that the molybdenum tubes plasticized extensively after a short period of heating. The plasticization was so severe that it consumed the entire drive power of 150 kW and the spindle started to decelerate and even came to a halt. The friction time was reduced to 5 s and the friction pressure was reduced as well. However, even a reduction of the friction pressure to the lowest feasible level of 2.3 MPa (10 kN) of the machine did not improve the welding behavior. Temperature measurements showed a steep increase of temperature to 2,000°C and onwards. In the same regime upsetting started and quickly rose up to 7 $^{\mathrm{mm}}/_{\mathrm{s}}$ in some experiments. As the maximum upset rate occurred while the spindle was decelerating it is difficult to refer to it as “equilibrium upset rate” in the conventional manner, it is the “terminal upset rate,” determined by the quasi-equilibrium between maximum drive power, decelerating spindle, and plasticization.

Figure 3.26 shows the measured axial pressures and the resulting upsets of three experiments. As observed in figure 3.26a, different levels of axial pressure (ramp 9.1–18.2 MPa, constant 2.3 MPa, ramp 5.7–6.8 MPa) did not influence the general upset behavior as shown in figure

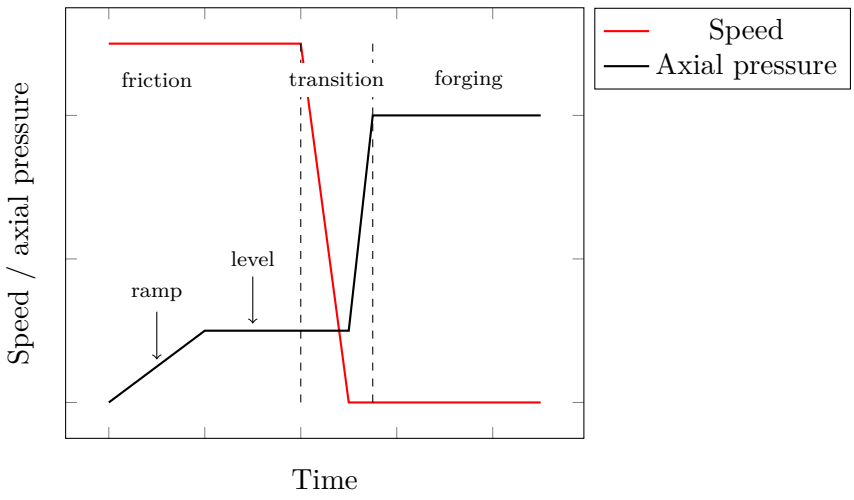

Figure 3.24: Schematic courses of the tube format experiment

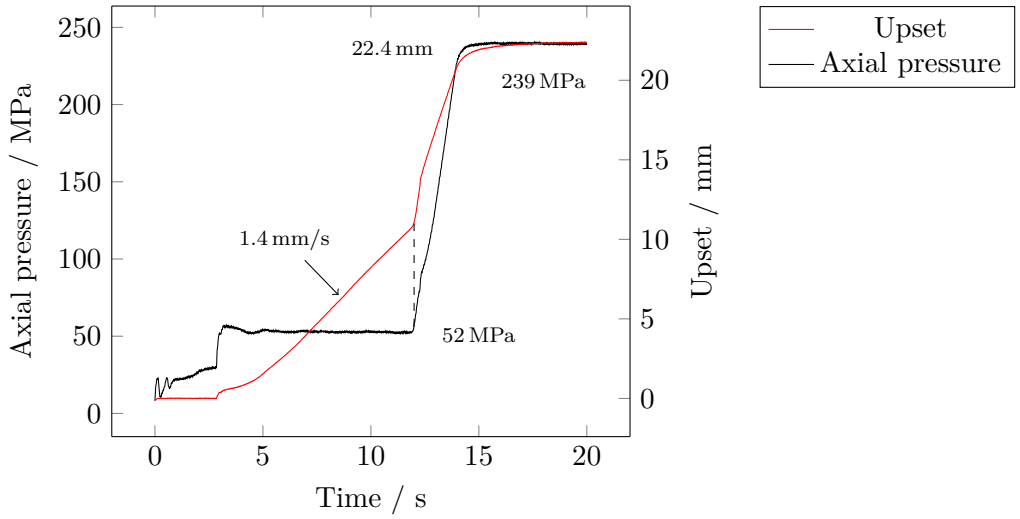

Figure 3.25: Measured force and upset courses of the preliminary S235 experiment R0-02: An equilibrium upset rate is observed.

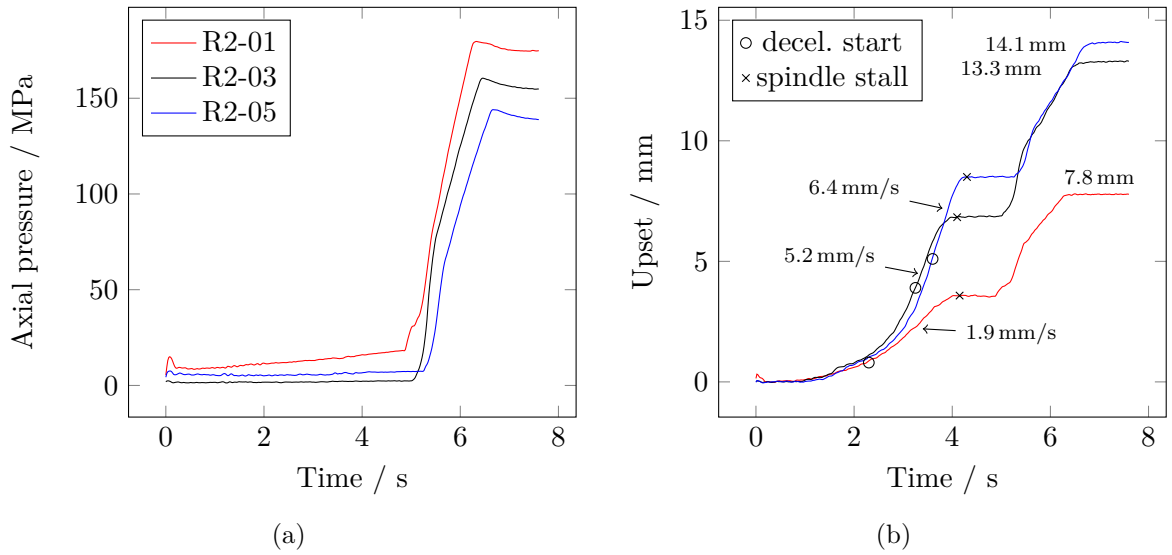

Figure 3.26: (a) Axial force and (b) resulting upset courses of tube format experiments R2-01, R2-03, and R2-05

3.26b. The terminal upset rates varied from 1.9 to 6.4 $^{mm}/_{s}$. Experiment R2-01 shows a shallower upset rate because the deceleration in this experiment commenced earlier as indicated by the circles in the figure. Further, a plateau in all three upset courses was observed which was due to the time period where the spindle was already stationary but the upset force was not initiated yet. It can be assumed that the Mo tubes start to plasticize and the upset rate increases as observed, intentioned to reach its equilibrium upset rate. Above a certain value the drive power is too low, and the discussed quasi-equilibrium establishes, where the upset rate stays constant until the spindle comes to a halt.

Figure 3.27a shows the measured axial pressure and upset of experiment R1-13 with a welding speed of 495 min^{-1}, a friction pressure ramp from 10.7 to 13.4 MPa (47–70 kN), and a forge pressure of 152 MPa (670 kN). It is observed that the start of upsetting coincides with the time

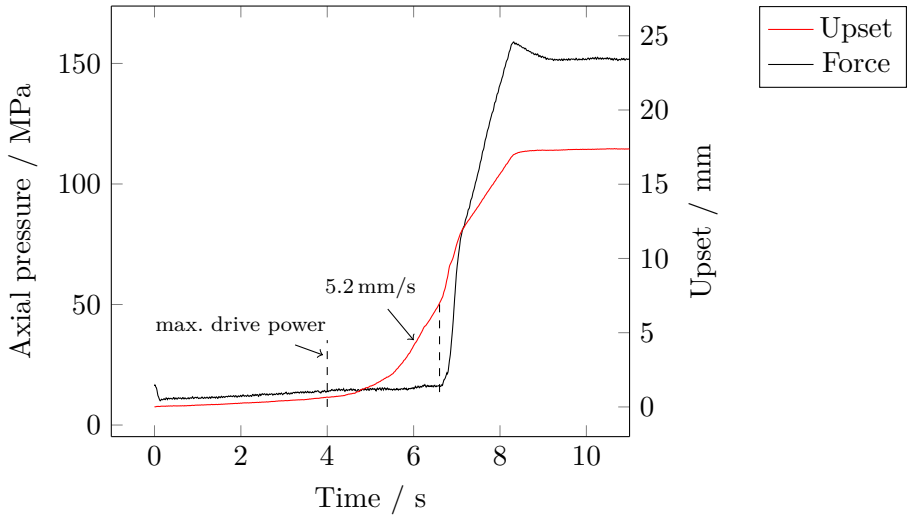

(a)

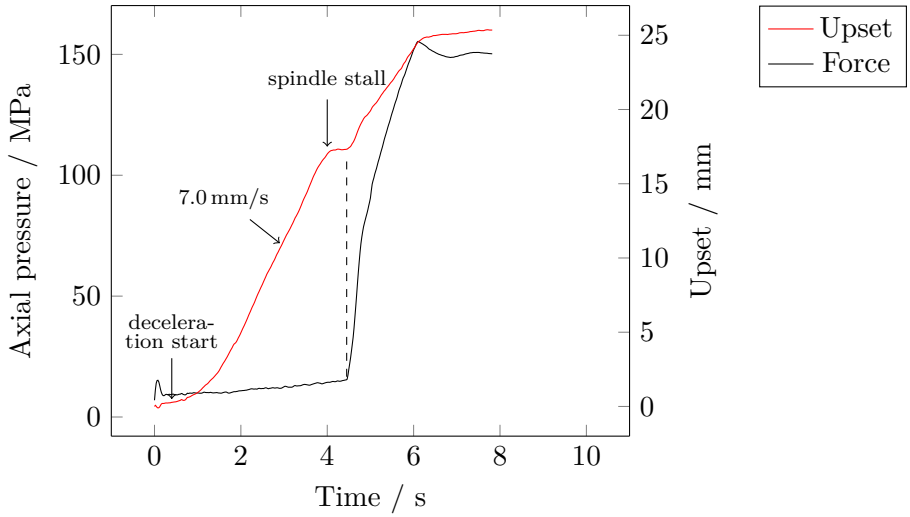

(b)

Figure 3.27: Measured force and upset courses of the tube format experiment (a) R1-13: A terminal upset rate of 5.2 $^{mm}/_{s}$ is observed at 6 s; (b) R2-13: A terminal upset rate of 7.0 $^{mm}/_{s}$ is observed.

from which on the maximum drive power occurs. The upset course quickly increases to a terminal upset rate of 5.2 $^{mm}/_{s}$ until the forge phase was initiated automatically and the final upset of 17.4 mm was reached. Roughly two thirds of the upset occurred in the forge phase.

Figure 3.27b shows the axial pressure and the upset of experiment R2-13 in which experiment R1-13 was reproduced, but with an increased welding speed of 850 min^{-1}. Further, the weld parts were pre-heated in a furnace to 450°C. Note that due to the manual step of clamping the welding parts in the machine, the Mo tubes readily cooled down to approximately 150°C before the welding cycle started.

Comparing the present experiment R2-13 to R1-13, a number of differences are observed: First, plasticization and upsetting started after 0.3 s friction time, at which the spindle decelerated

again due to a motor overload. Second, the resulting terminal upset rate is approximately 7 $^{mm}/_{s}$, which is notably higher than the 5.2 $^{mm}/_{s}$ of experiment R1-13. The final upset is 25 mm, which is also higher than in R1-13. Only one third of the total upset of 25 mm occurred in the forge phase.

Because of these observations it may be assumed that pre-heating causes the material to reach the shear limit earlier and accordingly, upsetting occurs earlier as well. If it is assumed that due to the pre-existing higher temperature in both welding parts, a larger volume is plasticized, the higher upset rate may be explained. The higher speed is accompanied in a larger amount of energy stored in the inertia of the drive that can be dispatched during the spindle deceleration, which also contributes to the upset rate.

It is assumed that the required power for the spindle run-up is eventually transfered into the weld and machine friction losses can be neglected. Then, if the motor power is integrated over the entire process, a specific weld energy can be calculated, which accounts to 147 $^{J}/_{mm^2}$ in experiment R2-13.

A plateau at 4 s is also observed, at which the spindle was stationary until the forge force was initiated. In this case and in general, a deceleration delay should be recommended to surpass a possible plateau inflicted by the response time of the machine controls.

3.3.1.2 Weld characterization

Although the welding process seemed to be unstable, successful welding with the typical flash formation was observed in some experiments. A cross section of experiment R1-13 is shown in figure 3.28, where a defect-free microstructure is observed. The aligned grains of the base metal are gradually re-aligned towards the outside, and typical RFW zones can be distinguished easily as indicated. A hardness line across the weld, as depicted in figure 3.29 revealed that no notable increase or decrease of Vickers hardness 10 was observed. The values were in a range of 200–220 HV10, which equals the value of the Mo base metal. The ultrasonic tests (UT) of the experiments in figure 3.30 show a circumferential lack of fusion in R1-13 and a substantial lack of fusion on one quadrant of the weld R2-13. After the experiment, an axial misalignment and a slight deviation in concentricity was detected, which may have caused the asymmetric bonding quality. Further, the clamping system of the stationary tube in the welding machine is facilitated by two half-shells and showed some wear due to the high strain by temperature and

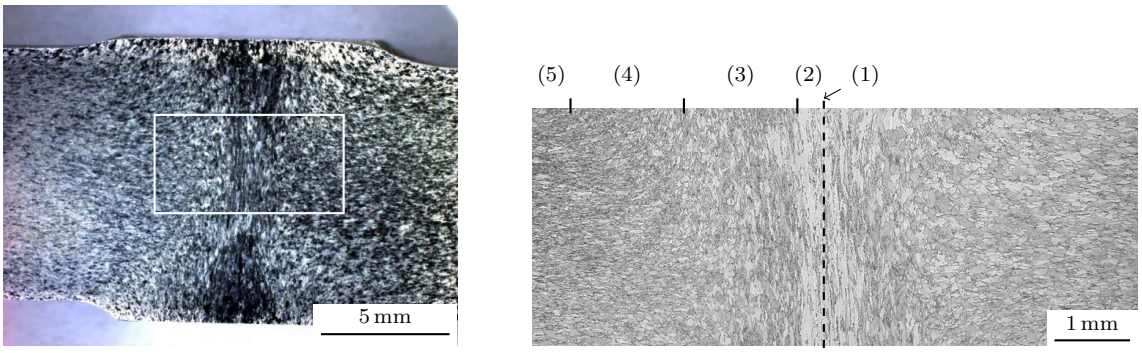

(a) (b)

Figure 3.28: Metallography pictures of experiment R1-13: (a) stereo microscopy and (b) detailed light optical microscopy with RFW zones indicated: (1) contact one, (2) fully plasticized zone, (3) partly deformed zone, (4) undeformed zone, and (5) base metal.

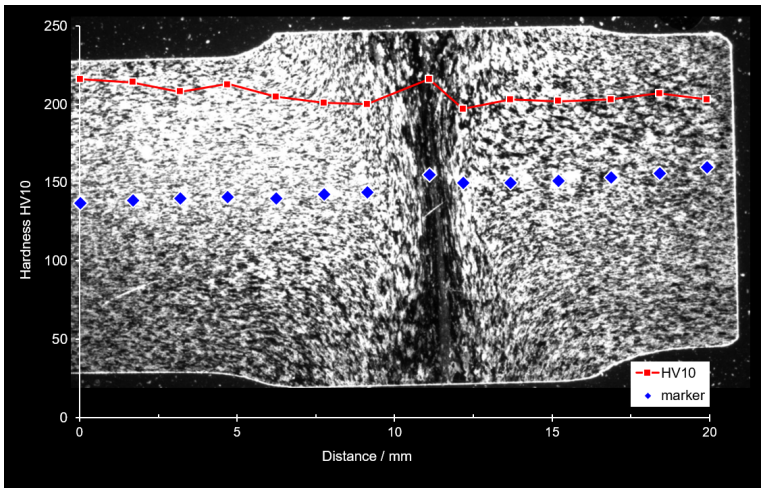

Figure 3.29: Vickers hardness HV10 of experiment R1-13 over the weld area: A constant hardness of approximately 200–220 HV10 is observed.

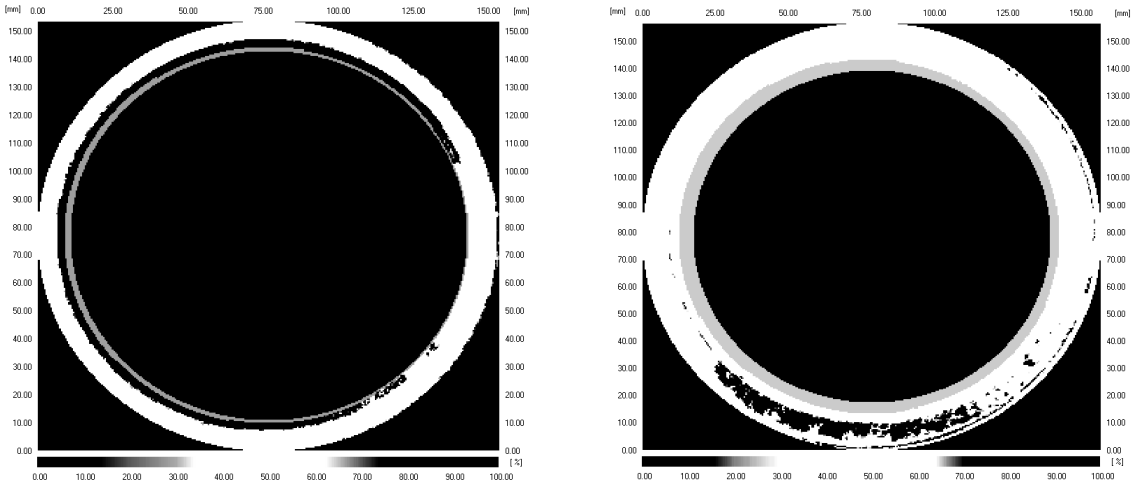

(a) (b)

Figure 3.30: Ultrasonic test result of experiments: (a) Lack of fusion is detected in R1-13 on the inside of the tube and (b) in R2-13 an asymmetric lack of fusion is detected in one quadrant (black areas).

force during the many experiments. It is assumed that by an improved clamping system these defects can be fully avoided.

3.3.1.3 Summary

The experiments in tube format quickly revealed that the behavior of molybdenum in RFW differs considerably from the behavior of conventional materials like steels. Extensive plasticization and a steep upset rate consumed a large amount of drive power and subsequently lead to a spindle stall. This effect could neither be avoided by an input parameter variation, nor a pre-heating of the weld parts. It is concluded that the upsetting behavior and the power consumption of the plastic deformation is an inherent property of the material and the thermal boundary conditions and can only be influenced to some extent by other process parameters.

Further, from the observations it was obvious that a parameter study in this configuration was impossible. The results of the microstructure investigations however, suggested that regardless of the unstable process, a joining of Mo tubes by direct drive RFW is possible and has been partly achieved.

3.3.2 Rod format friction welding

3.3.2.1 Process optimization

The adapted *MTS I-STIR BR4* FSW machine was tested for its RFW capabilities using ∅9 mm low carbon steel samples [105, 107]. The steel samples were welded successfully and variations of welding speed, friction time, friction pressure, and forge pressure, showed a large feasible parameter window. The first experiments in ∅9 mm molybdenum rods with similar welding parameters failed due to several reasons. Occurring problems were sudden brittle material failure at the friction force initiation, sudden unstable material displacement during friction or at forge force initiation, and buckling of the rods in the forge phase, among others. In figure 3.31, some of the issues are depicted. A series of process adaptations and improvements were necessary to enable a successful and stable RFW process of molybdenum:

1. Increase of the rod diameter for Mo from 9 to 12 mm; that is from 63.6 mm^2 to 113.1 mm^2 in cross section.

2. Pre-heating of the weld parts prior to the actual RFW process by rubbing at low levels of pressure (< 10 MPa) to confidently exceed the ductile to brittle transition temperature. It was shown that a quasi-stationary temperature field established at low friction pressures, and that the pressure values corresponded well to the resulting temperature level, as observed in figure 3.32 [105, 107].

3. Gradual transition from friction pressure to forge pressure, using a pressure gradient of 66 $^{MPa}/_{s}$ for Mo and 118 $^{MPa}/_{s}$ for TZM.

4. A deceleration delay was implied that the spindle began to decelerate in the same instant like the axial pressure started to increase to forge pressure.

Figure 3.33 shows the initial pressure course for low carbon steel and the adapted courses for molybdenum and TZM. Further, it is observed that the effective friction time was reduced from 2 s to 0.8 s until the spindle is decelerated and the axial pressure starts to increase to the forge pressure level. The forge pressure of Mo had to be reduced, while the friction pressure of TZM was increased.

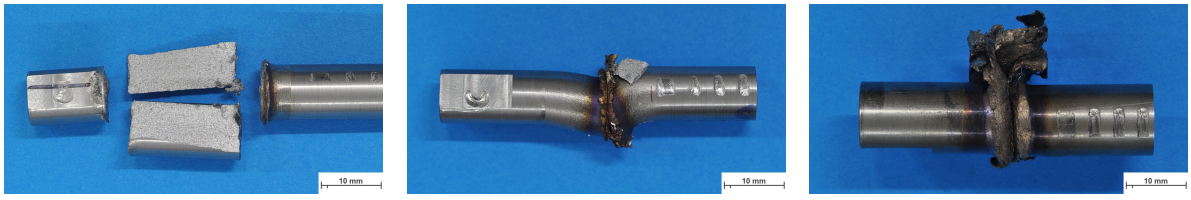

(a) (b) (c)

Figure 3.31: Examples for occurred problems in preliminary Mo experiments: (a) brittle rupture, (b) buckling, and (c) unstable plasticization with asymmetric flash formation

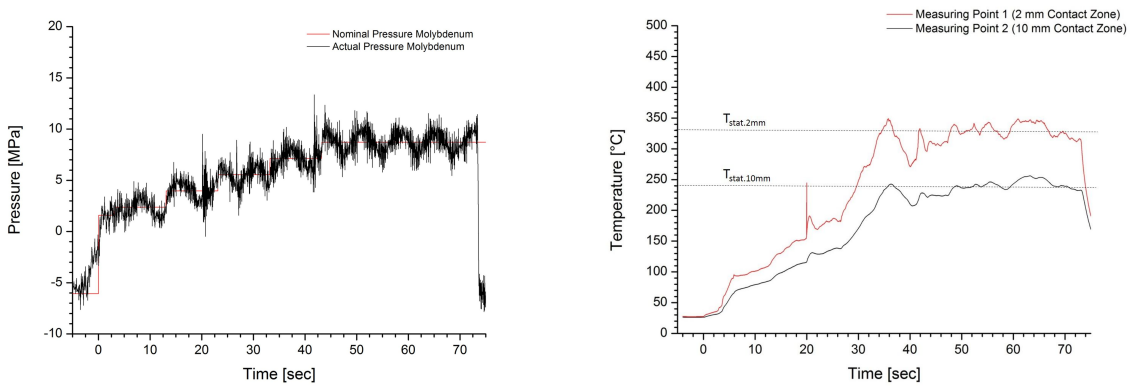

(a) (b)

Figure 3.32: In-situ pre-heating experiments in pure Mo: (a) levels of axial pressure (nominal and acutal) and (b) resulting pre-heating temperatures [105, 107]

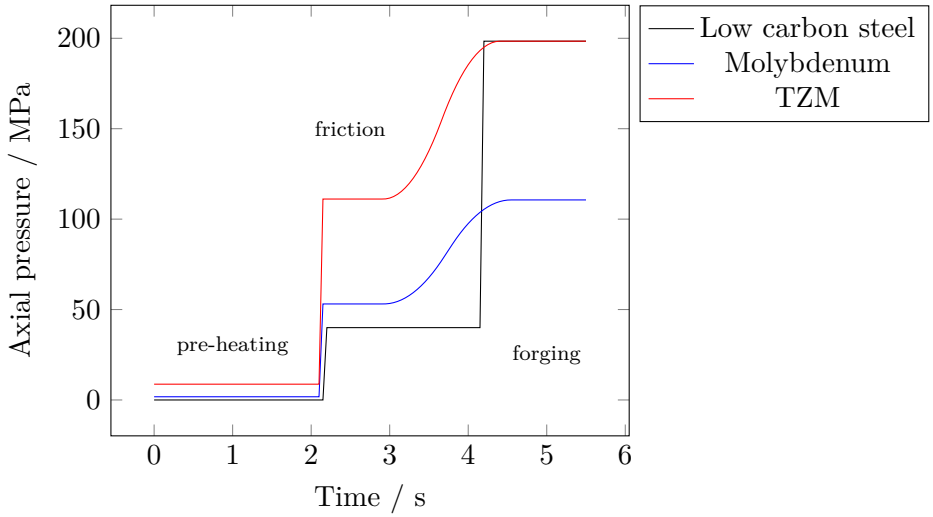

Figure 3.33: Comparison of axial pressure courses of low carbon steel to the adapted processes for Mo and TZM

3.3.2.2 Mo

Figure 3.34 shows three molybdenum experiments in comparison. Three different friction speeds of 2,500, 2,600, and 2,750 min^{-1} (figure 3.34a) were applied to vary the energy input. The course of the axial pressure (figure 3.34b) was kept constant at 53 MPa. The pre-heating phase lasted until 2.2 s, then the axial force was increased to friction force. After another 0.8 s the transition into forging started with a constant deceleration of the spindle of 4,000 $\mathrm{min}^{-1}\,\mathrm{s}^{-1}(\dot{\omega} = 419\,\mathrm{s}^{-2})$, as observed in figure 3.34a. Accordingly, the resulting deceleration times for the three speeds was slightly different and accounted to 0.625, 0.650, and 0.688 s, respectively. As it was shown in preliminary experiments, the point in time of spindle deceleration start had to coincide with the start of pressure increase to enable a continuous process, a deceleration delay $\Delta t_d = 0.65\,\mathrm{s}$ was implied. This means that the deceleration commences 0.65 s after the axial pressure starts to increase, as explained in section 3.1.4.

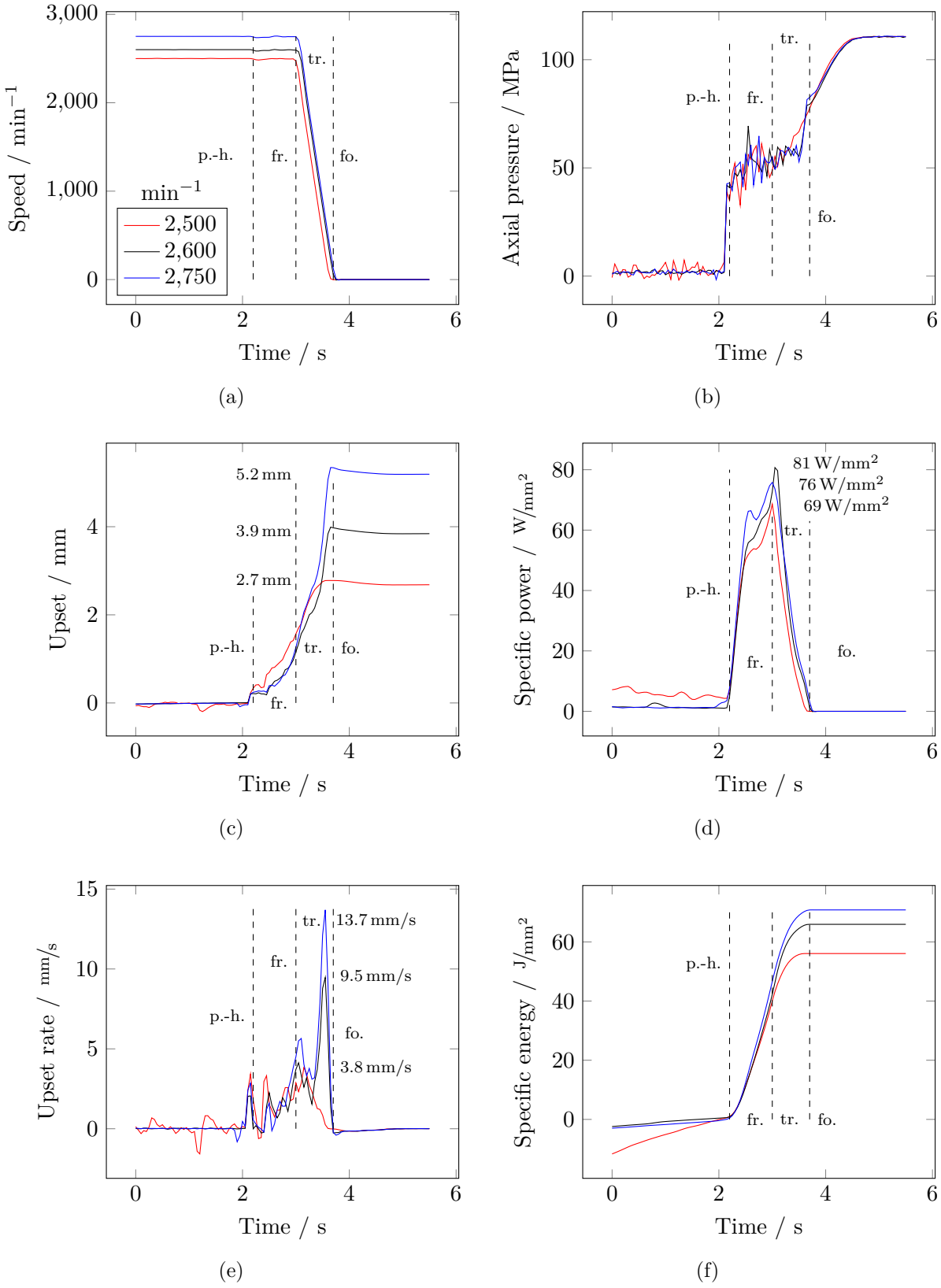

Figure 3.34: Comparison of welding parameters of three rod format experiments of Mo: (a) speed, (b) axial pressure, (c) resulting upset, (d) specific weld power, (e) upset rate, and (f) specific weld energy. The phases pre-heating (p.-h.), friction (fr.), transition (tr.), and forging (fo.) are indicated by dashed lines.

The comparison of the upsetting behavior (figure 3.34c) shows that the main difference in occurred in the last instances before the spindle stop. In the friction phase and the first half of the transition phase (labeled "tr." throughout figure 3.34) the upsetting of the three experiments is similar. Only in the last 0.5 s the upset courses differ significantly which resulted in three different final upsets of 2.7, 3.9, and 5.2 mm. In literature of RFW [80, 87], part of the upsetting takes place in the forge phase. In the present experiments the entire upsetting takes place in the relatively short friction and transition phases of 0.8 and 0.7 s, respectively.

In figure 3.34f it is observed that the transition phase bears the difference in total energy input which is responsible for the different total upsets. Note that the ordinate was zeroed at the start of the friction phase as the pre-heating input energy was neglected for the comparison. The pre-heating energy varied largely but eventually showed an equilibrium during the process of pre-heating with a stationary temperature field throughout the weld parts. The courses of specific weld power are observed in figure 3.34d, were at higher speed an accordingly higher power value is observed. The power courses cumulated in a power peak at the instant of spindle stop, but as the magnitude of the peaks did not correspond to their respective order of speed, it is concluded that the momentarily absolute power peaks were only of subordinate importance.

It is further observed that in the friction phase the upset rates of the experiments (figure 3.34e) are in the magnitude of 3–4 $^{mm}/_{s}$. A notable difference occurred only in the transition phase, shortly before the spindle stop, at about 75% of the final forge force: 9.5 $^{mm}/_{s}$ at 2,600 min^{-1} and 13.7 $^{mm}/_{s}$ at 2,750 min^{-1}, while experiment 2,500 min^{-1} showed no notable upset rate peak at all. The courses of specific weld power (figure 3.34d) show low current power values below 10 $^{W}/_{mm^2}$ at that point in time. Therefore, the terminal upset rates were a response to the increasing axial force and displacement of plasticized material rather than the plasticization by energy input.

More experiments with variable process parameters weld speed, spindle deceleration, axial pressure, and axial pressure gradient were conducted. In figure 3.35a the resulting upsets as a result of the specific energy input values are shown. If the specific welding energy is divided by the resulting upset, the energy per displaced volume in $^{J}/_{mm^3}$ is calculated. Figure 3.35b depicts this value in relation to the respective upsets.

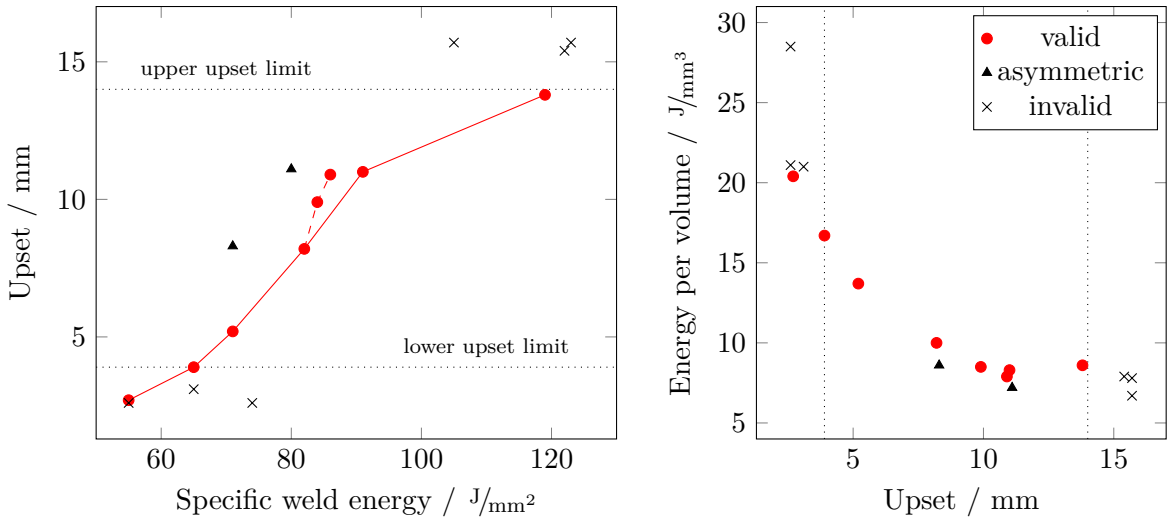

Figure 3.35: Display of all Mo trial welds, (a) resulting upset as response to specific weld energy and (b) energy per displaced volume according to the final upset

First, using the criterion of resulting upset, welding quality thresholds can be defined: In the lower upset domain, improper bonding was observed in most cases; one exception was the experiment at 2,500 min^{-1} of the discussion before. It is assumed that too little upset does not allow the weld interfaces to be cleaned properly by an expulsion of surface contaminations into the flash. From an upset of 3.9 mm onwards a sufficient flash formation is observed. At upsets of 14 mm and more, the machine's axial travel capability was on the limit and further, the high total upsets are generated by excessively high upset rates of up to 37 $^{\mathrm{mm}}/_{\mathrm{s}}$ which lead to unstable plastic deformation.

Triangular marks in the figures represent two experiments where small axial misalignments of the two weld parts or process instabilities lead to an asymmetric formation of the flash, but completed successfully.

Second, the influences of process parameter changes can be discussed. In most displayed experiments, the forge condition (forge pressure gradient, deceleration) was kept constant and the only variation was the welding speed from 2,500 to 2,900 min^{-1}. These experiments are indicated in figure 3.35a by the filled red markers connected by a line and a near-linear relation between specific weld energy and upset is observed. If, however, the force gradient is increased from 66 to 71 and 75 $^{\mathrm{MPa}}/_{\mathrm{s}}$ the upset increases more steeply at almost constant specific weld energy (82, 84, and 86 $^{\mathrm{J}}/_{\mathrm{mm}^2}$), as indicated by the dashed red line in the diagram.

A combination of slow deceleration and soft pressure gradient (2,000 $\mathrm{min}^{-1}\,\mathrm{s}^{-1}$ and 35 $^{\mathrm{MPa}}/_{\mathrm{s}}$) lead to an invalid result. Due to the prolonged process time, the plasticization was unstable yet excessive, resulting in 15.7 mm at 105 $^{\mathrm{J}}/_{\mathrm{mm}^2}$. Another combination of a soft pressure gradient but a regular axial pressure increase (3,500 $\mathrm{min}^{-1}\,\mathrm{s}^{-1}$ and 66 $^{\mathrm{MPa}}/_{\mathrm{s}}$) resulted in too little upset of 2.6 mm and an energy input of 76 $^{\mathrm{J}}/_{\mathrm{mm}^2}$. Both experiments showed improper bonding. To conclude, a slower deceleration lead to instabilities in the axial deformation and the process was therefore not feasible.

Overall in figure 3.35b it is observed that in successful welds, the energy per displaced volume values ranged from 8 to roughly 20 $^{\mathrm{J}}/_{\mathrm{mm}^3}$. A discrete tendency of less energy for displacement required at higher total upsets is observed. This indicates that a certain amount of energy is required to first plasticize the material, while at higher upsets the required energy per volume for deformation is less. The final upset is then mostly determined by the design of the transition phase.

To sum up, a short interval of high upset rate at the end of the transition phase or start of the forge phase, respectively, is required to facilitate proper bonding. Furthermore, molybdenum yielded only a small process window with a fixed deceleration of 4,000 $\mathrm{min}^{-1}\,\mathrm{s}^{-1}$ and allowed only a small variation of the pressure gradient between 66 and 75 $^{\mathrm{MPa}}/_{\mathrm{s}}$. The main parameter to change the resulting upset proved to be the welding speed, which was accompanied by a change of the resulting specific weld energy. If then the specific weld energy is adduced as an input parameter, the exact forge condition, consisting of spindle deceleration $\dot{n}$, pressure gradient $\dot{p}$, and deceleration delay Δt_d, has to be determined and kept constant.

3.3.2.3 TZM

Analogously to Mo, the process parameters welding speed, axial pressure, upset, specific weld power, upset rate, and specific weld energy of three different experiments of TZM are depicted in figure 3.36. Again, the welding speed was varied between 2,500, 2,600, and 2,750 min^{-1} while the deceleration (figure 3.36a) and the course of axial pressure (figure 3.36b) was kept constant. Compared to Mo, the level of friction pressure and forge pressure, however, had to be raised from 53 to 111 MPa and from 110 to 198 MPa, respectively. This is due to the better high temperature strength of TZM compared to Mo.

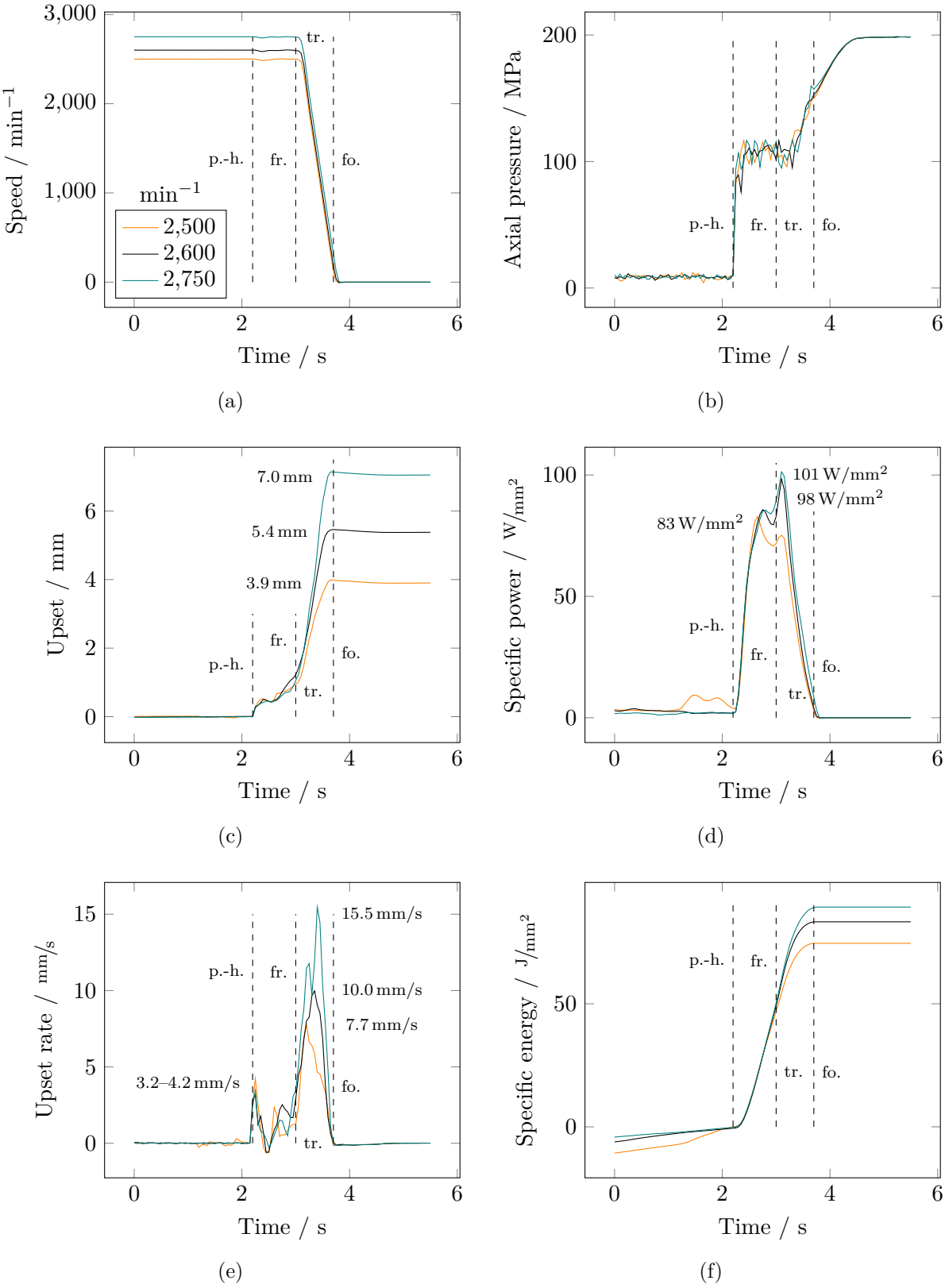

Figure 3.36: Comparison of welding parameters of three rod format experiments of TZM: (a) speed, (b) axial pressure, (c) resulting upset, (d) specific weld power, (e) upset rate, and (f) specific weld energy. The phases pre-heating (p.-h.), friction (fr.), transition (tr.), and forging (fo.) are indicated by dashed lines.

The upset courses of the three experiments (figure 3.36c) were almost identical to one another in the friction phase, while in the last 0.5 s of the transition phase the final differences in upset were produced. The manifested upset rates in the transition zone of 7.7, 10.0, and 15.5 $^{mm}/_{s}$ (figure 3.36e) resulted in the final upset values of 3.9, 5.4, and 7.0 mm for the three experiments. Again, the entire upset occurred in the friction and transition phases.

All three specific weld power courses in figure 3.36d showed two distinct peaks, one in the friction phase and another in the transition phase, momentarily after the spindle started to decelerate. The first peak was due to the commencing upsetting and the second occurred at the sudden steep increase of the upset rate. It is apparent that the instant of the transition power peak caused differences in the rise of the upset rates that eventually cumulated in the final upsets.

Table 3.2: Process parameter variations in TZM trial welds

Parameter	low	middle	high
Speed $n/\,\mathrm{min}^{-1}$	2,500	2,600	2,750
Friction pressure $p_f/\,\mathrm{MPa}$	111	–	125
Pressure gradient $\dot{p}/\,^{\mathrm{MPa}}/_{\mathrm{s}}$	118	–	786
Deceleration $\dot{n}/\,\mathrm{min}^{-1}\,\mathrm{s}^{-1}$	2,500	3,000	4,000

Figure 3.37a shows the resulting upsets of various input parameter changes. First of all it is noted that TZM allows a wider variation of forge pressure gradient and deceleration than Mo. The respective parameter values are listed in table 3.2. The experiments with 110 MPa depict the three experiments displayed in figure 3.36. An almost linear response of upset to a variation in specific welding energy is observed between the three. An increase of friction pressure to 125 MPa lifted the resulting upsets to higher values at similar specific welding energies, but also showed a near-linear behavior. The experiment with 109 $^{J}/_{mm^2}$ and 7.9 mm upset does not fit into this behavior, it was assumed that experimental irregularities (i.e. a not sufficiently warmed

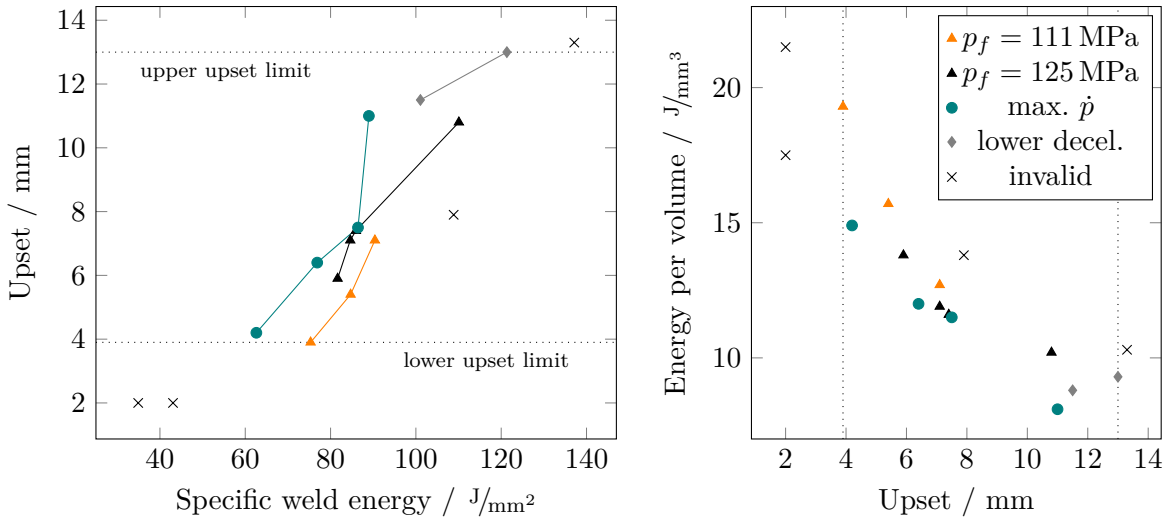

(a) (b)

Figure 3.37: Display of all TZM trial welds: (a) resulting upset as response to specific weld energy and (b) energy per displaced volume according to final upset

up machine) caused the deviation from the other experiments of that series and was therefore discarded. As discussed previously, due to the cleaning effect of the weld interface by forming flash a lower upset thresholds was identified at 3.9 mm. On the upper limit, at upsets beyond 13 mm the welding process became unstable.

TZM further allowed an increase of the regular pressure gradient from 118 $^{MPa}/_{s}$ to the maximum machine capability of approximately 786 $^{MPa}/_{s}$ (resulting from the machine specification's quoted 50 $^{kN}/_{s}$) to produce successful welds. In this case at similar upsets the specific weld energies were lower by a margin of 10–20%. This is explained by the fact that a steeper increase of axial pressure causes more material to displace in the transition phase due to higher pressure values while the input energies are less affected by the axial pressure.

A reduction of the deceleration from 4,000 to 3,000 and 2,500 $\mathrm{min^{-1}\,s^{-1}}$ resulted in a longer process time which increased the total and therefore the specific energy input. As a consequence, the resulting upset was increased simultaneously the process became less stable.

The calculated energy per displaced volume varies from 8 to 20 $^{J}/_{mm^3}$ which are comparable values to the Mo experiments. Again, a distinct drop in required energy per displaced volume with higher final upset is observed in figure 3.37b. As a more comprehensive welding parameter variation was possible in TZM, the values scatter more than in Mo. Therefore, the energy per displaced volume depends more on the forge condition than it is a measure for the resulting upset.

In table 3.3 the responses of upset, specific weld energy, and process stability to the various process parameter changes are compiled.

Table 3.3: Responses of TZM rod material to process parameter variations: Increase (↑), decrease (↓), and no effect (○)

Variation	upset	weld energy	process stability
Reduced friction pressure	↓	↓	○
Increased friction pressure	↑	↑	○
Increased friction pressure gradient	○	↓	↓
Reduced deceleration	↑	↑	↓

To conclude, due to its better high temperature strength compared to Mo, TZM showed a less sensitive behavior during friction welding than Mo and allowed a moderate parameter influence study. The best combination proved to be in the regime of 60–100 $^{J}/_{mm^2}$, with resulting upsets ranging from 4–11 mm. Similarly to Mo, a soft pressure gradient and high deceleration was preferable.

3.3.2.4 Microstructure characterization

The microstructure of both Mo and TZM samples was investigated to evaluate the quality of the joints. In figure 3.38 the results of the three already discussed experiments with identical process parameters but 2,500, 2,600, and 2,750 $\mathrm{min^{-1}}$ weld speed are depicted. First in figures 3.38a, b, and c, a macro photograph is observed. The flash geometry of all three welds was symmetrical and the processes finished successfully. Figures 3.38d, e, and f show the etched cross sections in which the microstructural character of the friction welds is observed. The microstructure exhibited the typical change from base metal to outwardly aligned and refined grains as observed in most friction welds. At 2,500 and 2,600 $\mathrm{min^{-1}}$ improper bonding and lack of fusion was visualized as white areas by the etching. It is observed that at 2,500 $\mathrm{min^{-1}}$ the

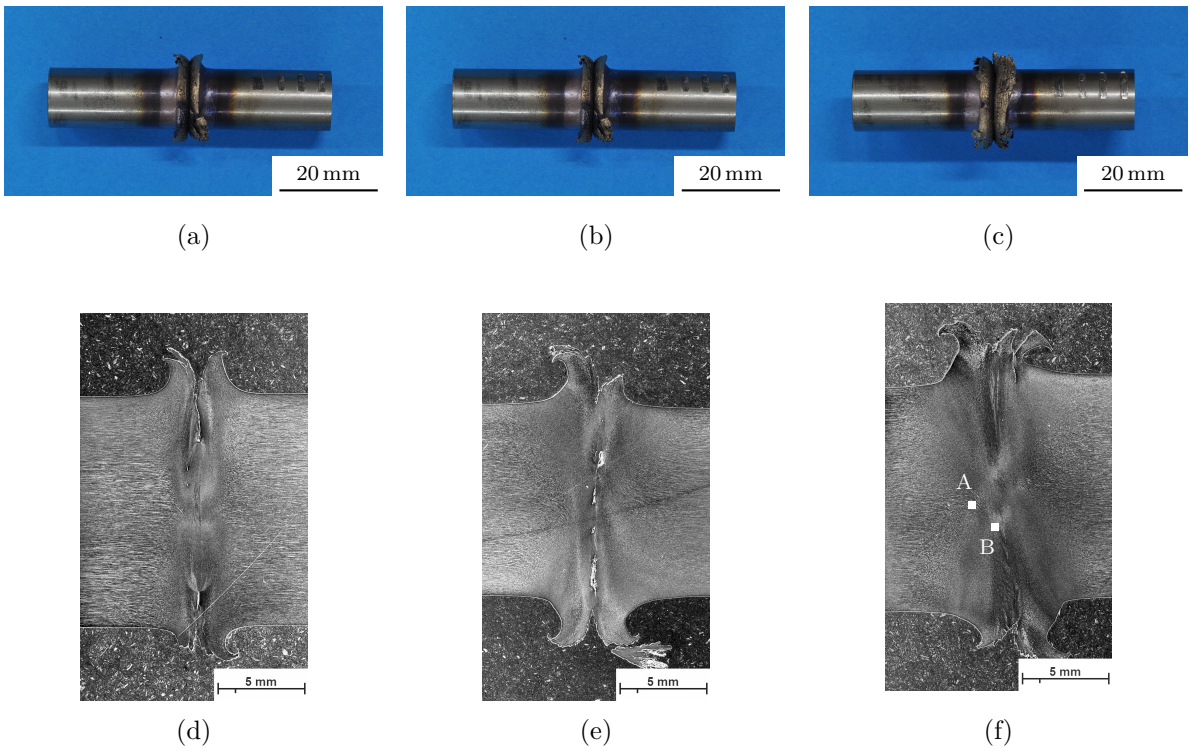

Figure 3.38: Macro photographs, light optical microscopy of etched cross sections of rod format molybdenum RFW experiments: (a), (d) 2,500 min^{-1}, (b), (e) 2,600 min^{-1}, and (c), (f) 2,750 min^{-1}

weld sample exhibited a small lack of fusion, and at 2,600 min^{-1} it showed multiple irregularities at the welding interface. At 2,750 min^{-1}, defect-free bonding was achieved.

The three experiments in TZM at 2,500, 2,600, and 2,750 min^{-1} with otherwise identical process parameters are observed in figure 3.39. The flash formation was symmetrical and regular, compared to Mo, however, it showed a more curly morphology, as observed in figures 3.39d, e, and f. This is once more explained by the better high temperature strength of TZM, as schematically demonstrated in figure 3.41: Assuming a similar temperature distribution, the shear stress limit in Mo is reached at a lower temperature, meaning the material plastically deforms further away from the welding interface. The higher shear stress limit of TZM on the other hand means that the gradient of the transversal material displacement has to be higher and therefore it drives stronger towards a screw movement.

The hardness distribution was investigated with a Vickers hardness HV1 matrix scan. Figure 3.43 shows the results for molybdenum and figure 3.44 the hardness map for TZM. It is observed that the base metal in Mo averaged 245 HV1 and in TZM 291 HV1. In Mo a change of hardness was observed neither in the plasticized zone nor in the contact zone. In TZM a slight increase to 310 HV1 was observed in the plasticized zone and the contact zone.

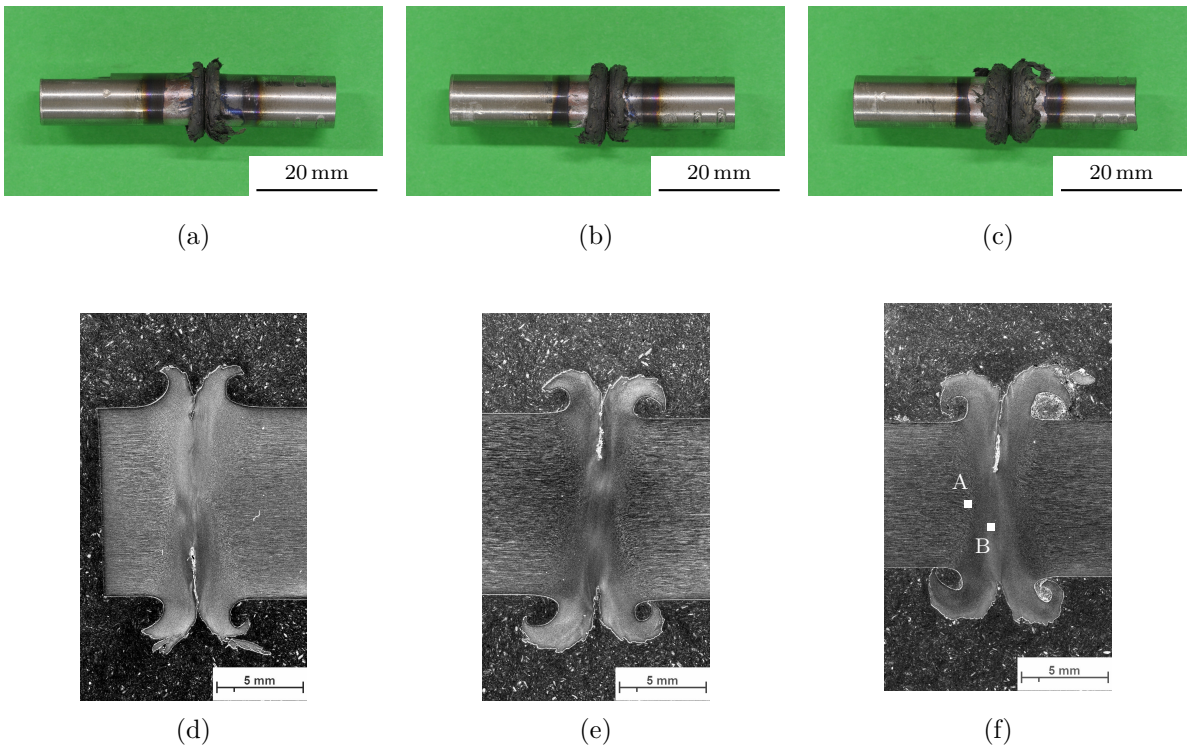

(a) (b) (c)

(d) (e) (f)

Figure 3.39: Macro photograph, light optical microscopy of etched cross section of rod format TZM RFW experiments: (a), (d) 2,500 min^{-1}, (b), (e) 2,600 min^{-1}, and (c), (f) 2,750 min^{-1}

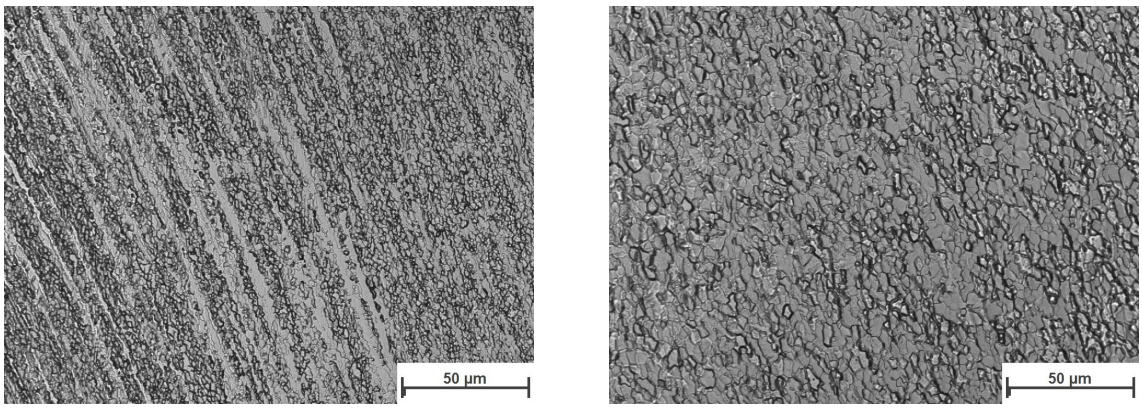

(a) (b)

Figure 3.40: Light optical microscope images of points marked in figure 3.38: (a) Detail A of plasticized zone with diverted grains visible and (b) detail B of the weld center zone with new, undeformed grains

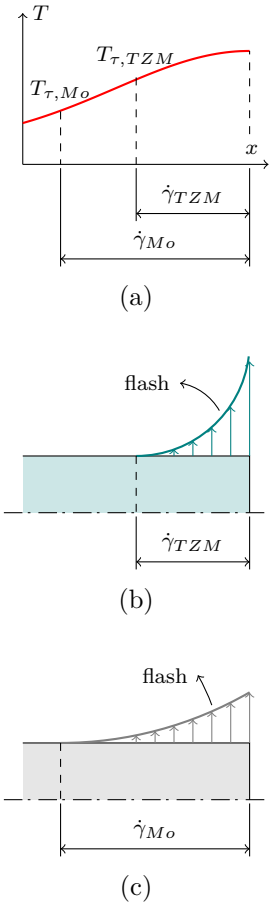

Figure 3.41: Schematic of the effect of the shear stress limit on the flash formation: (a) Given identical temperature distributions, the shear yield limit is higher in TZM than in Mo, which leads to less material plasticizing and (b) a stronger curling effect of the displaced material in TZM than (c) in Mo.

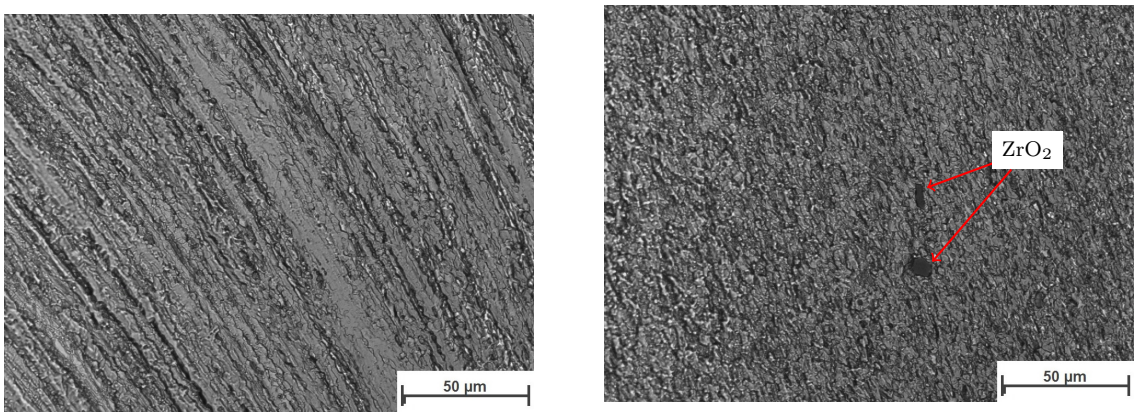

Figure 3.42: Light optical microscope images of points marked in figure 3.39f: (a) Detail A of the plasticized zone with visible diverted grains and (b) detail B of the weld center zone of TZM RFW experiment where a homogeneous microstructure of fine grains is observed. ZrO_2 particles are highlighted.

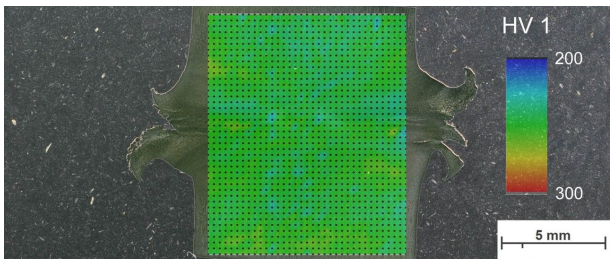

Figure 3.43: Hardness map of a rod format molybdenum RFW experiment at 2,750 min^{-1}

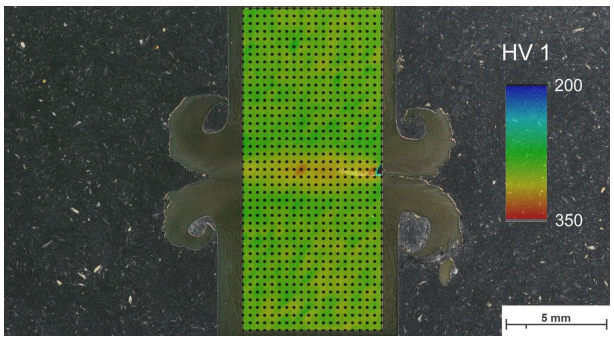

Figure 3.44: Hardness map of a rod format TZM RFW experiment at 2,750 min^{-1}

3.3.3 Simulation of rotary friction welding

Figure 3.45 shows temperature maps of the simulation at different points in time. Figure 3.45a is at 15.0 s, which is still in the pre-heating phase, figure 3.45b shows the point in time with the highest occurring temperature at 16.2 s, during the friction phase. Here, part of the deformation is already visible. In the forging phase at 18.4 s in figure 3.45c, the full upset is reached, the heat is conducted away from the friction interface, and the overall temperature declines. The overlay of the resulting contour of the simulation onto the polished cross section of the experiment reveals a deviation (figure 3.46).

Points 1, 2, and 3 (2, 5, and 10 mm distance from the welding interface, figure 3.23) were measured by S-type thermocouples during the experiment. These points were tracked in the simulation and were compared to the experiment, as shown in figure 3.47. In the pre-heating phase (0–15.5 s) the temperature courses match almost exactly, which means that on the one hand the heat source was set correctly and on the other hand confirms the material data of heat

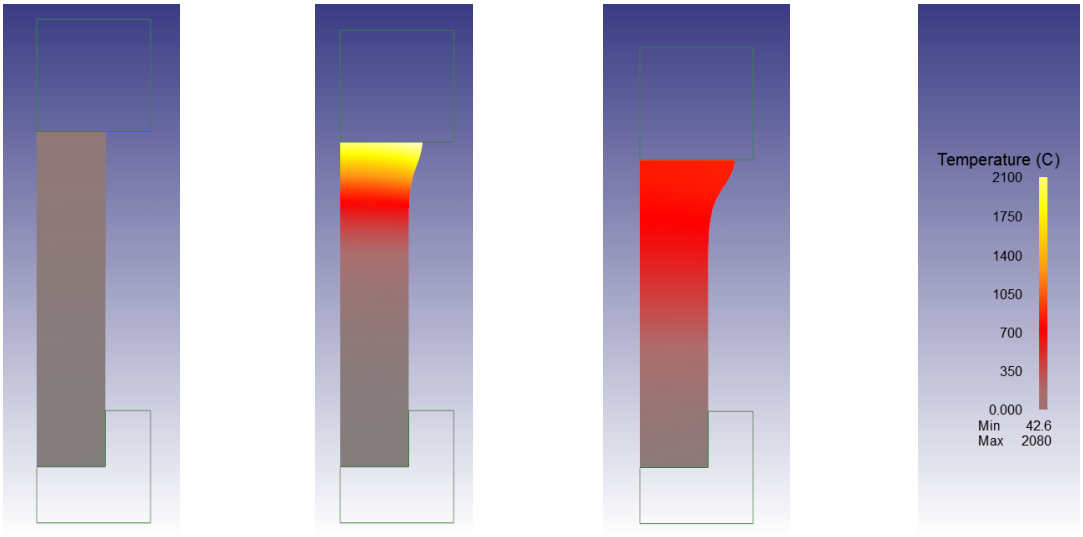

(a) (b) (c) (d)

Figure 3.45: Simulation results of the temperature distribution during RFW of pure Mo at (a) 15.0 s (pre-heating), (b) 16.2 s (friction phase), (c) 18.4 s (forge phase), and (d) the colorbar legend

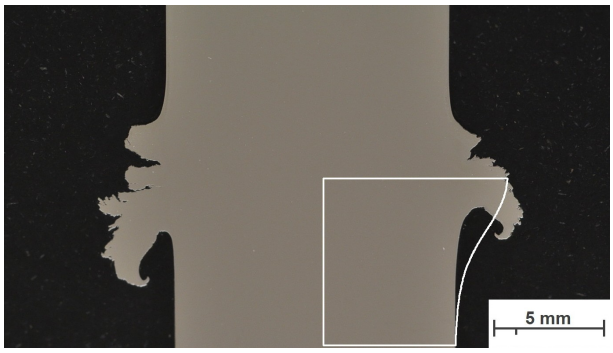

Figure 3.46: Overlay of the resulting contour of the simulation on the polished cross section of the experiment

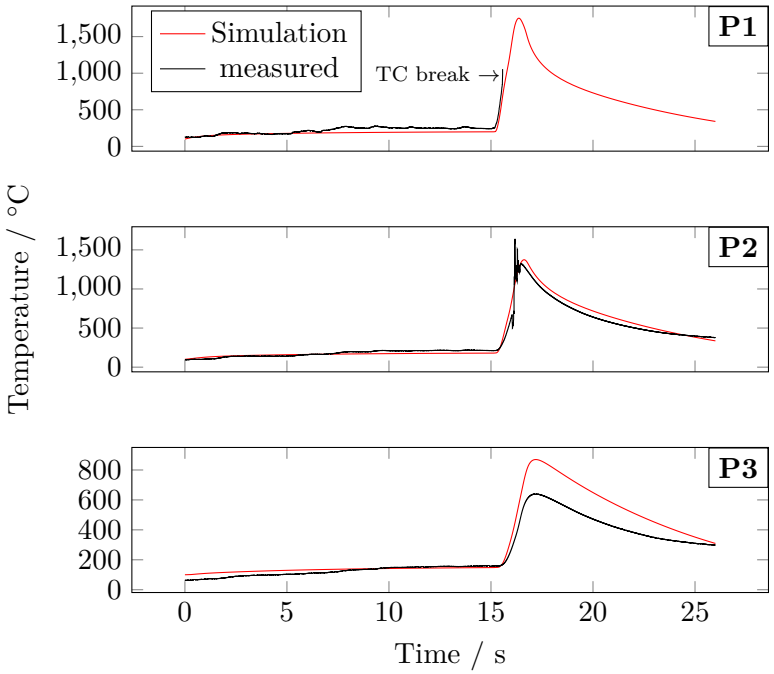

Figure 3.47: Measured temperature courses during the experiment in comparison to the simulated temperatures at the respective points. The thermocouple at point 1 was shifted into the forming flash and broke at approximately 16 s as indicated.

conduction and heat capacity.

Due to the forming flash, the thermocouple at point 1 was sheared off at approximately 16 s. At point 2 the temperatures were well-matched, while the simulation predicted a slightly higher peak temperature at point 3. This indicates a too soft temperature gradient during the friction phase, which could result from a too low heat transfer to ambience or a too small heat conduction coefficient into the clamping system. The temperature dependent values of thermal conductivity and specific heat capacity are well established and unlikely to be the cause of the observed temperature deviation.

Figure 3.48 shows the temperature course over time at point 1 of the simulation if the heat input is varied. Here the experimentally obtained input power P is increased by 10% and decreased by 10%, respectively. It is observed that the peak temperatures drop by 8.2% or rise by 8.4% in absolute values. The gradients of the temperatures after the friction phase (17–26 s) appear similar, which again suggests that the spatial temperature gradient is more dependent on the heat transfer boundary conditions.

Because the axial stroke (upset) was a boundary condition in the simulation, the axial force was a result to assess. Figure 3.49 shows the course of the measured axial force of the experiment in comparison to the resulting axial force of the simulation. Large differences are observed in a number of ways: First, a force between 6 and 8 kN occurs during the pre-heating phase. This results from the difference between ideal and real pre-heating condition. A slight upsetting occurred during the experiment in the pre-heating phase, which is due to macroscopic shearing and flattening of the rubbing surfaces. These effects are not modeled in the simulation, therefore the response of the simulation to an axial upset is compression stress and thus axial force on the rotary part.

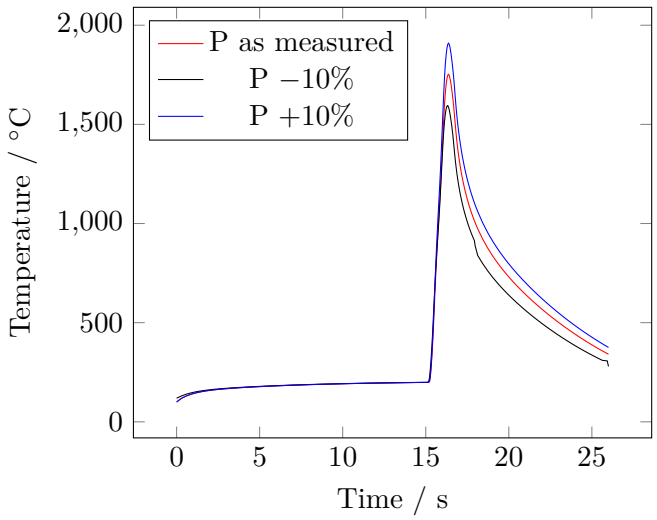

Figure 3.48: Comparison of peak temperatures at point 1 of the heat input as measured, increased by 10%, and reduced by 10%

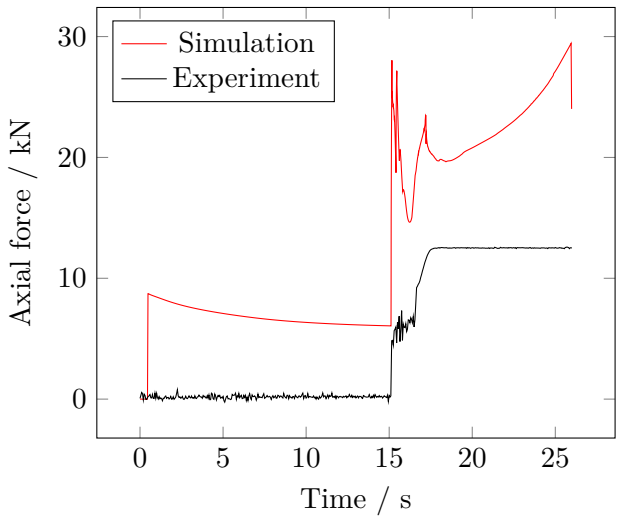

Figure 3.49: Measured axial force during the experiment in comparison to the resulting axial force of the simulation. The axial force of the simulation is a factor of two higher than the measured axial force.

3.3.3.1 Input parameter force

If instead of the axial travel the force was set as an input parameter and the axial travel of the top die (upset) was the result, a large difference was observed also. As figure 3.50 shows, the workpiece almost remained undeformed with a total upset of 0.034 mm. The temperature evolution was comparable to the axial travel input condition because it is almost independent from the deformation. It is therefore stated that the simulation in the current setup lacks the desired ability to consistently represent the RFW process of pure Mo.

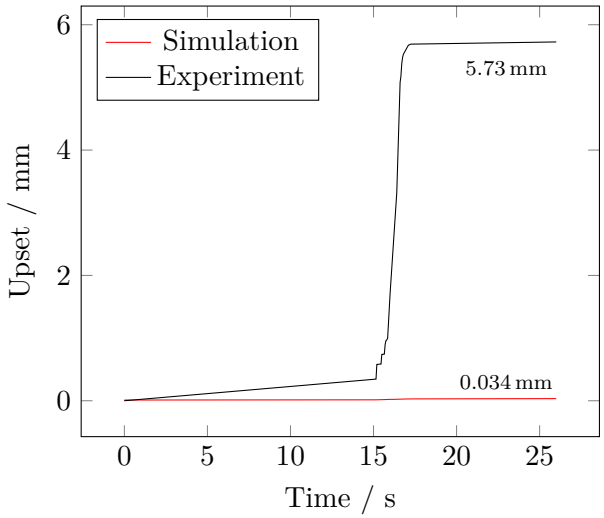

Figure 3.50: Comparison of upset between the inputs axial travel and axial force

3.3.4 Conclusion

3.3.4.1 Scaling of a continuous friction welding process

Contrary to Duffin and Bahrani in mild steel [87], a change of upset rate depending on speed or axial pressure was not observed in RFW of Mo and TZM. It is suggested that the equilibrium upset rate depended more on the material properties rather than the welding parameters. Contributing factors were thermal diffusivity, the softening or hardening behavior due to temperature, deformation, deformation rate, the thermal boundary conditions that govern heat conduction and convection, and finally the weld part format. It is obvious if Mo and TZM allowed for a larger process window, possibly the equilibrium upset rate could be influenced by axial pressure and welding speed to some extent. Nevertheless, it is certain that a lack of drive power cannot be countervailed by a prolonged friction phase to balance the energy input. This value is only a valid measure for estimating the resulting upset, if the forge condition is kept constant.

Controlling the RFW process by upset rather than axial pressure is possible but rarely in use [71]. The main issue is the controllability; the material reacts to an imprinted axial upset with axial pressure and torque peaks which quickly can exceed the machine capabilities. In the case of the laboratory scale experiments, the maximum read frequency was 20 Hz which means that the machine would have to control upsets of up to 0.75 mm per loop. The resulting fluctuations in axial pressure would not be controllable in this configuration.

The specific welding energies varied between 147 $^{J}/_{mm^2}$ at tube format and 70.8 $^{J}/_{mm^2}$ at rod format. Further, the consumed energy per displaced volume was 5.7 $^{J}/_{mm^3}$, which is clearly below the observed lowest values in rod format of 8 $^{J}/_{mm^3}$. On the one hand this circumstance may be attributed to the fact that the tube format experiments were conducted in tubular formats and the rod format experiments were full cross sectioned rods. On the other hand, the tube format experiments always were accompanied by a premature spindle deceleration which distorts the comparability of the results of the two processes.

Nevertheless, using the experience of the experiments in rod format, a series of process improvements for the larger tube format process can be derived:

1. The maximum drive power of the *HR 1250* machine was 150 kW; with a welding cross

section of 4,400 mm^2 the maximum achievable specific power calculates to 34 $^{W}/_{mm^2}$, which is only 42% of the achieved maximum specific power value in the friction phase of the rod format Mo experiments. Following this line of argument, the required drive power for a successful tube format friction welding experiment is 357 kW.

2. Assuming a required specific weld energy of 70.8 $^{J}/_{mm^2}$, the maximum weldable cross section in the *HR 1250* machine calculates to 2,119 mm^2.

3. With sufficient drive power, a re-raise of the friction pressure to 53 MPa should be possible.

4. Given a higher friction pressure, the friction phase can be shortened to a suitable timespan.

5. As elaborated in preliminary rod format experiments, a deceleration delay ("forging into the turning spindle") must be employed that the the transition phase coincides with the increase of the axial pressure.

6. The pressure gradient must be lowered to sustain a stable axial deformation and to prevent a sudden plastic yielding of the welding partners.

7. A forging pressure of 110 MPa proved to be sufficient for the rod format experiments, therefore the final pressure of the tube format setup can be lowered also.

8. Finally, a pre-heating phase at low axial pressure can be employed directly before the friction phase, if the welding setup proves to be unstable with no pre-heating.

Figure 3.51 shows the proposed process improvements schematically in comparison to the existing tube format process.

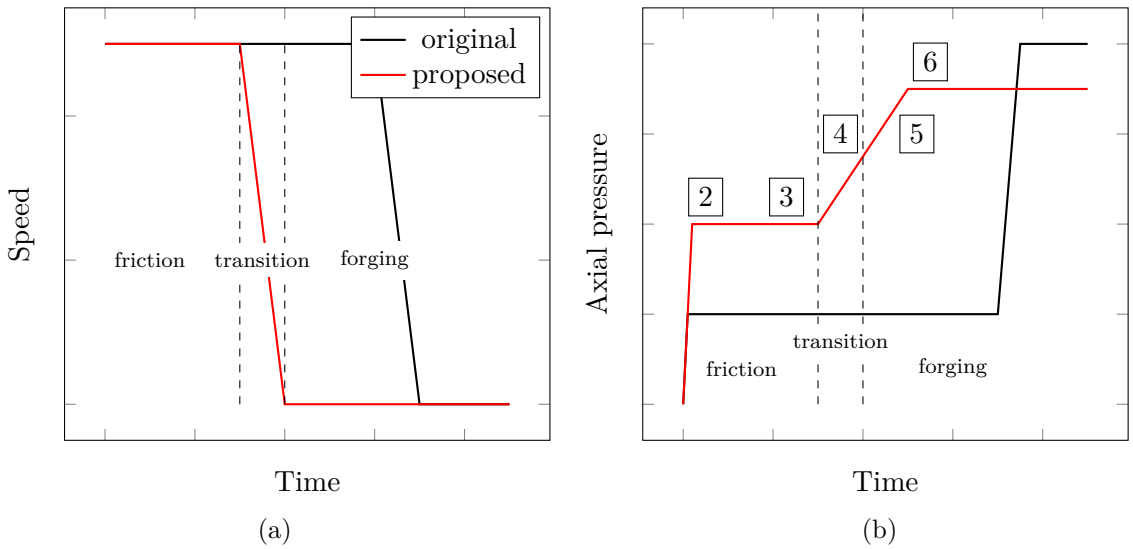

Figure 3.51: Schematic courses of (a) speed and (b) axial pressure of the tube format experiment and suggested process improvements. The numbers 2–6 refer to the items of the list in the conclusion.

3.3.4.2 Deformation and deformation rates

As discussed earlier, determining the rotational shear rates is difficult. After the weld parts are heated up and the shear yield strength drop below the present shearing forces, plastic deformation commences. Further, sticking condition is assumed at the start of upsetting. Referring to figure 3.34c, upsetting and therefore plastic deformation starts roughly 0.3 s into the friction phase. The remaining timespan for plastic deformation under sticking condition is $t_{fr} = 0.5\,\mathrm{s}$ in the friction phase and $t_{tr} = 0.6\,\mathrm{s}$ in the transition phase. The total rotary plastic deformation is

$$\varphi_n = t_{fr} \cdot n + t_{tr} \cdot \frac{n}{2} \tag{3.22}$$

revolutions. For Mo that accounts to $0.5 \cdot 2{,}750/60 + 0.6 \cdot 2{,}750/2/60 \approx 37$ revolutions. TZM starts to plasticize an instant of 0.1 s later, therefore TZM completed only 32 revolutions in full sticking condition.

Figure 3.52 shows the estimation of the deformed zone of the Mo weld at $2{,}750\,\mathrm{min}^{-1}$ and the schematic sketch for the calculation of the shear and axial strain rates. The span of the deformed zone was approximately 3 mm in width. Using equation 3.21 (page 41), an approximate maximum shear rate of $\dot{\gamma}_{max} = 864\,\mathrm{s}^{-1}$ can be calculated for a diameter of 12 mm. As TZM only showed about 2.5 mm of deformed zone but the diameter of the rods was only 9 mm, the calculated shear rate on the perimeter is similar, being $\dot{\gamma}_{max} = 778\,\mathrm{s}^{-1}$.

The last interval of spindle rotation contains the maximum axial upset rates. If again a deforming length of 3 mm in Mo is assumed, the axial strain rate equals $\dot{\varepsilon} = 4.6\,\mathrm{s}^{-1}$. Given the obtained values for maximum upset rate and an approximate deformation length of 2.5 mm, the achieved axial strain rates in TZM were 3.1, 4, and $6.2\,\mathrm{s}^{-1}$.

To conclude, the material deformation consists of a phase of relatively high shear deformation of several hundred s^{-1} with low axial strain. Subsequently, when the relative motion between the two welding parts is almost zero and neglectable, an axial compression with medium strain rates of 1–10 s^{-1} completes the process.

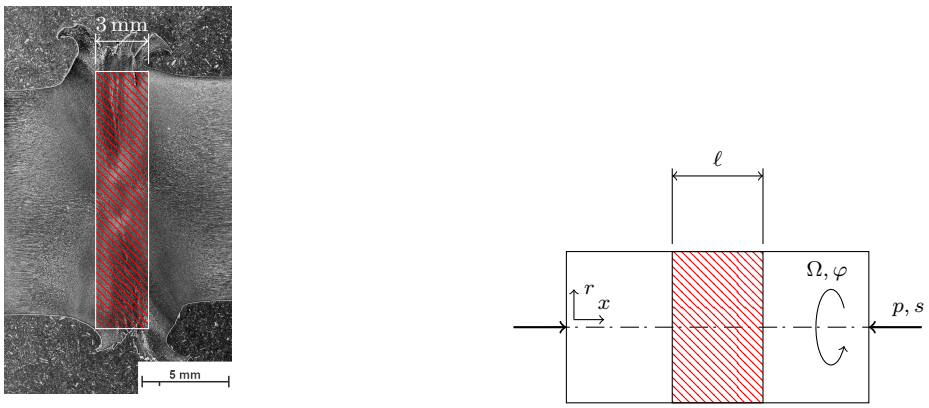

(a) (b)

Figure 3.52: (a) 12 mm Mo rods welded with $2{,}750\,\mathrm{min}^{-1}$ with the deforming zone indicated and (b) the schematic sketch of the deforming volume

3.3.4.3 Simulation

As mentioned before, the temperature gradient in axial z-direction appears to be too small. A higher peak temperature at the interface combined with a higher temperature gradient would lead to more softening and thus more deformation which would influence the flash morphology. However, the simulations have shown that the main change of contour was negligible, even at twice the input power. This indicates on the one hand that the resistance of the material model against deformation is too high. On the other hand, the the rotary shear deformation could play a role in the flash formation as well, but was neglected in the 2.5d simplification. Pure axial compression was the basis for both the modeled deformation as well as the material data which was used from flow curves resulting from compression tests.

Another uncertainty was that RFW of pure Mo was only partly stable in the experiments. This means that with a slight change of the welding parameters, the results sometimes differed largely. In similar experiments a conical deformation was observed, more resembling the simulation result. Since the utilized FSW machine was limited in the axial alignment of the welding parts, insufficiencies may also have played a role. To sum up, the current state of the simulation enables a rough estimation of the temperature field during the process. Uncertainties of flow stresses, boundary conditions, as well as real deformation rates regarding rotary shear deformation should be elaborated further. It seems inevitable to take the shear deformation into account, either by modifying the strain [101, 106] or by adapting the flow curves, assuming a certain shear rate.

4 Fusion Welding

Electron beam welding was chosen to fusion weld TZM alloy. This chapter briefly explains the electron beam welding technology and the encountered problems during welding of molybdenum and TZM. The main focus was the development of a weld with improved properties and a ductile joint. For that reason, different filler metals were investigated as well. A novel molybdenum cored wire was welded using EBW and the results and potentials are discussed.

4.1 State of the art

Whenever the material is heated above its liquidus temperature during the welding process, the main mechanism of bonding is dilution and epitactic growth of material in their liquid phase and which defines a fusion welding process. The most common welding processes like metal inert gas (MIG) or metal active gas (MAG), among others, are fusion welding processes. The so-called power beam welding processes laser beam welding (LBW) and electron beam welding (EBW) both belong to fusion welding as well. Their unique attribute is their immensely high input energy density, which exceeds their conventional counterparts by multiple orders of magnitude, as listed in table 4.1.

Table 4.1: Comparison of maximum power densities of different fusion welding techniques [108]

Heat source	Max. power density $^{W}/_{cm^2}$
Gas flame	$5 \cdot 10^3$
Electric arc	10^4
Plasma	10^5
Laser beam (continuous)	10^7
Electron beam	10^7

The cause and effects of high power densities, in respect to LBW and EBW, will be discussed in the following sections.

4.1.1 Deep welding effect and the keyhole

The heat in EBW is directly generated in the material by the impact of electrons rather than by heat conduction from an electric arc at conventional welding processes like MIG or MAG. The electrons only penetrate fractions of millimeters into the material (figure 4.1a). Whenever the beam power density exceeds the order of 10^6 $^{W}/_{cm^2}$, the highly focused energy causes a local evaporation of the material, forming a small vapor cavity, the so called “keyhole,” which is depicted in figure 4.1b and c [109]. It is possible to achieve deep and narrow weld beads compared to conventionally produced welds. Then, the reachable depth of the keyhole and therefore the weld is only theoretically restricted by the beam power. The keyhole itself is enveloped by a

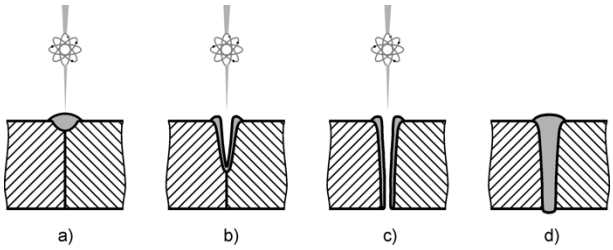

Figure 4.1: The establishing keyhole in the different stages [109]

layer of molten metal [109, 110]. A laser beam, however, is damped by the metal vapor and the effective achievable welding depth is 25–30 mm [73].

When the beam is moved across the work piece, the vapor pressure of the keyhole causes the material to flow around the keyhole to the back of the weld, which eventually forms the typical chevron pattern upon solidification.

One issue in laser beam welding is the low absorption rate of the wave length of the most commonly used lasers (near and far infrared) in most metals. The reason that LBW is industrially feasible nevertheless is, that the absorptivity of molten metal or metal vapor is considerably higher [73, 110]. In EBW, side products of the impact of high velocity electrons are X-rays, elastically reflected electrons, back scattered primary electrons, secondary electrons, and thermal electrons [108]. The magnitude of these effects depends strongly on the material and the welding parameters. Nevertheless, compared to LBW, the efficiency of the energy transfer into the metal is superior in EBW [108].

4.1.2 Electron beam welding

Electron beam welding was invented in the late 1950's as a drilling tool for accomplishing precise and small holes. If the beam moves relative to the specimen, a weld bead develops and soon the technology was adapted for welding purposes [108].

Figure 4.2 shows a schematic principle of an EBW machine: A resistor consisting of a high melting material acts as a cathode. For the cathode, tantalum and tungsten–rhenium alloys are widely in use. A high voltage (up to a few hundred kV) between the resistor cathode and the anode causes electrons to emerge from the cathode and accelerate towards the anode, reaching up to $^2/_3$ of light speed. To promote the emergence of electrons from the metal lattice, the cathode is heated up by an electric current, which induces kinetic energy into the valence electrons of the cathode. The intensity of the beam is controlled by the higher charge of the secondary cathode than the primary cathode's charge. This third electrode, the so called "Wehnelt," or bias, retains the electrons. When the bias voltage is lowered, the electrons travel through the center hole of the anode into the working chamber. With a series of coils which generate magnetic fields, the electron beam is stigmatized and focused. Additional fields permit a rapid deflection (1° per µs) of the beam to form beam deflection figures, to influence the energy distribution during the welding process [73, 108, 111].

4.1.2.1 Process parameters

The beam power is calculated as the product of acceleration voltage and beam current

$$P = U_H \cdot I_B. \tag{4.1}$$

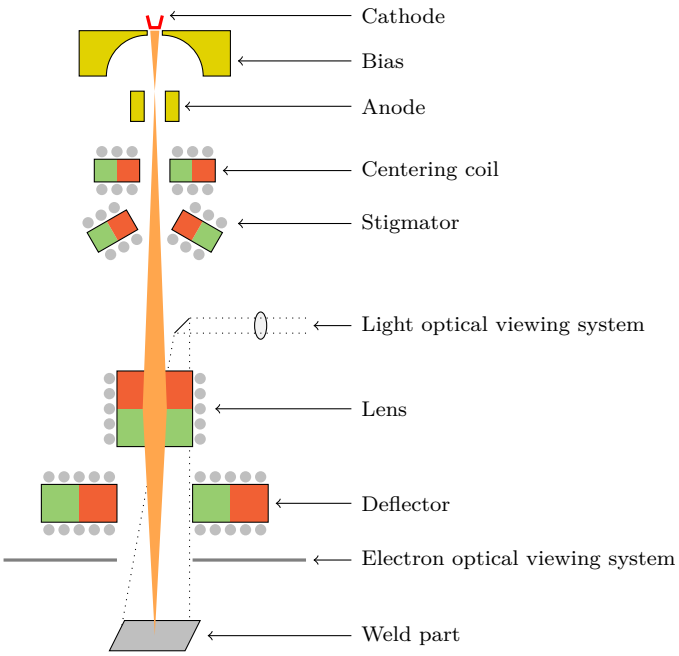

Figure 4.2: Schematic principle of function of an electron beam welding machine [108, 111]

Naturally, if the voltage is reduced, the current has to be raised accordingly to achieve the same nominal beam power. An electric current is defined as the amounts of charges Q per time t,

$$I = \frac{Q}{t}. \tag{4.2}$$

The charges in the case of an electron beam are electrons with a charge of $(-1)\,e$ and a higher beam current causes a higher density of electrons. The physical limiting parameter for the focus of an electron beam is the repulsion between the electrons. A lower beam current therefore enables a better focus. This means for electron beam welding that for the best achievable focus, the highest possible acceleration voltage is required at a given beam power.

Several reports of welds with an acceleration voltage 60 kV are found in literature [17, 31, 112]. This is due to machine capabilities or specifications rather than influence on the weld. So far, no major correlation between the voltage and the resulting weld quality was observed, apart from the achieved beam power [113]. There is, however, an influence on the shape of the weld in deep welding. If the focal distance is moved closer to the top surface, the weld forms a more tapered shape [108]. Figure 4.3 shows the influence of the acceleration voltage and the focal distance on the weld bead.

Investigations have shown that the resulting weld quality is strongly dependent on the performance of the magnetic coils [114].

4.1.3 Temperature field calculation

Daniel Rosenthal proposed a set of solutions for the theory of moving heat sources in metals [115]. He imposed a series of assumptions: (1) Material properties are independent from temperature, (2) a quasi-stationary state with constant heat source speed and heat input, (3) a point heat source, (4) an infinite size of the substrate, and (5) no heat exchange with ambience.

In the case of a thin plate or a sheet, the temperature gradient in z-direction is neglected and

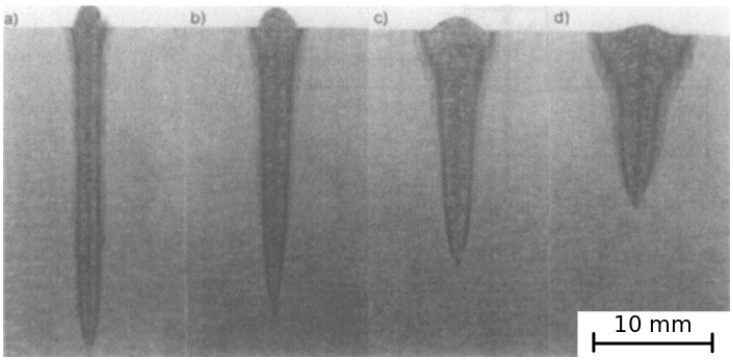

Figure 4.3: Cross sections through welds with a constant beam power of 5 kW but different accelerating voltages and focal distances: (a) 150 kV and 350 mm, (b) 60 kV and 350 mm, (c) 150 kV and 1,200 mm, (d) 60 kV and 1,200 mm [108]

the corresponding 2d equation is given with

$$T - T_0 = \frac{q'}{2\pi\lambda} e^{-\frac{1}{2a}v\xi} K_0\left(\frac{1}{2a}vr\right). \tag{4.3}$$

In this equation, T_0 represents the ambient temperature, q' is the rate of heat per unit length, λ is the thermal conductivity, a expresses the thermal diffusivity which is calculated with λ, the specific heat capacity c_p, and the density ρ as

$$a = \frac{\lambda}{\rho c_p}. \tag{4.4}$$

Further, v is the speed of the heat source, and the spatial coordinates are given with $\xi = x - vt$ in direction of motion, y transversely, and $r = \sqrt{\xi^2 + y^2}$. Finally, K_0 is the Bessel function of order zero. After a few transformations the equation can be re-formulated to give the quasi-stationary temperature field with

$$T - T_0 = \frac{\dot{q}}{2\pi\lambda s} e^{-\frac{1}{2a}vx} K_0\left(\frac{1}{2a}vr\right). \tag{4.5}$$

$\dot{q} = U_H I_B \eta$ is now the heat source power assuming an efficiency of energy transfer $\eta = 0.9$ [108] and s appears as the plate thickness.

4.1.4 Filler metal addition

Due to the deep welding effect, high power beam processes like EBW do not require filler metal. In a butt weld the fusion surfaces should be clean but are sufficiently smooth if roughly machined [108, 116]. Filler metal addition is of interest if a custom alloying is required to specifically alter the metallurgy of the joint [117] or to enable dissimilar joints [118]. The filler metal is inserted by a sheet in between the welding parts, as shown schematically in figure 4.4. Another example is the EBW of thick walled pure copper in PA welding position: The molten material is pulled out of the weld pool by gravity and welding defects like spiking occur. An inserted brass (CuSn6) sheet modifies the weld pool towards a higher viscosity so that the welding defects are suppressed [119]. Successful thick-walled copper welds were also achieved at the institute by substituting the brass sheet by a plasma-sprayed pure tin (Sn) layer prior to welding [120].

The EBW machine at the institute is equipped with a filler wire feed unit that allows the insertion of filler wire with a diameter of 1.2 mm off of conventional wire drums. The main

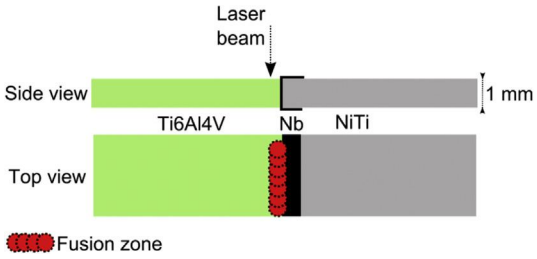

Figure 4.4: Schematic of a weld setup for dissimilar laser beam welding of Ti6Al4V to NiTi with a Nb interlayer [118]

difference in filler metal deposition by wire in EBW compared to arc welding processes is the missing electric field. Therefore, both the the pinching effect σ_P and the electrostatic force F_E are not present. Figure 4.5 shows the forces on a liquid metal droplet at EBW. The gravity force F_G and the beam pressure force F_B act towards the base metal, the force of the vapor cavity F_V opposes the droplet transfer, and finally the adhesion force F_A which points in the direction of the wire feed [121]. Additionally, the surface tension σ_S keeps the droplet formed.

In electron beam additive manufacturing (EBAM) the goal is to deposit the filler metal on the surface of a substrate. To assure a stable and reproducible transfer of the filler metal to the base metal, a liquid bridge between the filler wire and the base metal has to establish [121]. Figure 4.6 shows a schematic of the process. By a proper beam oscillation the beam power is

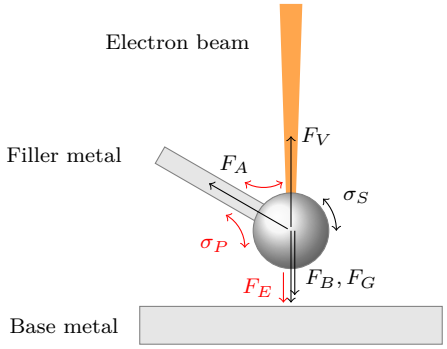

Figure 4.5: Forces on a welding droplet in electron beam welding [121] and the missing forces compared to arc welding marked in red

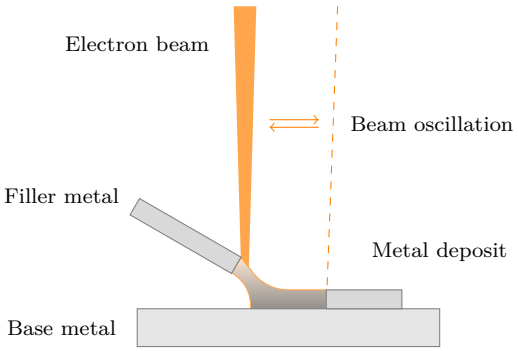

Figure 4.6: Filler metal deposition by a beam oscillation to maintain a liquid metal bridge between the filler wire base metal substrate [121]

distributed rather than punctually transfered, which enables the forming droplet to contact the base metal surface and solidify continuously.

4.1.5 Classification of EBW

Electron beam welding is classified according to EN ISO 15609-3:2004 [122]. The according parameters are listed in table 4.2.

Table 4.2: Parameters of EBW according to EN ISO 15609-3:2004 [122]

Welding parameters		
Acceleration voltage	U_H	kV
Beam current	I_B	mA
Lens current	I_L	A
Beam deflection		constant/periodic, figure
Overlap, slope in, slope out		s, mm, °
Slope profile		
Mechanical parameters		
Welding direction		
Welding speed		$^{mm}/_{s}$
Details about welding speed variation		
Feed rate, -direction, -position, and -angle of filler material		
Other parameters		
Working distance		mm
Pressure within the beam gun		mbar
Pressure within the working chamber		mbar

4.1.6 Electron beam welding of molybdenum

4.1.6.1 Process control

The welding of molybdenum in 8 mm deep welds is feasible using normal welding practices of de-focusing, beam oscillation, and beam offset, among others [108]. EBW experiments in 2 mm TZM sheets included a pre-heating above the ductile–brittle transition temperature to avoid cracks and a post weld heat treatment at 1000°C for 2 h in high vacuum to relieve weld stresses [14]. Welding results of molybdenum by tungsten inert gas (TIG) welding, often also called gas tungsten arc (GTA) welding were reported [17, 20]. Kolarikova et al. compared EBW and TIG welding of thin Mo sheets. They were able to produce a sound weld without macroscopic defects, however, the fracture elongation ranged from 1–2%. Further, they concluded that EBW was to prefer over TIG, because TIG resulted in a higher total heat input which resulted in inferior hardness and microstructure [123].

4.1.6.2 Metallurgy

Electron beam welding has been tested on refractory metals including molybdenum with some success. The biggest problem still remaining is a brittle joint at room temperature, which is caused by oxygen enrichment on grain boundaries, which impair the strength of a molybdenum

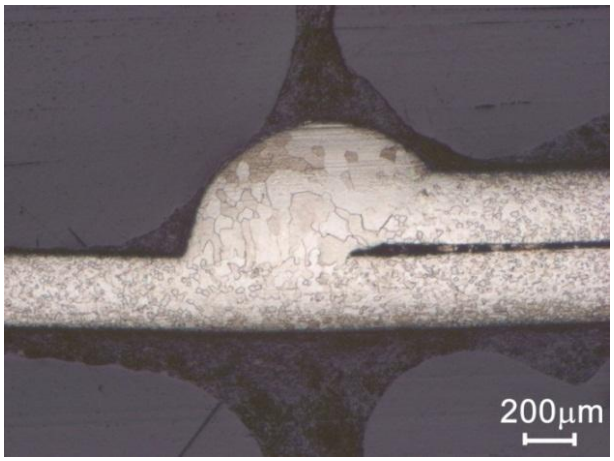

Figure 4.7: Macroscopic cross section of a Mo–Mo joint of 0.2 mm sheets by EBW [123]

joint the most [17]. Apparently even in vacuum enough oxygen was present in the residual ambience, an insufficiently clean surface, or as impurity in the material, since only a few ppm of oxygen suffice to negatively influence molybdenum. Figure 4.7 shows the joint of two overlapping 0.2 mm sheets, welded by EBW [123]. The excessive grain growth in the weld zone can be observed.

Wadsworth et al. [124] investigated the welding behavior of TZM by EBW, LBW, and TIG. They reported brittle failure of the welds during tensile tests, regardless of welding technique. Optical microscope investigations revealed precipitations within the grains of the FZ and precipitates on the grain boundaries in the HAZ, as shown in figure 4.8. Fracture surfaces and grain boundaries were investigated by Auger electron spectroscopy (AES) and it was concluded that no excessive oxygen was present on the grain boundaries in the weld zone. Instead they suggested that Mo-carbides were formed during solidification and precipitated on the grain boundaries, but simultaneously ruled out that those carbides caused the embrittlement. The argument was that coarsely recrystallized TZM achieved up to 40% ductility while exhibiting a similar microstructure like the HAZ of EB-welded TZM. The conclusion was that the brittle fracture behavior was a result of the tensile testing method and strain localization effects rather than the intrinsic brittleness of the welded material.

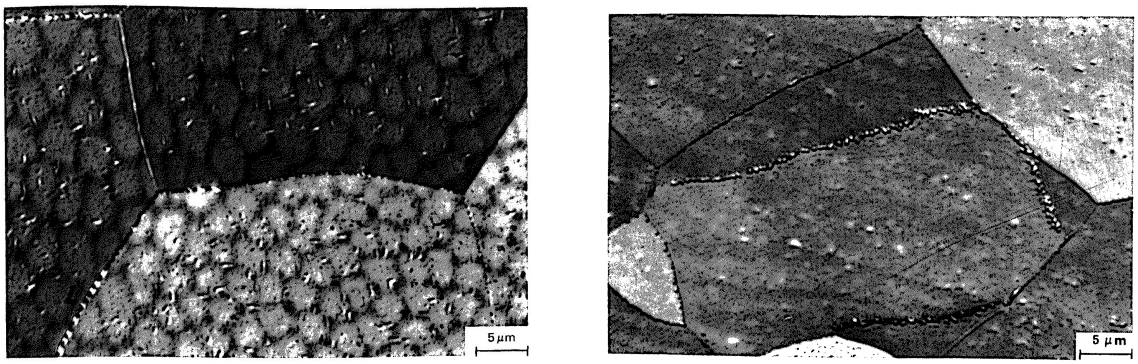

(a) (b)

Figure 4.8: (a) Fusion zone of EB welded TZM with intragranular precipitation and (b) the HAZ with strong precipitation visible on the grain boundaries [124]

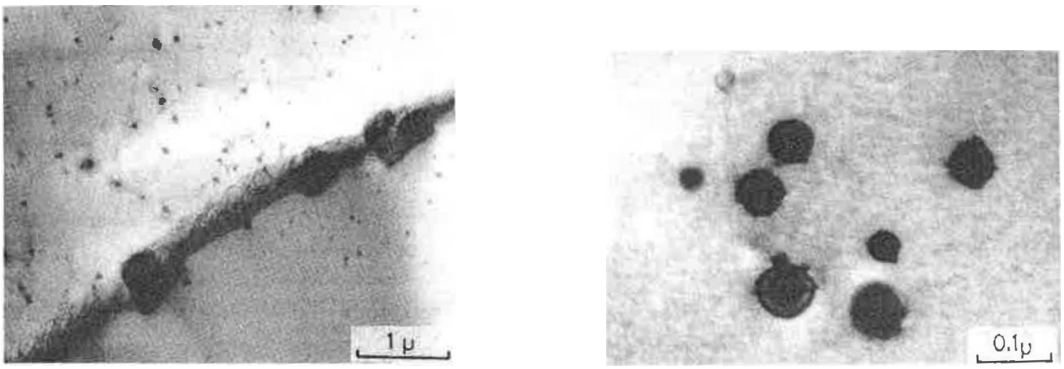

(a) (b)

Figure 4.9: (a) Grain boundary precipitates in the FZ of post-weld carburized TZM and (b) small carbides visible in the matrix [31]

Fumio Morito studied EB welding of powder metallurgic molybdenum and vacuum arc cast TZM [31] and also performed post-weld carburization in some welds. For this purpose, carbon was deposited onto the finished welds and the sheets were treated for 30 min at 1,500°C, which resulted in an increase of C content by 20 wt.ppm in Mo and 40 wt.ppm in TZM. Afterwards, small carbide precipitates on the grain boundaries as well as in the Mo matrix were observed, as shown in figure 4.9. It was reported that the carburized weld samples showed an increase of the yield stress and the fracture elongation.

Cockeram et al. [125] experimented with custom alloying of Al, Zr, B, and C to pure Mo base metal to create alloys with improved ductility after EBW. They argued similarly to Morito that C and B improved the grain boundary strength but reported that excessive amounts of Zr resulted in brittle intermetallic phases which act as crack initiation sites. On the contrary, Wang et al. [126] reported that a Zr interlayer between TZM sheets—resulting in 1.32 wt.%—improved the grain boundary strength and a mixed fracture.

4.1.6.3 Mechanical properties

The EB welding of molybdenum and TZM was reported to lead to a drop of the hardness from the BM into the HAZ and an impaired ductility compared to the base metal [112, 127]. The hardness increased again in the FZ as a result of precipitation hardening [127]. EBW was recommended by Sun and Karppi [128] for welding dissimilar refractory metals. They pointed out that due to the low specific energy input the tendency of recrystallization which would raise the DBTT was reduced.

EB welds of Mo and TZM resulted in a decrease of the tensile strength compared to the respective base metals by about 40% [14]. The even more severe issue, however, was the substantial loss of ductility, where Mo and TZM only exhibited a few percent of elongation in the tensile tests. This was attributed to the grain growth in the fusion zone and the heat affected zone.

Morito's results of post-weld carburized Mo and TZM welds showed an improved tensile strength as well as improved ductility. First, ductile behavior in tensile tests was observed for all welds above 200°C, suggesting a DBTT in that temperature region. Further, post-weld carburized TZM even exhibited a ductile failure with 27% elongation at room temperature. Morito argued that the carbon addition resulted in Mo_2C precipitation on the grain boundaries, which strengthened the latter by forming a strong carbide–matrix boundary instead of a high energy incoherent boundary [31].

4.1.7 Effects of heat treatment

Almost all authors reported relief to embrittlement by post-weld heat treatment which improves the grain boundary cohesion [14, 17]. Morito [31, 47] stressed the importance of post-weld heat treatment as well and found the optimum post-weld heat treatment temperature in vacuum for EB welds of TZM to be 1,200°C. He reported that nitrogen disappeared while carbon diffused to the grain boundaries, as observed in figure 4.10, and concluded that the carbon content on the grain boundaries is the primary determining factor of the ductility and DBTT of TZM.

4.1.8 Summary

Electron beam welding is a promising technology for welding molybdenum and refractory metals in general. Research has clearly demonstrated the superiority of EBW over other fusion welding processes due to its high energy density, which minimizes the amount of melting, re-solidification, and recrystallization.

Despite the advantages, as naturally in fusion welding processes, a molten and re-solidified microstructure is produced in EBW. As discussed by many authors, the associated impairing of the mechanical properties and especially the ductility in the fusion zone and the recrystallized heat affected zone are unresolved issues. For welding molybdenum, it is assumed that the biggest problems to overcome will be: (1) Preventing grain coarsening in the fusion zone and (2) sustaining the ductility of the weld and the HAZ to an acceptable extent.

The flexibility of the electron beam regarding beam deflection, pre-heating, and beam split are to be elaborated. Further, the feasibility of filler metal addition has to be investigated and potential filler metals are to be explored.

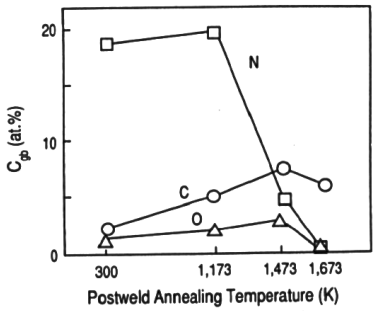

Figure 4.10: Concentration of N, C, and O on the grain boundaries of EB welded TZM in the fusion zone [47]

4.2 Experimental

4.2.1 Base metal

Figure 4.11 shows the microstructure of the TZM base metal in as-recieved condition. The production route was sintered, hot rolled, and stress relieve annealed at 1,200°C under vacuum for 2 h. In the figure elongated grains in rolling direction, accompanied with some residual porosity from the sintering process are observed.

4.2.2 EBW equipment

For the electron beam welding experiments, the *pro-beam EBG 45-150 K14* electron beam welding machine at the IMAT was used. Figure 4.12 shows the machine in the laboratory facilities. Its characteristics were a beam gun with up to 150 kV acceleration voltage, a maximum beam current of 300 mA, and thus 45 kW maximum beam power. The working chamber was encased in lead as X-ray radiation emerges from the weld bead if the acceleration voltage exceeds 60 kV [108]. The operation vacuum in this machine was $5 \cdot 10^{-4}$ mbar, and the working distance varied between 600 and 1,000 mm, depending on the setup. The machine also contains a wire feed device which can feed 1.2 mm wire from a conventional filler wire roll continuously into the weld pool. For

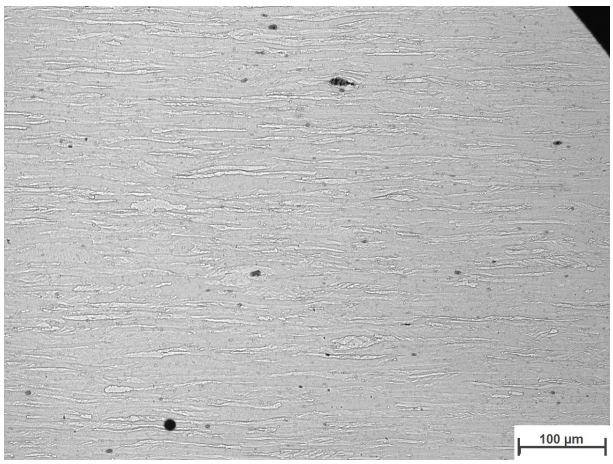

Figure 4.11: TZM 2 mm sheet base metal sintered and rolled. Elongated grains are observed in rolling direction as well as residual porosity (black spots) from the sintering process.

Figure 4.12: The *pro-beam EBG 45-150 K14* EBW machine at the institute

welding with filler wire the working table had to be raised in order to enable the wire feed to apply the filler metal appropriately.

4.2.3 Beam deflection figures

To vary the energy distribution, in EBW it is common practice to use a beam oscillation rather than de-focusing. One of the reasons is depicted in figure 4.13: The beam intensity is described by a Gaussian function [129] and a de-focused beam basically just softens the intensity distribution of the beam. If the focus is maintained and the beam is oscillated, the steep flank of the Gaussian distribution is retained and the intensity is distributed evenly over the oscillation amplitude. This promotes a sharper edge of the weld pool and potentially a more stable keyhole.

The experiments were conducted using no beam deflection with sharp focus (point) and a circular deflection figure with ∅0.5 mm for welding, and concentric circles and ellipses for filler wire deposition, as depicted in figure 4.14. The scanning frequency of the deflection figures was set constant to 1,000 Hz.

4.2.3.1 Beam split

The deflection coils in the EBW machine allow a fast deflection of the beam in a way that seperate weld pools can be established. A power distribution is also possible. Figure 4.15 shows a combined process, where first the filler wire is deposited, followed by two full penetration welds to ensure a sound dilution of the filler metal.

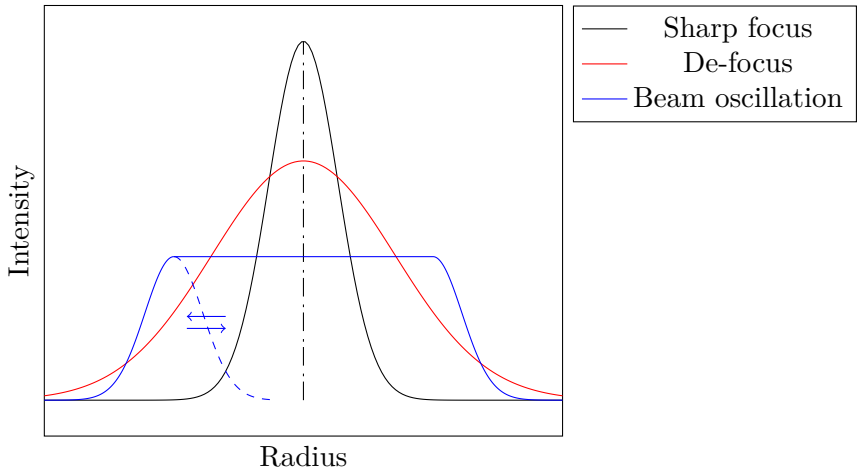

Figure 4.13: Difference in the intensity distribution between a de-focused beam and a beam oscillation: With a beam oscillation the intensity is more evenly distributed over the desired oscillation amplitude.

Figure 4.14: Beam deflection figures used in the experiments: (a) Point, (b) circle, (d) concentric circles, and (d) concentric ellipses

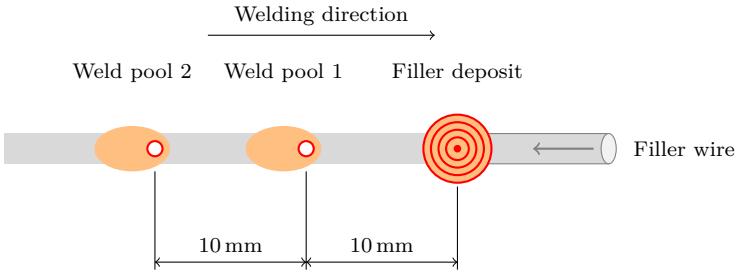

Figure 4.15: Combined beam figure

4.2.4 Welding setup

Clamping of the sheets is of foremost importance to ensure a good alignment of the sheets during the process. For this reason, an L-profile aluminum clamping device was built to hold the weld parts in place. Further, a setup with collets was used in some experiments as well, as observed in figure 4.16

For the butt joints the sheets were aligned evenly with no weld gap, as sketched in figure 4.17a. ISO 9692-1:2003 [130] suggests a V-seam with 8° opening angle for electron beam welds with wire filler metal (figure 4.17b). In the course of the experiments it was established that a simple butt seam with a small gap in the range from 0.1–0.2 mm (figure 4.17c) lead to the same joint quality like a V-seam. Further, in 5 mm sheet welds a Y-seam was also welded (figure 4.17d).

4.2.5 Welding and characterization procedure

To systematically approach the welding of TZM sheets, first, bead-on-plate and butt weld experiments were carried out to gain an understanding of the required process parameters and their

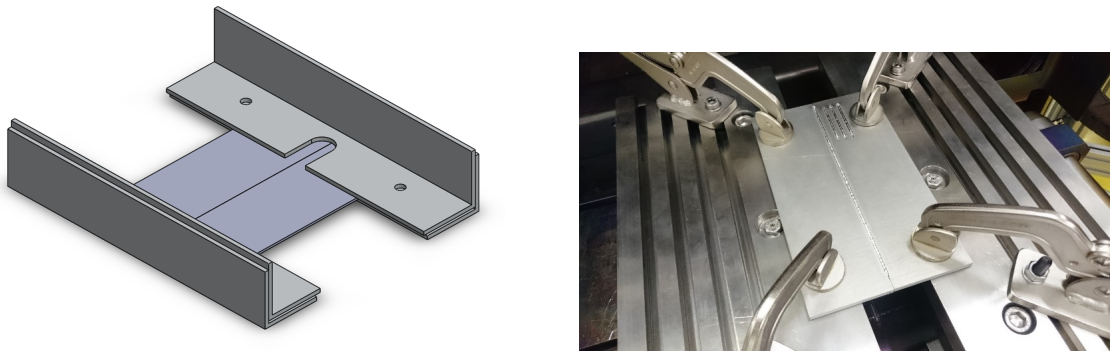

(a) (b)

Figure 4.16: Clamping systems for welding: (a) L-profile clamping and (b) collet clamping

(a) (b) (c) (d)

Figure 4.17: Weld joint setups: (a) butt seam, (b) V-seam with $2 \times 4°$ angle according to ISO 9692-1, (c) butt seam with 0.2 mm gap, and (d) Y-seam

interactions. Then, the filler metal insertion by filler wire was elaborated and tested. Finally, different filler metals were investigated.

The characterization of the welds was done by visual assessment of the regularity of the weld seams. Selected visually approved welds were investigated by X-ray imaging to visualize porosity. The main investigation method was the characterization of the microstructure, particularly the grain sizes and dimensions of FZ and HAZ. Further, hardness lines were recorded to estimate the mechanical strength of the joint. Tensile test samples were only produced from the first butt weld experiments without filler to correlate microstructure and hardness to tensile strength. Finally, because the welding results with cored wire were promising, a mechanical characterization by tensile and bending tests was carried out again.

4.2.5.1 2 mm butt welds

For the butt welds of TZM sheet metal the voltage was set to 150 kV to achieve the best possible focus and no deflection figure was used. After some preliminary experiments, a 2^n design of experiment test matrix with $n = 4$ parameters in two levels was drafted with the parameters listed in table 4.3. Pre-heating was conducted in-situ by the EB, by scanning a 40×120 mm rectangle with 15 mA beam current for 60 s. The resulting temperature was approximately 400°C. Post-weld heat treatment was done by *Plansee SE* by their standard stress-relief procedure for TZM in a vacuum furnace at 1,200°C for 2 h.

Table 4.3: Parameter levels for the 2^4 DoE of 2 mm TZM sheet butt welds

Parameter	−	+
Beam current I_B	15 mA	25 mA
Welding speed v_W	10 $^{mm}/_{s}$	30 $^{mm}/_{s}$
Pre-heating	no	yes
Post-weld heat treatment	no	yes

In the experiments with filler metal the optimal process parameters were determined in a separate test matrix, based on the results of the butt weld experiments. For the final welds, the beam current was varied depending on the filler metal between 17.7 mA (V filler) and 21.7 mA (VACTZM filler). The beam deflection figure was set to a circle for welding with a diameter between 0.5 mm and 1.2 mm. For filler metal deposition in a separate step, concentric circles or ellipses were used as deflection figure. The wire feed rate was set between 0.58 $^{m}/_{min}$ and 1.2 $^{m}/_{min}$, depending on the experimental setup, the filler metal, and the welding speed.

4.2.5.2 5 mm butt welds

The beam current for butt welds without filler metal was varied between 40 mA and 50 mA at 30 $^{mm}/_{s}$. The wire feed rate was investigated between 3.5 $^{m}/_{min}$ and 4.5 $^{m}/_{min}$, while at deposition prior to welding it was reduced to 2–3 $^{m}/_{min}$, as the welding speed was reduced to 10 $^{mm}/_{s}$ and 20 $^{mm}/_{s}$, respectively.

4.2.6 Filler metals

Alloying of the fusion zone by targeted variation of the chemical composition of the filler metal is widely used in industrial welding processes. In the course of this project, three different filler

metals were used to investigate their suitability and potential for improving the mechanical properties of TZM sheet welds.

4.2.6.1 Vanadium

Vanadium (V) was chosen due to its full solubility in molybdenum [1, 46], thus no potentially detrimental intermetallic phases can be formed in the weld. However, literature on the mechanical properties and hardness values of the Mo–V solid solution crystal was not available.

4.2.6.2 Vacuum arc cast TZM

The production of TZM by vacuum arc casting (VAC) results in an even lower residual oxygen content than powder metallurgically produced TZM. This bears the potential welding with the same filler as the base metal but also reducing the residual oxygen in the weld and to inhibit the formation of oxides on grain boundaries.

4.2.6.3 Molybdenum cored wire

To increase the flexibility in composition from massive filler wire further, cored wire technology was developed [131]. However, a cored wire with molybdenum was never produced. In the course of the project, *voestalpine Böhler Welding GmbH* and *Plansee SE* collaborated to produce a novel cored wire specifically for welding Mo. Figure 4.18 shows an overview of the production process which resulted in the first custom cored pure molybdenum wire.

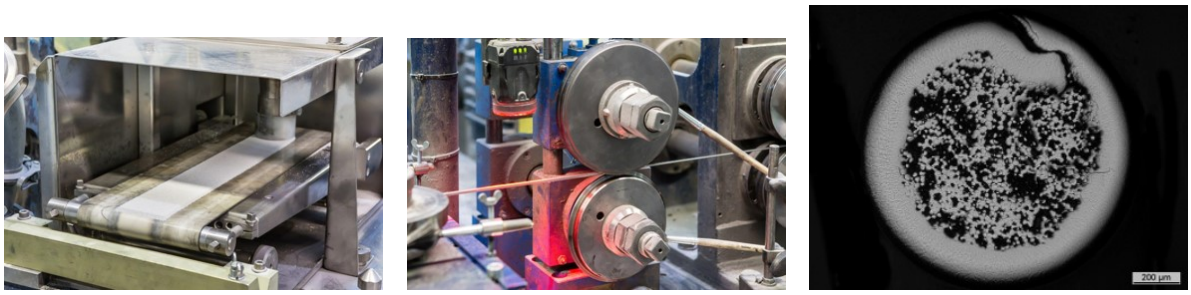

(a) (b) (c)

Figure 4.18: Production route of Mo cored wire: (a) Powder insertion into a pre-bended Mo strip, (b) rolling and closing of the strip to a wire; (c) Microsection of the finished wire

4.3 Results

4.3.1 Electron beam welding of 2 mm TZM

As a reference, figure 4.19 shows a bead-on-plate weld in TZM at a beam current of 20 mA (3.0 kW) and a welding speed of 20 $^{mm}/_{s}$. The image shows nicely distinguishable zones, the base metal (BM) with typical elongated, small grains from the rolled semi-finished sheet metal. In the heat affected zone recrystallized grains are observed with increasing grain size towards the fusion zone. The heat affected zone was determined by the border between BM and visually recrystallized grains, which occur beyond the recrystallization temperature of 1,400°C [12]. Finally, large new grains in the fusion zone which re-solidified from the fusion lines towards the weld center.

4.3.1.1 Microstructure

Figure 4.20 shows two microsections of EB butt welds of 2 mm TZM welds with (a) 15 mA (2.25 kW) at a welding speed of 30 $^{mm}/_{s}$ and (b) 25 mA (3.75 kW) at 10 $^{mm}/_{s}$. It is easily observed that the sizes of the fusion zone (FZ) and the heat affected zone (HAZ) are much smaller at lower beam power and higher welding speed. Concerning the beam power, the DoE revealed that a higher beam power resulted in a larger grain size in the FZ but had little effect on the grain size of the HAZ. Further, the weld's porosity was also the least at low beam power [132].

The X-ray image in figure 4.21b shows that at a high energy input and low welding speed the weld bead exhibited periodically occurring bonding faults. Furthermore, pores occurred frequently. If welded with low beam power and high welding speed (figure 4.21a) the weld bead was more regular, only occasionally showing deviations. The porosity was also much less.

A higher welding speed resulted in a smaller width of both the FZ and the HAZ. Moreover, the welding speed affected the grain size of the HAZ much more than the beam power, with a smaller grain size observed at higher speeds.

Assuming material properties with the values in table 4.4, Rosenthal's equation 4.5 (page 76) can be evaluated for different beam powers $\dot{q}$ and welding speeds v. Figure 4.22 shows the four resulting temperature fields of the DoE, with subfigures (a) and (d) corresponding to the macrosections of figure 4.20a and b, respectively.

The innermost contour lines represent the melting temperature of TZM with 2,620°C, thus

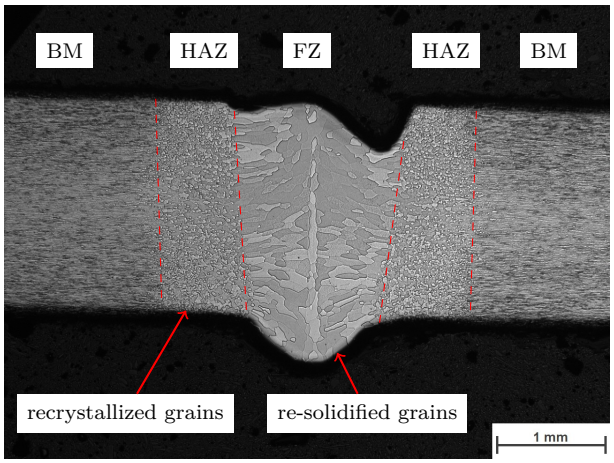

Figure 4.19: EB bead-on-plate weld in TZM with $I_B = 20\,\text{mA}$ and $v_W = 20\ ^{mm}/_{s}$

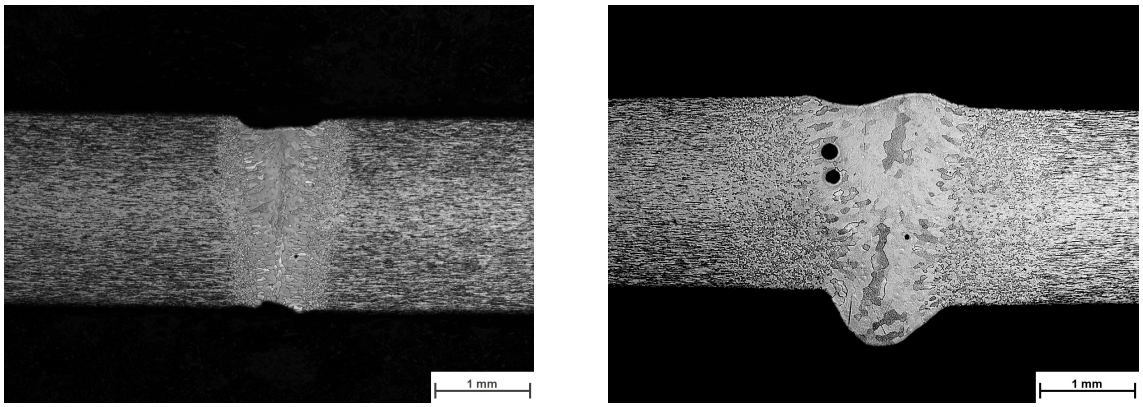

(a) (b)

Figure 4.20: Electron beam welds of TZM sheets with (a) 15 mA and 30 $^{mm}/_{s}$ and (b) 25 mA and 10 $^{mm}/_{s}$

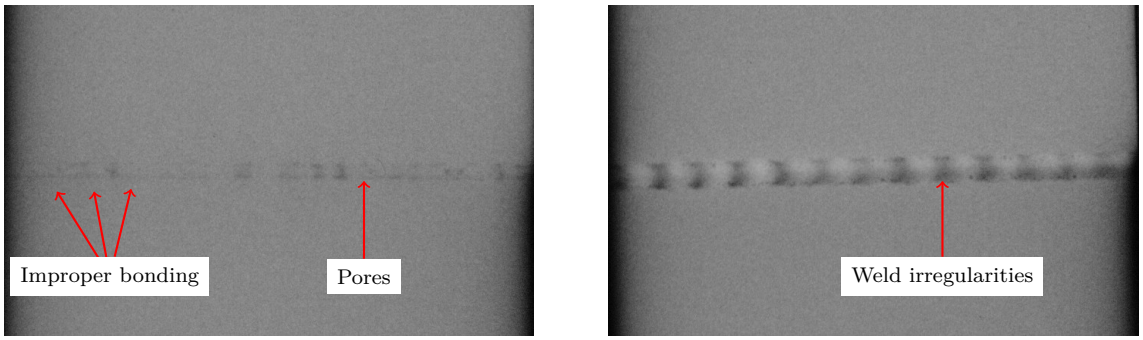

(a) (b)

Figure 4.21: X-ray images of electron beam welds of TZM sheets with (a) 15 mA and 30 $^{mm}/_{s}$ and (b) 25 mA and 10 $^{mm}/_{s}$

corresponding to the resulting fusion lines. Compared to the macrosections of the welds in figure 4.20 of course, the fusion lines of the calculations do not match. As mentioned before, Rosenthal's equation implies various simplifications, however, it is suitable to show a general trend of the influence of the investigated welding parameters on the resulting temperature field.

The obviously different magnitude of the temperature fields in 4.22a and d resulted in the different microstructure observed in figure 4.20.

Pre-heating resulted in larger grains in both the FZ and HAZ, with the same tendency of even larger grains at high beam power. Further, it increased the average width of FZ and HAZ. This is due to the resulting softer temperature gradient during cooling that results in a longer time period for the grains to grow bigger. Contrary to common recommendations [12]

Table 4.4: Physical properties of TZM at 1,000°C [12] for Rosenthal's calulation

Thermal conductivity λ	105 $^{W}/_{m\,K}$
Specific heat capacity c_p	315 $^{J}/_{kg\,K}$
Density ρ	10.20 $^{g}/_{cm^2}$

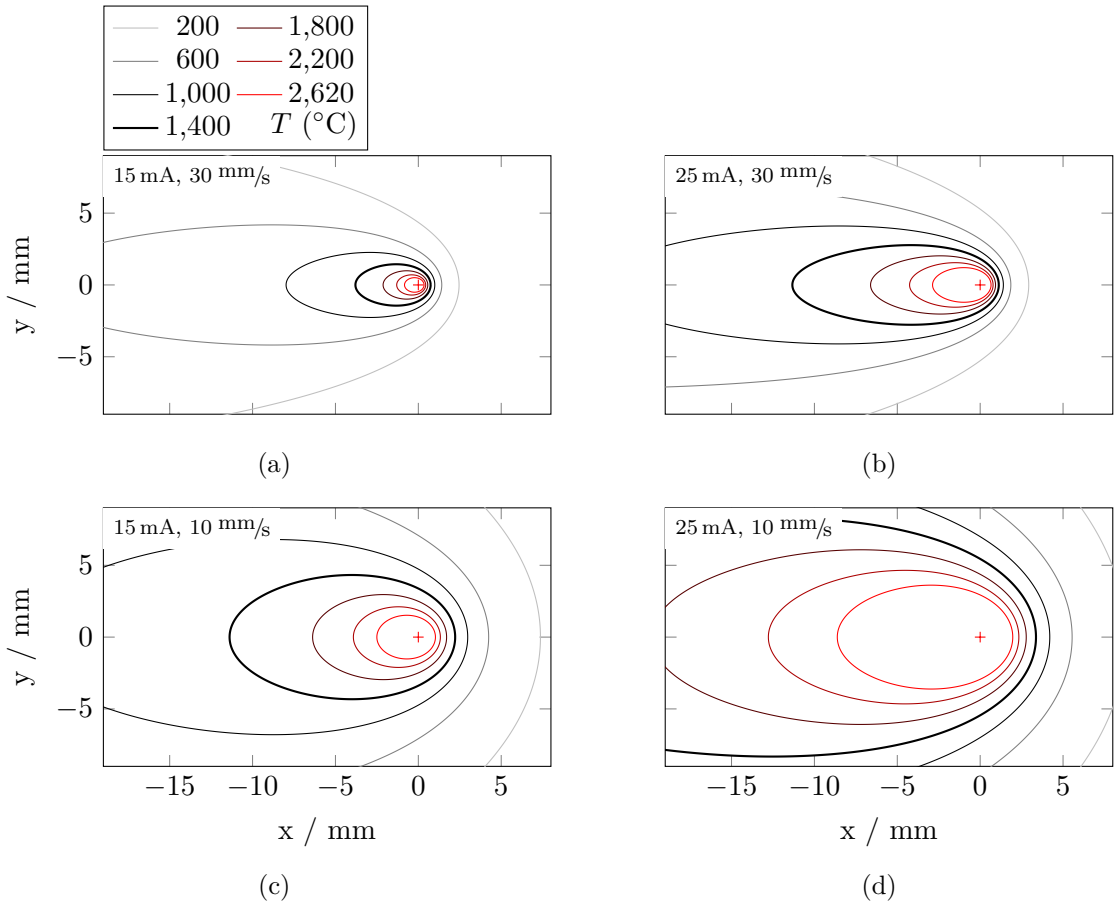

Figure 4.22: Contour plots of the results of the Rosenthal calculations. The lines represent isotherms, the cross at [0,0] marks the position of the electron beam, and x is the welding direction. It is observed how the resulting temperature field changes qualitatively with the variation of welding speed and beam current. Subfigure (a) corresponds to the macrosection of figure 4.20a and (d) to figure 4.20b.

no improvement of microstructure or susceptibility to cracking was observed with pre-heating, therefore it is concluded that pre-heating does not improve the weld quality in EBW of TZM.

4.3.1.2 Hardness

Figure 4.23 shows two EB welds with three hardness lines across the FZ and HAZ. It is observed that the base metal hardness of approximately 290 HV1 drops in the HAZ and continues through the FZ. The resulting average hardness values were between 200 and 227 HV1. Post-weld heat treatment lowered the resulting hardnesses between 5 and 10 HV points. The highest hardness values of FZ and HAZ was observed at 15 mA and 30 $^{mm}/_{s}$ (figure 4.23a). The most influencing parameter on hardness was the weld speed with yielding better values at higher speeds.

4.3.1.3 Ultimate tensile strength

Finally, the ultimate tensile strength (UTS) was determined in as-welded condition. This means that due to the notches of the weld bead the results are only partly comparable to the base metal results. Figure 4.24 shows the results of the DoE samples in as-welded (AW) and post-weld heat

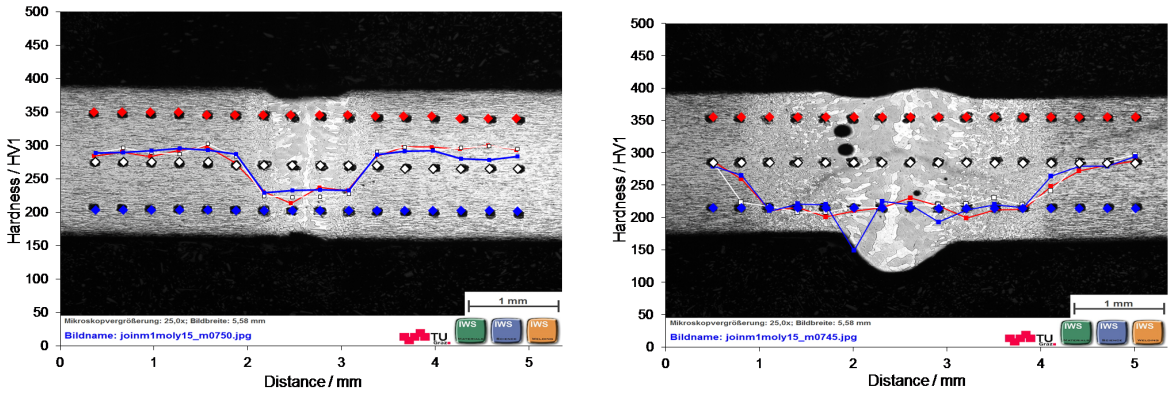

(a) (b)

Figure 4.23: Hardness lines of electron beam welds of TZM sheets with (a) 15 mA and 30 $^{mm}/_{s}$ and (b) 25 mA and 10 $^{mm}/_{s}$

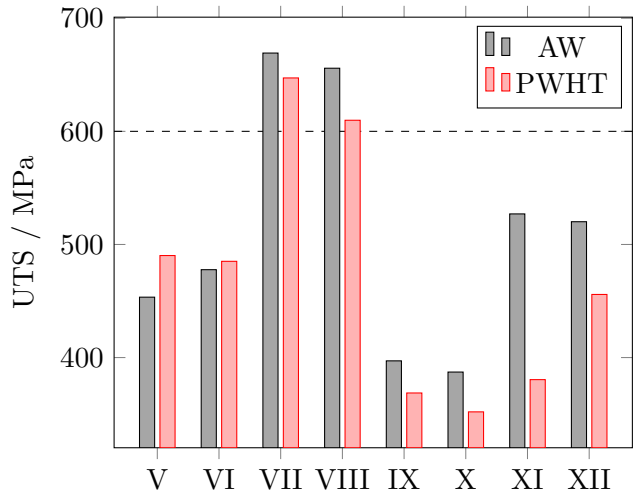

Figure 4.24: Ultimate tensile strength of as-welded and post-weld heat treated samples. The dashed line represents the tensile strength of fully recrystallized TZM base metal [12].

treated (PWHT) condition. It is observed that welds VII and VIII yielded the best results, with values between 610 and 669 MPa they are higher than the tensile strength of fully recrystallized base metal of 600 MPa [12] but still below the as-worked base metal value of 861 MPa; weld VII (15 mA, 30 $^{mm}/_{s}$) in as-welded condition was 77.8% of the UTS of the base metal.

The contour plots of the DoE of UTS are displayed in figure 4.25. It is observed that the beam current had only little influence on the UTS, except in PH and PWHT condition, while a fast welding speed lead to the best UTS values. Pre-heating reduced the UTS values overall, because of the resulting larger grain sizes in FZ and HAZ. Post-weld heat treatment, however, also reduced the obtained UTS values. It has to be noted that the tensile samples were extracted in as-welded condition and subsequently heat treated. A brittle microstructure like the present TZM welds could suffer from small cracks during cutting, which may propagate during the heat treatment and ultimately compromise the tensile strength values. This may also be the reason for the observed shift of influence of PH and PWHT in figure 4.25d.

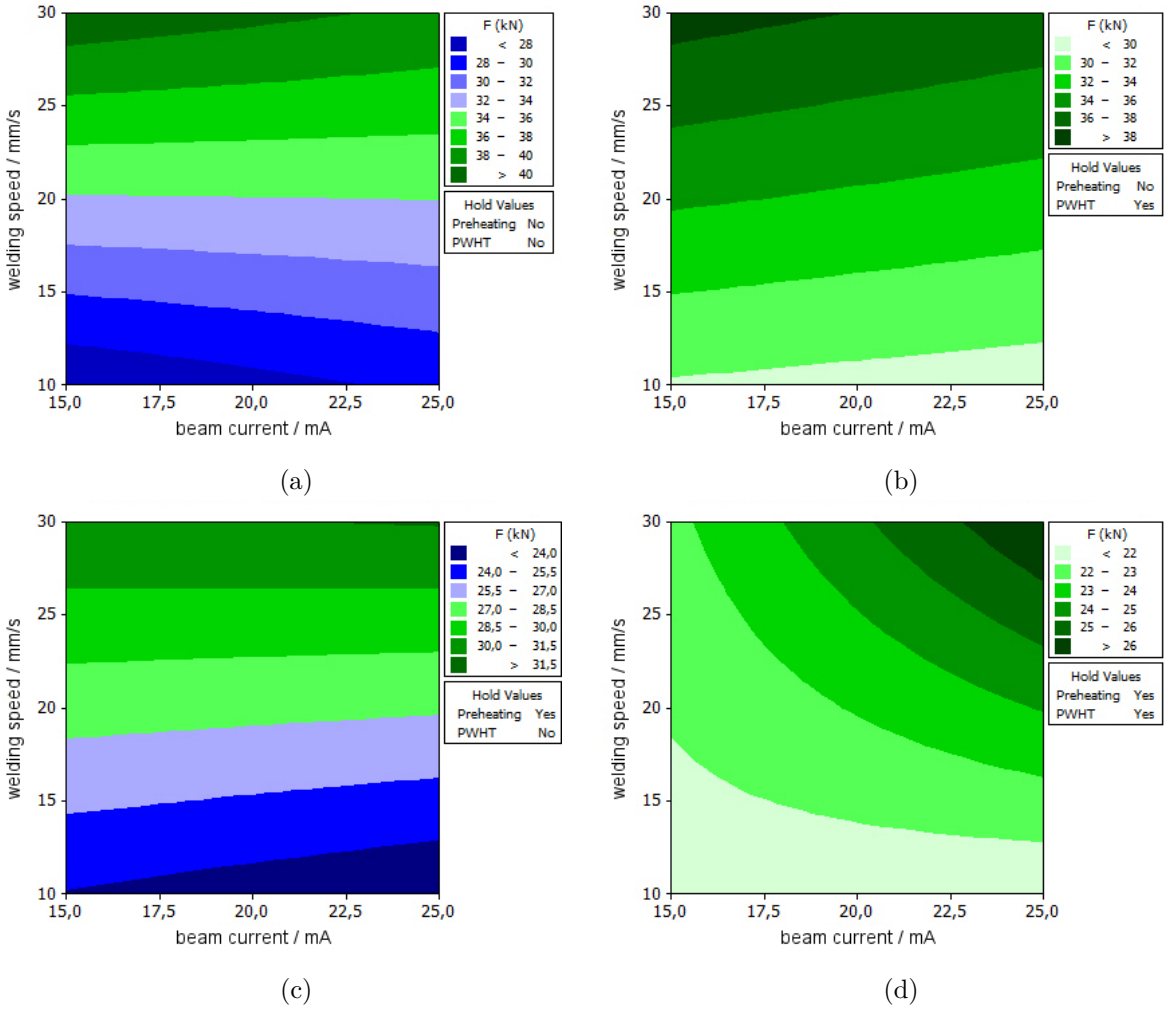

Figure 4.25: Contour plots of beam current and speed on UTS, with (a) no PH, no PWHT, (b) no PH, with PWHT, (c) with PH, no PWHT, and (d) with PH and with PWHT

Preliminary experiments showed an intergranular fracture mode, as observed in figure 4.26a. In this case it was concluded that the weak point in the bonding were the grain boundaries. The experiments of the presented DoE all showed either a mixed fracture mode or mostly transgranular, as observed in figure 4.26b.

Kadokura et al. [133] found that small additions of carbon changed the fracture mode from intergranular to transgranular in pure Mo. It may be supposed that a significantly slower welding speed resulted in a lower C content or less beneficial C distribution in the FZ of TZM.

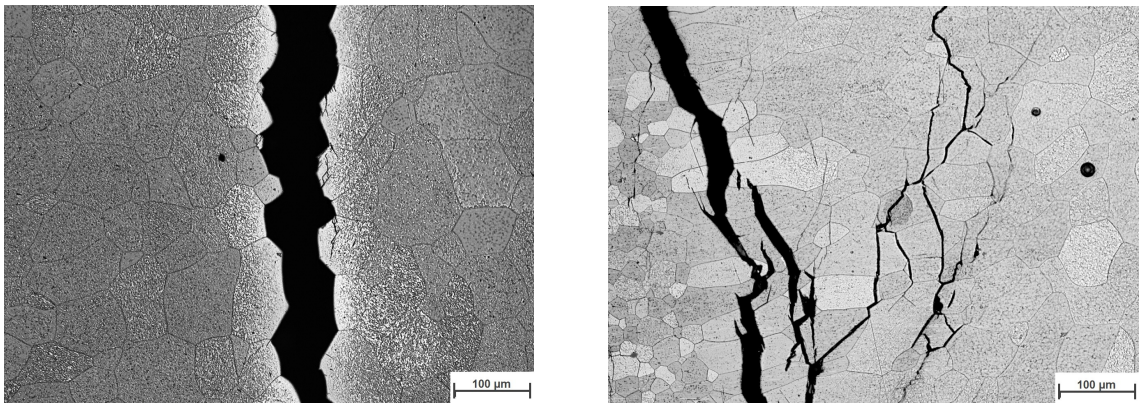

(a) (b)

Figure 4.26: Comparison of the tensile test rupture interfaces of (a) a preliminary experiment (15 mA, 5 $^{mm}/_{s}$) that showed intergranular fracture and (b) experiment VI of the DoE which exhibited a transgranular fracture mode

4.3.2 Electron beam welding of 2 mm TZM with filler metal vanadium

Figure 4.27 shows the macroscopic top view of a preliminary test weld with V filler wire. It is observed that due to instationary filler metal transfer a periodic droplet formation occurred and small spatter that landed on the top sheet, leaving vanadium smoke trails. V smoke condensation is also observed on the bottom sheet. The clamping marks from the L-clamps are visible as no smoke condensation is occurred in these areas. Apparently a fraction of the vaporized V was deposited on the surface of the TZM sheets during the welding process.

Cross sections of the preliminary welds showed an irregular distribution of V, owing partly to the strong droplet formation. Further, brittle cracking during and immediately after the welding process occurred perpendicularly to the welding direction. This issue could mostly be resolved by leaving the vacuum chamber of the EBW machine closed for approximately 7–10 min after the welding process, thus reducing the cooling rate. Figure 4.28 shows the temperature of a TZM

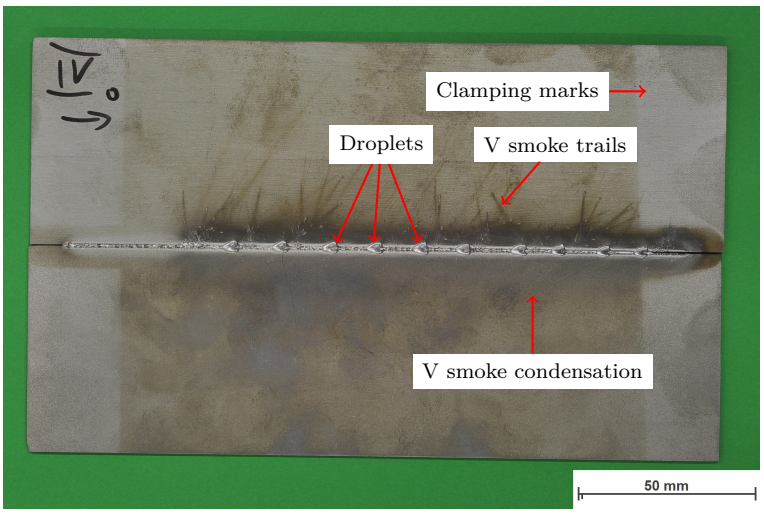

Figure 4.27: Macroscopic top view of preliminary EB weld of TZM sheets with V filler metal

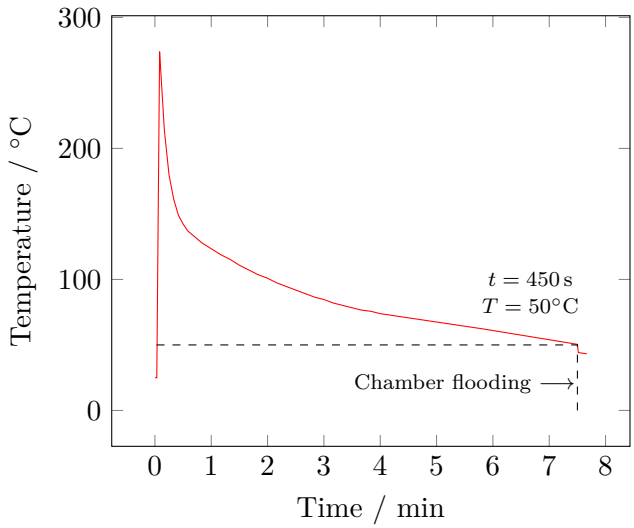

Figure 4.28: Measured temperature during an EB weld by a thermocouple placed in 8 mm distance to the weld. It is observed that the temperature at the position dropped to 50°C after roughly 7 1/2 min after the electron beam passed.

sheet measured in 8 mm distance from the weld center line. It is observed that the temperature dropped from 270°C to 50°C in roughly 7 1/2 min, where a small drop is observed which resulted from the occurring convection evoked by flooding the vacuum chamber.

Figure 4.29 shows the top and bottom view of a TZM weld where the V filler was deposited prior to welding. The weld bead quality was good, showing a regular top surface and continuously formed weld root. A V smoke deposit was visible on the top surface (figure 4.29a) and small lateral cracks occurred on the bottom side (figure 4.29b). During welding it was observed that some cracks occurred directly after the filler metal deposition. This indicates that residual stresses resulted from the different heat expansion coefficients of TZM and V which were high enough to initiate cracking.

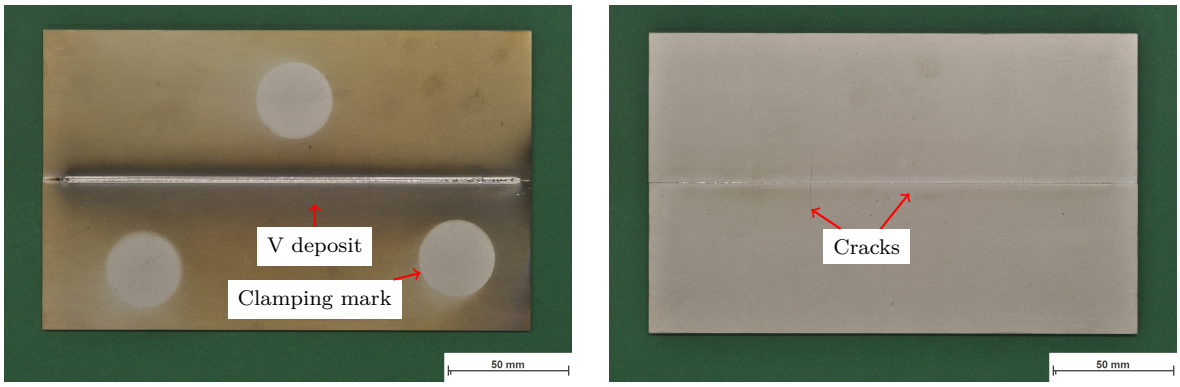

(a) (b)

Figure 4.29: Macro photographs of a TZM sheet metal welded with V filler wire: (a) Top view and (b) bottom view

4.3.2.1 Microstructure

Figure 4.30 shows an etched cross section of the resulting weld bead. The V filler was mostly diluted in the top region of the weld, as confirmed by a energy-dispersive X-ray spectroscopy (EDX) map (figure 4.31). The hardness measurements in figure 4.32 shows that the values increased up to 390 HV1 in the V-enriched regions. However, the bottom hardness line also peaks in the weld zone—although only at roughly 300 HV1—which could be due to the small amount of V present.

Further it has to be noted that the TZM base metal in this particular experiment was from a different batch and exhibited only a hardness of 220–230 HV1, which is considerably lower than the base metal of the other experiments in this section.

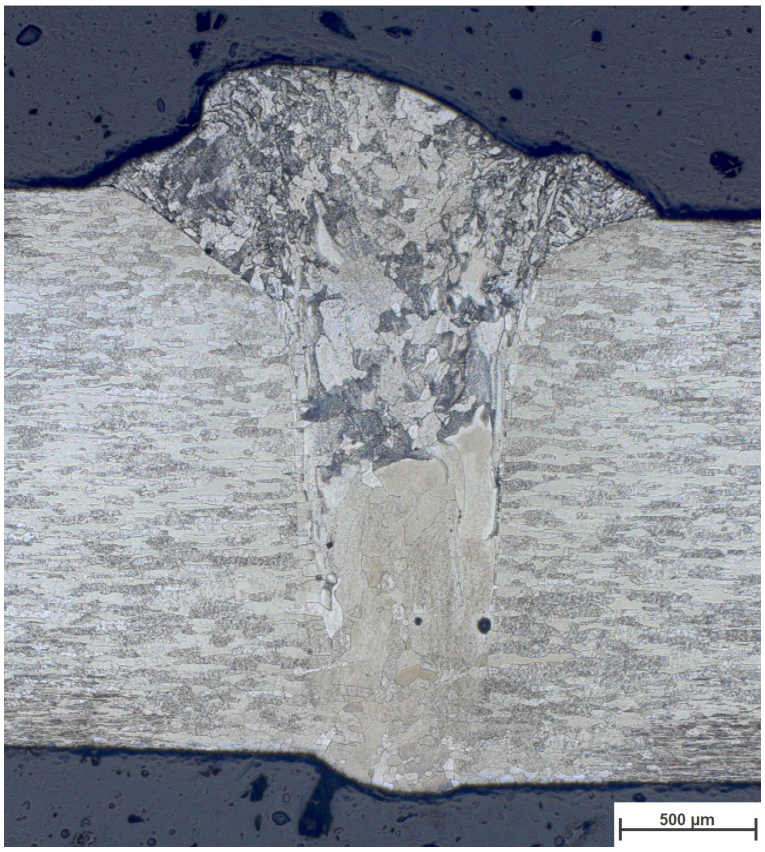

Figure 4.30: EB weld of 2 mm TZM with V filler. Mo–V solid solution is observed in the top weld region.

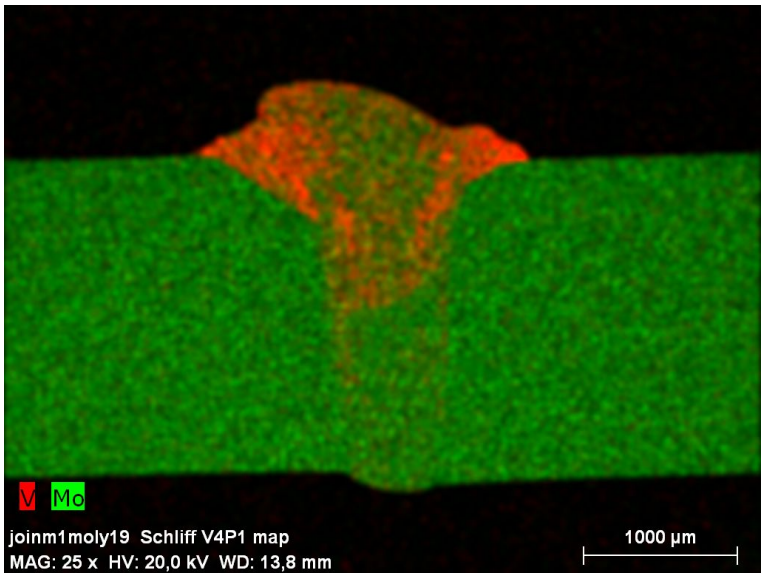

Figure 4.31: EDX map of 2 mm TZM with V filler: A V-concentration is observed in the top weld region.

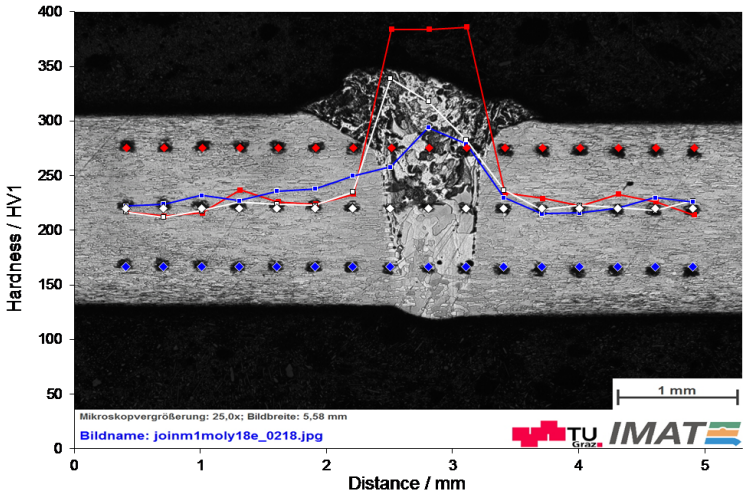

Figure 4.32: Hardness of the EB weld of 2 mm TZM with V filler: An increase of hardness is observed in the V-enriched regions

4.3.3 Electron beam welding of 2 mm TZM with VACTZM filler metal

VACTZM as filler metal proved to be more stable in the melt transfer from the wire into the weld pool than vanadium. Good results were achieved by direct deposition of the wire, with the best results exhibiting almost no pores. Table 4.5 lists the parameters of the best result of EBW of 2 mm TZM with VACTZM filler metal. Note that due to the direct insertion of the filler metal the beam oscillation amplitude (beam figure diameter) had to be set to 1.0 mm to ensure a stable melt transfer from the wire into the weld pool.

Cracks could be suppressed by cooling in vacuum, as previously described. Figure 4.33 shows the resulting hardness courses. It is observed that the values drop from 290 HV1 in the BM to approximately 220 HV1 in the HAZ and the FZ, similarly to the welds without filler metal.

Table 4.5: Welding parameters of 2 mm TZM sheets with filler metal VACTZM

Beam power	Welding speed	Deflection figure	Wire feed
20.7 mA	30 $^{mm}/_{s}$	Circle ∅1 mm	0.58 $^{m}/_{min}$

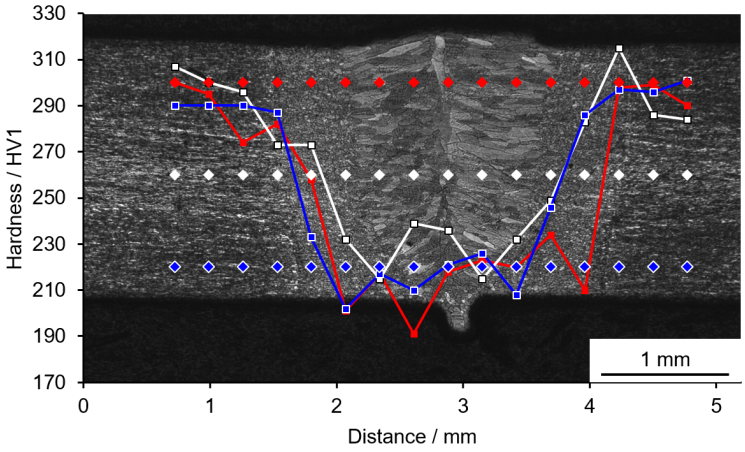

Figure 4.33: Hardness courses of a 2 mm TZM sheet EB welded with VACTZM filler metal. A hardness drop is observed in HAZ and FZ

4.3.4 Electron beam welding of 2 mm TZM with cored wire filler metal

The filler metal deposition was carried out by 18 mA beam power, 20 $^{mm}/_{s}$ welding speed, 1.2 $^{m}/_{min}$ wire feed, and concentric ellipses (3×2 mm in welding direction) as deflection figure. Table 4.6 lists the experiment numbers and their according welding parameters. Post-weld heat treatment was executed in all samples except V2P2.

Table 4.6: Welding parameters for welding 2 mm TZM with cored wire filler. The scanning frequency of the beam deflection figures was set to 1,000 Hz.

	Beam power	Welding speed	Deflection figure
V2P2	22 mA	30 $^{mm}/_{s}$	Circle ∅0.5 mm
V2P3	22 mA	30 $^{mm}/_{s}$	Circle ∅0.5 mm
V3P1[1]	2 × 22 mA	30 $^{mm}/_{s}$	Circle ∅0.5 mm
V3P2	35 mA	60 $^{mm}/_{s}$	Circle ∅0.5 mm
V3P3	20 mA	30 $^{mm}/_{s}$	Circle ∅0.5 mm

Although the porosity of the produced Mo cored wire was considerable (40–60%), the filler metal deposition showed no instabilities and the finished welds appeared smooth and regular both on the top side as well as on the bottom side.

4.3.4.1 Microstructure

All performed welds showed a regular and almost pore-free microstructure as figures 4.34 and 4.35 exemplary show. Excess material from the filler wire on the weld top surface is observed.

[1] Two welding passes with a 3 min cooling interval in between.

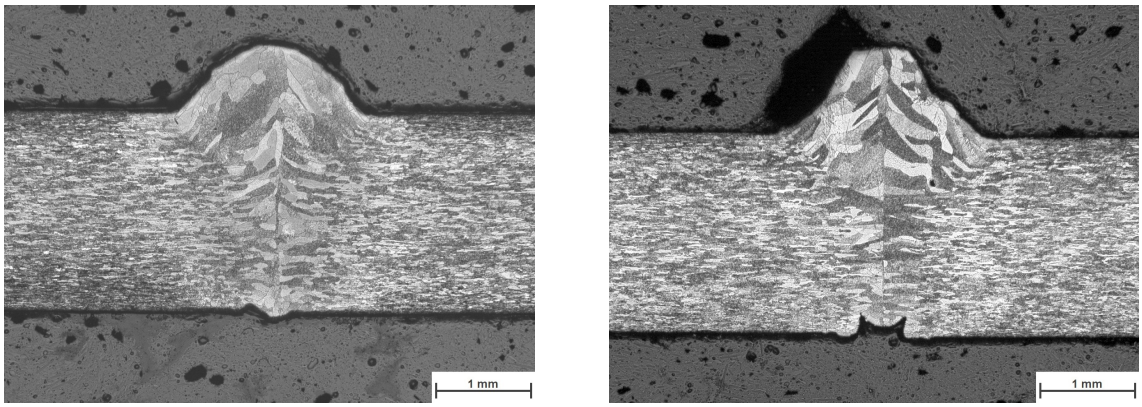

(a) (b)

Figure 4.34: Microsection of (a) V2P2 and (b) V3P2 EB welds of 2 mm TZM sheets with cored wire filler

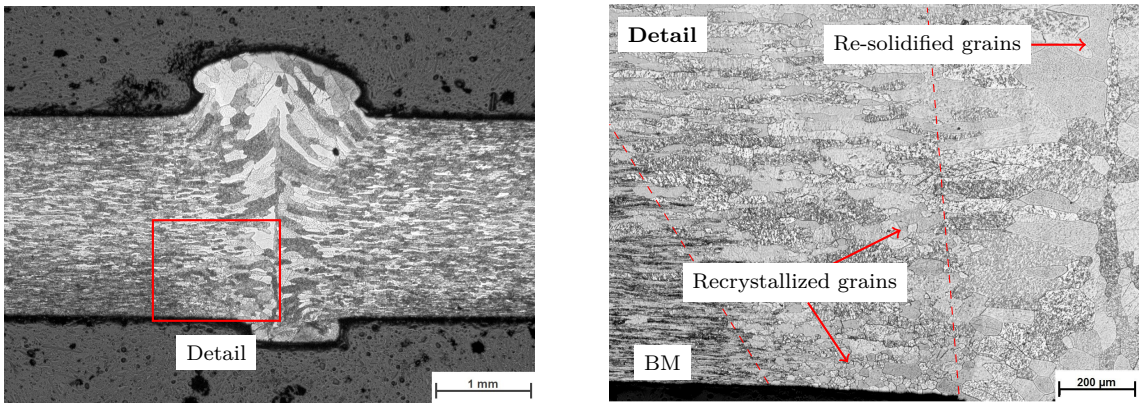

(a) (b)

Figure 4.35: V3P1 (a) Overview microsection and (b) detail to identify recrystallized regions of the HAZ

If figure 4.20 (page 88) is compared to figures 4.34 and 4.35, it is observed that the microstructure appeared different in the micrographs: In figures 4.35a and b it was almost impossible to visually determine the borders between BM and HAZ. The detail in figure 4.35b in higher resolution allowed a distinction between BM and the recrystallized HAZ. However, the border to the FZ is still difficult to determine and had to be assumed from the different grain size.

Figure 4.36 shows X-ray images of the different welds. Continuous porosity is observed along the edges of the weld beads.

Figure 4.37a shows an EDX spot scan of a particle in the base metal. The resulting spectrum revealed mostly Mo, but also Ti, suggesting that the particle is $(Mo,Ti)_xC_y$. Similar particles were neither observed in the HAZ nor in the FZ. A possible explanation is that because pure Mo was used as filler metal, the Ti of the sheets was diluted beyond a point where (Mo,Ti)-carbides are detectable by SEM, Ti has evaporated, or that all Ti is in solution.

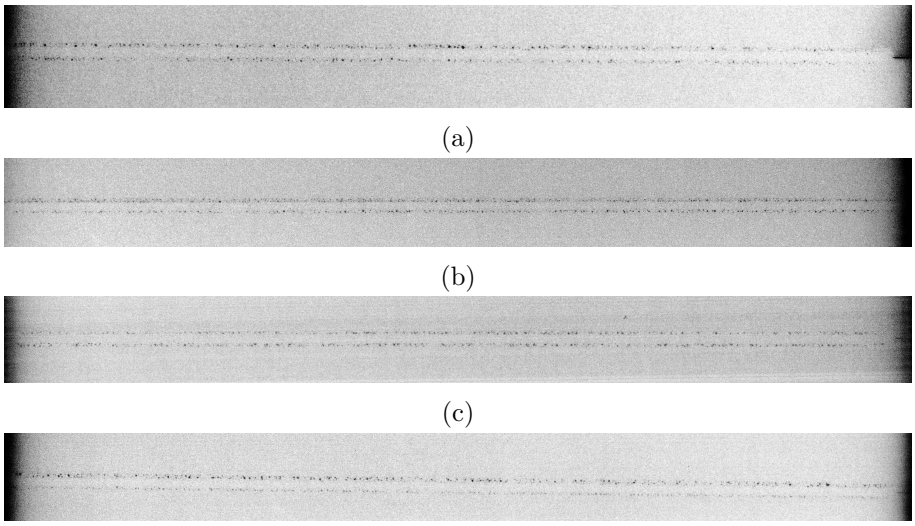

(a) (b) (c) (d)

Figure 4.36: X-ray images of EB welds of TZM with cored wire filler: (a) V2P3, (b) V3P1, (c) V3P2, and (d) V3P3. Continuous porosity is detected along the edges of the weld bead.

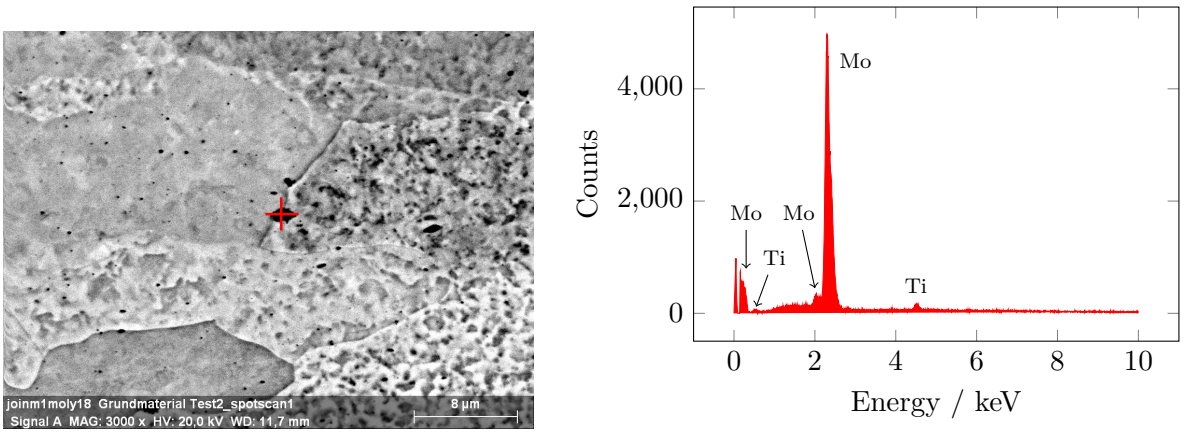

(a) (b)

Figure 4.37: (a) EDX spot scan in a particle observed by SEM and (b) EDX spectrum with Mo and Ti peaks visible

4.3.4.2 Hardness

The hardness evaluation revealed that the average hardnesses of BM, HAZ, and FZ only varied slightly, except V3P2 (35 mA, 60 $^{mm}/_{s}$) exhibited a slightly higher hardness in the FZ than in BM and HAZ (figure 4.38). The grain size of V3P2 appeared larger than of V2P2 (figure 4.34). This coherence was in accordance to the TZM butt welds without filler metal, which was that 1) larger grains occurred at higher beam power and 2) a faster welding speed resulted in higher hardness values.

Concerning the base metal hardness, it is observed that the base metal hardness of the TZM sheet batch used in the cored wire experiments was substantially lower than in the experiments without filler metal. The observed variation was between 220 HV1 (cored wire) and 290 HV1 (no

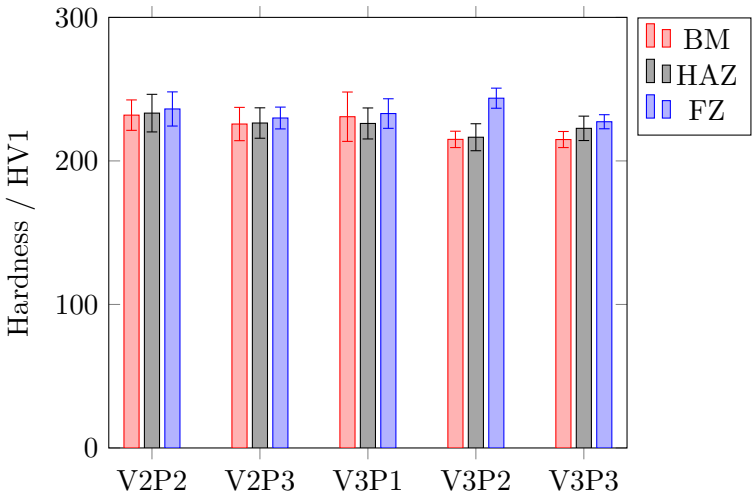

Figure 4.38: Hardness values after PWHT with standard deviations of base metal (BM), heat affected zone (HAZ), and fusion zone (FZ) of different 2 mm TZM sheet welds with cored wire filler

filler, V, VACTZM). These differences in batches are a result of the production process of PM TZM and according to *Plansee SE*, the hardness values may range from 220 to 320 HV1 [134].

4.3.4.3 Ductility and strength

Tensile tests and three-point bending tests were conducted of the samples welded with cored wire filler. The tensile and bending samples were extracted and the surface was ground flat to remove excess material and notches on the top and bottom side of the weld. Figure 4.39a shows the results of the tensile tests. It is observed that all investigated samples are below the reference value of 587.3 MPa of the tested fully recrystallized TZM base metal. The average values achieved

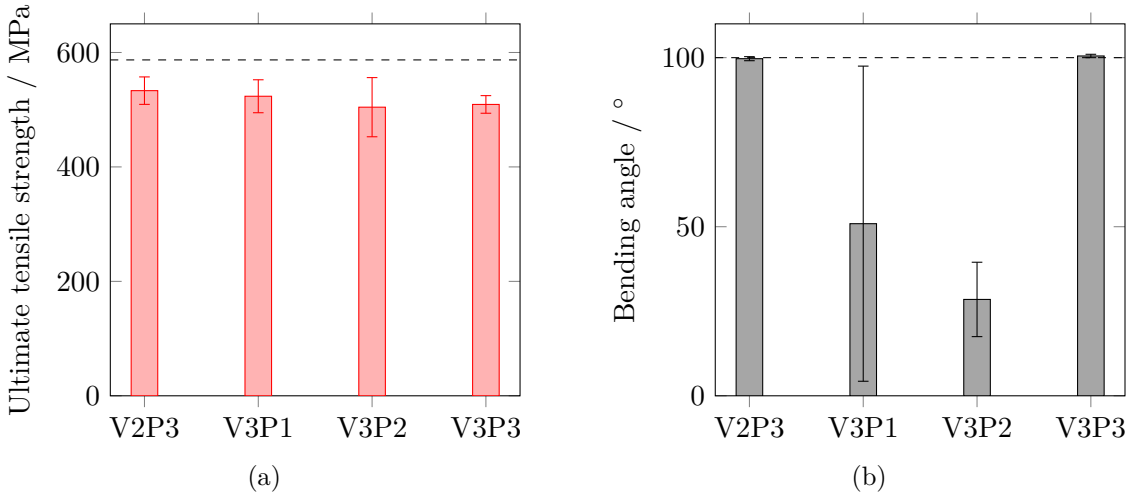

Figure 4.39: (a) Ultimate tensile stress values and (b) achieved three-point bending angles of different 2 mm TZM sheet welds with cored wire filler. The dashed lines represent the values of the fully recrystallized base metal reference.

between 86% (V3P2) and 91% (V2P3) of the reference. The fracture elongation was still poor and below 1.6% in all cases. However, as observed in figure 4.39b, three-point bending tests revealed that the resulting bending angles of V2P3 and V3P3 reached the reference of 100°. The bending samples of V3P1 exhibited anomalies, where either angles of 10–17° or 100° occurred.

To conclude, the desired bending ductility was met with cored wire filler welds at a welding speed of 30 $^{mm}/_{s}$ with beam currents of 20 and 22 mA. A second weld pass (V3P1) apparently caused irregularities in the weld, which resulted in a large spread of achieved bending angles in the different bending samples. Furthermore, an increased welding speed (V3P2) resulted in lower bending angles overall. It has to be noted that the base metal sheets used in the cored wire filler experiments yielded a base metal hardness on the lower end of the specified hardness range for TZM [12]. It is highly likely that the base metal condition plays an important role in the processability by welding.

4.3.5 Electron beam welding of 5 mm TZM

The up-scale from 2 mm to 5 mm TZM sheets was done by increasing the beam power accordingly. In trial butt welds it was found that at 43 mA full penetration is ensured, which is a factor of roughly 2.8 times the beam power of 2 mm fully penetrated butt welds. Experiments were carried out to elaborate the effect of a higher welding speed of 60 $^{mm}/_{s}$. To reach full penetration, the beam power was increased from 43 to 67 mA, which is +56% of beam power. The reason is that the keyhole requires a certain power to remain open and a doubling of the welding speed requires only a fraction of excess power.

Figure 4.40 shows the microsections of the two butt welds with (a) 30 $^{mm}/_{s}$ and (b) 60 $^{mm}/_{s}$ welding speed. In both images fine-grained FZ and HAZs are observed, although the higher welding speed resulted in a smaller grain size in the FZ and smaller widths of both FZ and HAZ.

Figure 4.41 shows the resulting averaged hardness courses of 30 $^{mm}/_{s}$ and 60 $^{mm}/_{s}$ with and

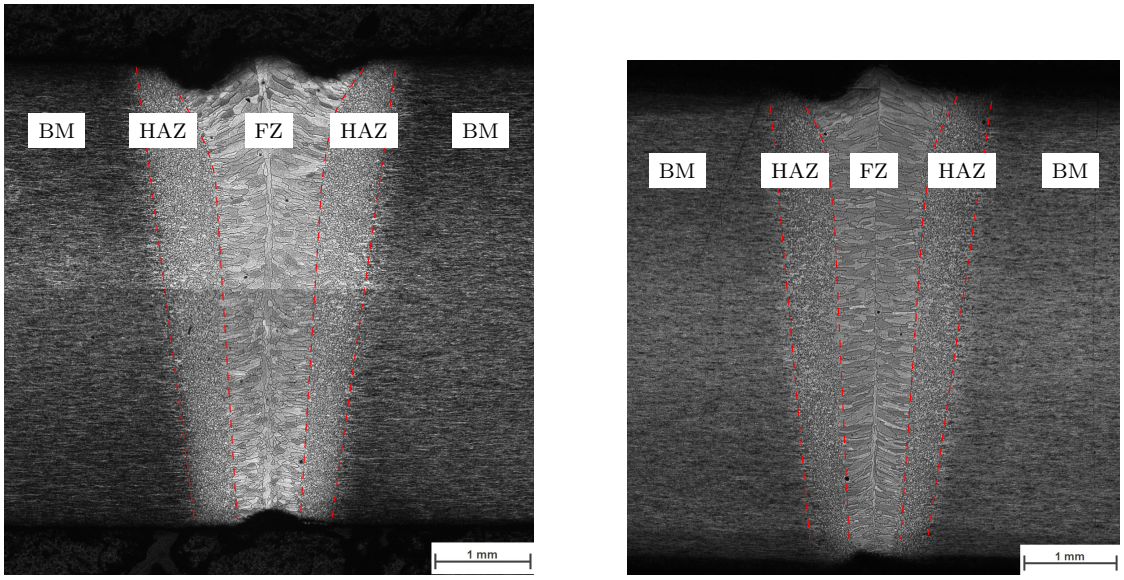

(a) (b)

Figure 4.40: EB butt welds of 5 mm TZM sheet metal welded with (a) 43 mA and 30 $^{mm}/_{s}$ and (b) 67 mA and 60 $^{mm}/_{s}$

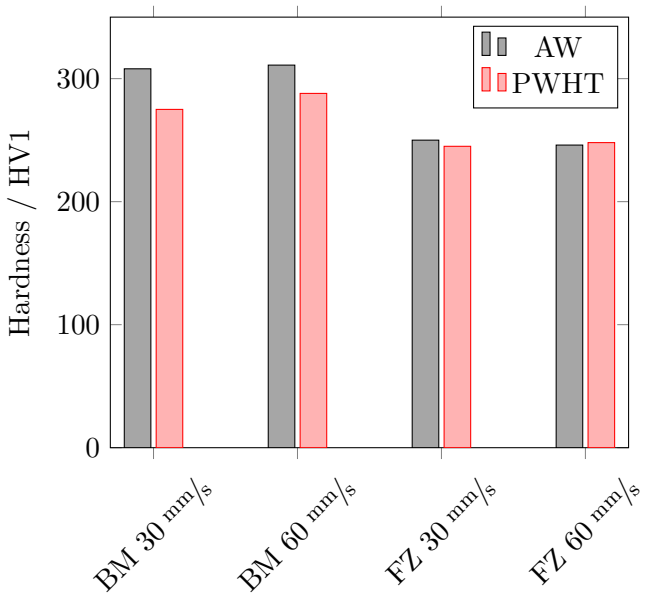

Figure 4.41: Comparison of averaged hardness courses of 5 mm TZM EB welds with different welding speeds and without and with post-weld heat treatment

without post-weld heat treatment. First, it is observed that a higher welding speed does not affect the resulting hardness. Second, the PWHT process reduced the HV1 values of the base metal slightly, but the HAZ and FZ remained unaffected. It was therefore concluded that the hardness values and as a consequence the UTS were not improved significantly by PWHT.

4.3.5.1 Filler metal

As mentioned before, a liquid metal bridge has to establish to ensure a stable EB welding with a wire filler metal. In a first attempt the solid wire was fed directly into the weld pool. The higher beam power resulted in a higher pressure of the vapor cavity, which exceeded the pressure the filler metal melt droplet could withstand. The wire was spattered upon contact with the beam or the vapor cavity. Figure 4.42 shows the resulting weld bead with a re-solidified droplet and substantial lack of fusion. Further, the spattering filler metal consumed a major amount of the beam power which meant that the remaining power was insufficient to fully penetrate the V-joint. It is observed that only roughly half of the depth was achieved and the V-preparation was still visible in the bottom half of the fusion interface.

It was therefore concluded that with a welding depth of 5 mm a single step weld was not feasible. The solution was to split the welding process into multiple steps: First, the filler metal should be deposited on top of the joint preparation, and second, the actual welding process should take place. Figure 4.43a shows a microsection of a filler metal deposition on plate, with the re-solidified filler metal exhibiting large grains and an established HAZ in the proximity of the deposition. In figure 4.43b the filler deposition is observed on top of the standard V-joint preparation, over which the actual welding process takes place. To ensure a better dilution of the filler metal over the full 5 mm depth of the weld two identical welding cycles were carried out successively. The final welding procedure is listed in table 4.7. For welding the beam current had to be increased from 43 mA to 54 mA to penetrate and dilute the deposited filler metal.

Figure 4.44 shows the microsection of the resulting weld. Excess material and pores are present in the top region, but cracks were not visible.

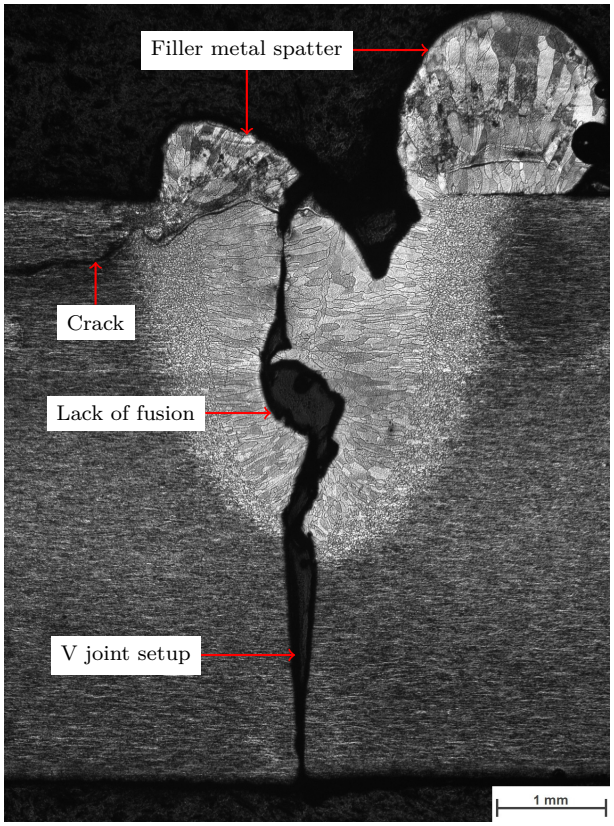

Figure 4.42: EB weld of 5 mm TZM with filler metal inserted into the full penetration beam. The V joint setup is still visible due to a lack of fusion and further, spatter is observed on the surface of the TZM sheets.

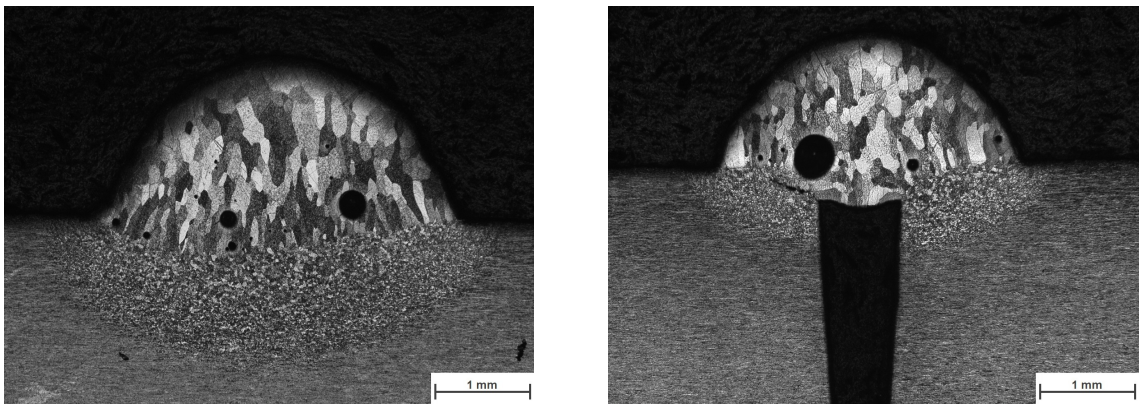

(a) (b)

Figure 4.43: Filler metal deposit (a) on plate and (b) on top of the V joint setup

Finally, one trial weld with cored wire was conducted in 5 mm TZM. The same welding sequence as listed in table 4.7 was executed, only the beam current was reduced to 50 mA, because first, the cored wire was porous and therefore less material was deposited at the same wire feed rate. Second, the experiments with VACTZM filler metal suggested that the beam power could be reduced and still obtain full penetration.

Table 4.7: Welding procedure for a three step welding of 5 mm TZM with filler metal VACTZM. The scanning frequency of the deflection figures was set to 1,000 Hz.

Step	Beam power	Welding speed	Deflection figure	Wire feed
1. Deposition	20 mA	10 $^{mm}/_{s}$	Concentric circles ∅4 mm	2 $^{m}/_{min}$
2. Welding	54 mA	30 $^{mm}/_{s}$	Circle ∅0.5 mm	–
3. Welding	54 mA	30 $^{mm}/_{s}$	Circle ∅0.5 mm	–

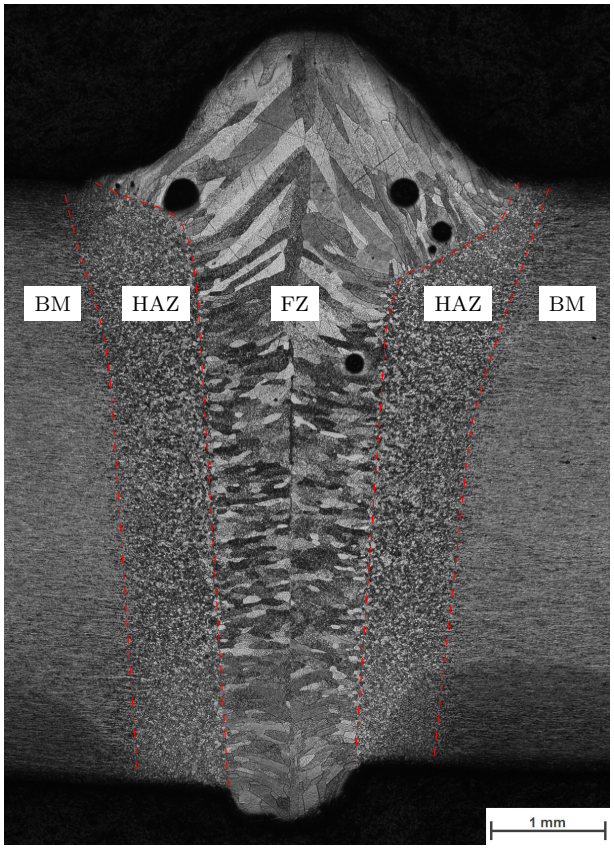

Figure 4.44: 3-step EBW of 5 mm TZM sheet metal with VACTZM filler.

Figure 4.45 shows the hardness obtained from the experiment. Again, the values drop from the BM to approximately 230 HV1 in HAZ and FZ. Compared to the butt welds without filler metal the hardness is therefore slightly lower with cored wire filler.

To elaborate a more productive way and combine the deposition and welding steps, a combined beam figure was designed (see figure 4.15 on page 84). Here, the deposition of filler metal is followed by two consecutive welding steps with full penetration. The distance between the three beam instances was 10 mm, the relative beam currents were 50 mA for deposition, 67 mA, and 63 mA for welding, respectively. Figure 4.46 shows a live image of the process during welding. The filler metal as well as the two following keyholes are observed.

As a result of the combined process, the overall beam power adds up to 180 mA, which further leads to a total energy input per length of 900 $^{J}/_{mm}$ at 150 kW acceleration voltage. This excessive energy input lead to severe residual stresses and resulted in spontaneous, almost explosive cracking of the sheets during unclamping. Figure 4.47 shows that cracks initiated at

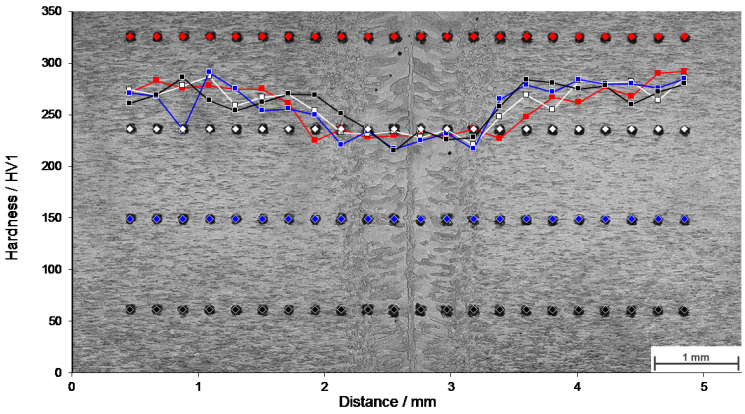

Figure 4.45: EB weld of 5 mm TZM with cored wire filler

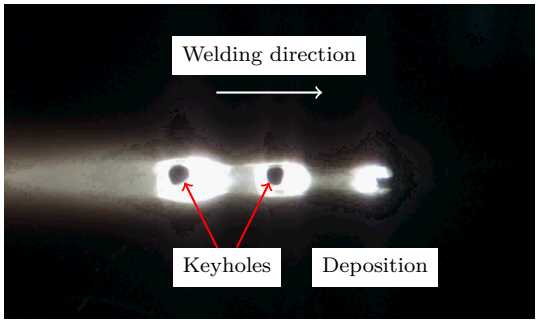

Figure 4.46: Live image of the combined welding process: The filler metal insertion and the two weld pools are observed.

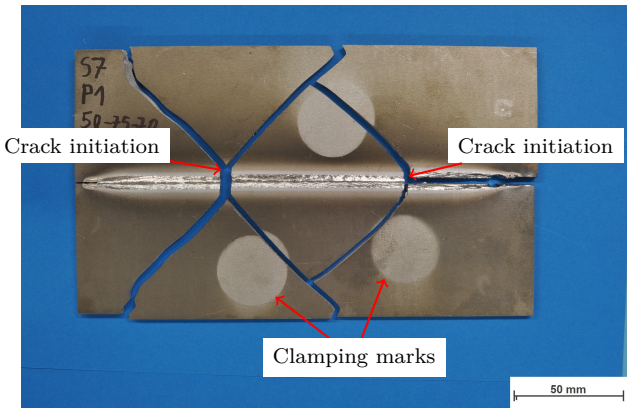

Figure 4.47: Cracked 5 mm TZM sample of a combined process after unclamping: Cracks initiated at the weld zone and propagated in 45° towards the sheet edges.

multiple positions and propagated in 45° all the way through the sheets. The micrograph of the weld in figure 4.48 shows that the high energy input resulted in excessive grain growth in the FZ as well as a large recrystallized HAZ with a width of 2.2 mm, which is beyond the margins of the image in figure 4.48.

To make a combined process feasible, the total beam power has to be reduced drastically. One

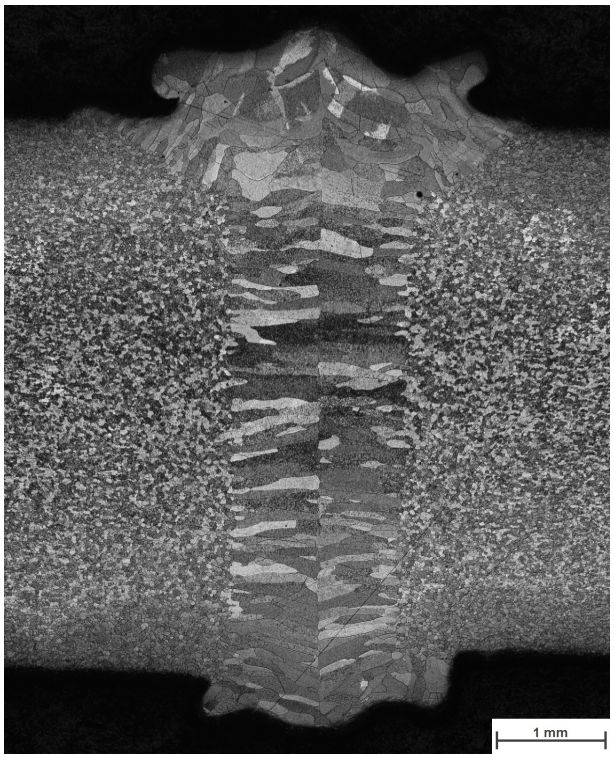

Figure 4.48: Micrograph of a 5 mm TZM sheet welded with VACTZM filler metal in a combined EBW process. Excessive grain growth in the FZ and a large HAZ are observed.

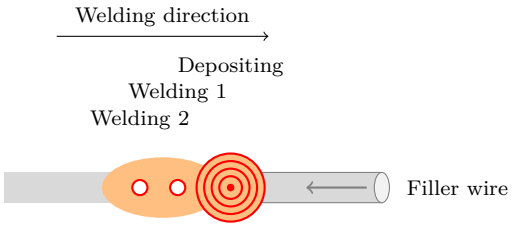

Figure 4.49: Proposed improvement of a combined beam figure: The welding steps should be closer together to enable welding in a larger but single weld pool.

problem with the current configuration was that the weld pool solidified after the respective welding steps. Therefore, the beam of the welding steps needed to re-melt the metal again by additional beam power. A possibility could be to reduce the distances between the weld pools in order to keep the two keyholes within one single melt pool. Figure 4.49 depicts the principle.

4.3.6 Summary

In the course of the project different EBW experiments were carried out:

- 2 mm sheets without filler metal
- 2 mm sheets with vanadium filler metal
- 2 mm sheets with vacuum arc cast TZM filler metal
- 2 mm sheets with molybdenum cored wire filler metal

- 5 mm sheets without filler metal
- 5 mm sheets with vacuum arc cast TZM filler metal
- 5 mm sheets with molybdenum cored wire filler metal

With careful parameter selection in EB butt welding of TZM it is possible to influence the hardness and the UTS to some extent: In the configuration of 2 mm, hardness values and UTS values correlated to each other, meaning that a higher hardness value also meant a higher UTS value. The grain size of the FZ was mostly affected by the beam power while the welding speed was less important. The achieved UTS was most affected by the welding speed and the fracture occurred in the FZ in every experiment. Therefore, the grain size of the FZ did not determine the tensile performance. This is also backed by the fact that transgranular fracture rather than intergranular fracture occurred at the best tensile strengths, which means that grain boundary cohesion is not the limiting factor in the tensile performance. Following the argument of Scheiber et al. [37], a faster cooling rate and thus faster welding speed would reduce the oxygen concentration on the grain boundaries, which may have changed the fracture mode.

In butt welds without filler metal the best results concerning hardness and UTS were achieved with a welding speed of 30 $^{mm}/_{s}$, regardless of beam power. A lower beam power, however, resulted in smaller grains in the FZ and the HAZ. In general, a smaller grain size is preferred, because the strength impairing elements and precipitates are more spread if the total length of grain boundary is higher.

EBW of TZM sheets with vanadium filler metal proved to be problematic. The underlying idea to counteract the observed hardness decrease in the fusion zone by producing a solid solution strengthened fusion zone was accompanied by a severe issue with inferior ductility and high susceptibility to cracks. First, the filler metal insertion or deposition, owed to the different melting temperatures and vapor pressures of TZM and V resulted in an unstable process or directly induced cracks. Second, the increase in hardness of the solid solution crystal also increased the brittleness of the fusion zone to an unacceptable extent. Therefore it has to be concluded that vanadium is unsuitable as a filler metal for EBW of TZM.

Vacuum arc cast TZM (VACTZM) filler metal was well processible due to the quasi-similar filler metal. However, VACTZM did not increase the properties of the welds notably. Nevertheless, it was shown that in EBW a stable filler metal insertion was possible by means of a filler wire.

The novel pure Mo cored wire filler proved to be well processible by means of EBW. A stable weld bead established and no macroscopic welding defects were detected. The hardness of the base metal was sustained throughout HAZ and FZ; the hardness of the used base metal batch, however, was lower compared to previous experiments. It can be assumed that the condition of the base metal majorly contributes to the resulting ductility of TZM welds, as other authors have suggested as well [47]. Tensile tests revealed a low fracture elongation with slightly reduced tensile strengths compared to fully recrystallized base metal, but three point bending tests successfully exhibited 100° bending angle of a single pass weld at 30 $^{mm}/_{s}$ and 20–22 mA.

In the current configuration it is assumed that a seam preparation with parallel edges and a space of 0.2 mm are sufficient. Experiments with V-shaped seam preparation and vanadium filler metal exhibited also improper dilution and did not improve the dilution of the filler metal with the base metal. The costlier V-seam preparation seems to be advantageous only if a very small wire diameter (e.g. ∅0.2 mm) had been used and the filler wire could have been inserted directly into the groove. Although a better dilution is expected if a second weld pass is conducted, the experiment in 2 mm TZM with cored wire filler showed inferior bending ductility than the single pass welds.

5 Summary and Conclusion

This work concerns the welding behavior of molybdenum and its alloys. Naturally, being a refractory metal, molybdenum possesses a number of unique properties like high melting point and good high temperature strength, among others, which sets it apart from more common materials like steels or aluminum alloys. Therefore, the welding behavior differs substantially as well. In literature it was established that mainly grain coarsening and recrystallization lead to an intrinsic embrittlement of the welds which limited the technical applicability of welded Mo-products [1, 12, 14]. The goal of this project was to deepen the knowledge about the welding behavior, investigate process parameter interactions, and identify process improvements for different welding technologies.

The thesis is separated in three main parts: First, the general properties and behavior of molybdenum and its alloys, containing an experimental investigation the flow curves of Mo. Second the welding technology of friction welding and its application for joining Mo and TZM alloy. A comprehensive study in tubular and rod format Mo and TZM samples was conducted and discussed. Third and last, the fusion welding by the means of electron beam welding of TZM. Here, the main focus laid on the investigation and elaboration of possible and novel filler metals to improve the mechanical properties of the finished welds.

5.1 Molybdenum

To characterize the hot deformation behavior of molybdenum, isothermal compression experiments in a *Gleeble 3800* simulator were successfully carried out. The investigated samples of $\varnothing 6 \times 12\,\mathrm{mm}$ pure Mo rod material were investigated in a temperature range from 200 to 1,700°C and at strain rates of 0.01, 0.1, 1, and $10\,\mathrm{s}^{-1}$until a true strain of 1. The findings can be summarized as follows:

1. With rising temperature, the flow stress decreased accordingly.
2. At the same temperature but at different strain rates, Mo showed a higher flow stress at higher strain rates. The observed strain rate sensitivity increased with increasing temperature.
3. An increase of stress with increasing strain (strain or work hardening) was observed at lower temperatures up to 1,300°C. A transition towards steady-state behavior occurred in the range between 750°C / $0.01\,\mathrm{s}^{-1}$ and 1,300°C / $10\,\mathrm{s}^{-1}$. At high temperatures and strain rates of 0.01–$0.1\,\mathrm{s}^{-1}$ a decrease of flow stress was observed (strain or work softening)
4. A transition of material behavior occurred between 900 and 1,100°C. At lower temperatures, the flow curves showed a distinct local maximum with a subsequent valley in the interval of $\varepsilon = [0, 0.2]$. This was accounted to the circumstance that the 2 min temperature soaking before the compression experiments lead to recrystallization of the samples above 1,000°C, which is the quoted recrystallization temperature of Mo.

Coefficients for a Zerilli–Armstrong flow stress model were determined to estimate the flow stress for temperatures until the melting point. It was shown that the model can depict the

flow stress with acceptable accuracy in a wide temperature range. Nevertheless, certain effects like the initial peaks in flow stress as well as steady-state and strain softening behavior could not be depicted by the Z–A model. Further, since the experiments were limited to 1,700°C, the extrapolated flow curves are to be interpreted as rough estimations.

5.2 Friction welding

Rotary friction welding (RFW) is a well established solid state joining process in industrial production. The advantage of joining molybdenum and TZM by RFW is that typical welding defects of fusion welding are avoided since the base metal never reaches the melting temperature. Further, strong plastic deformation in the fusing volume prevents detrimental grain coarsening and the associated embrittlement. Experiments were carried out in ∅130 × 10 mm Mo tube format as well as in laboratory scale ∅12 and ∅9 mm rod material of Mo and TZM, respectively. As it turned out, the plasticization behavior of Mo and TZM differed strongly from that of low carbon steel. Strong plasticization occurred and a much smaller process parameter window was feasible. The following list compiles the main understandings drawn from the experiments:

1. In the tube format experiments a motor overload occurred. The 150 kW drive was apparently insufficient to cope with the deforming Mo tubes. The result was a decelerating spindle during the welding process until a full halt.

2. Strong plasticization and for known RFW processes uncommonly high upset rates were observed, accounting to values of 7.0 $^{mm}/_{s}$, which caused the vast drive power demand of the deforming tubes.

3. Different welding speeds showed no improvements of process stability, as well as a preheating of the tubes in a furnace did not improve the welding behavior and proved to be little reproducible due to the manual clamping procedure.

4. Despite the unstable process, the cross sections showed a fine-grained microstructure. Some lack of bonding was detected by ultrasonic testing. Hardness measurements across the weld areas showed a sustained hardness of the base metal throughout the weld.

5. The rod format experiments allowed an investigation of the influences of the RF welding behavior of Mo and TZM due to a better tunability of the FSW machine's input parameters.

6. Due to brittle failure of samples during the friction phase in preliminary experiments, an in-situ pre-heating process by friction at low axial pressures was developed, which enabled to exceed the DBTT of the samples directly prior to the actual RFW process.

7. Sudden and intensive plasticization occurred in all experiments and appeared to be an intrinsic behavior of Mo and TZM, which could only be slightly influenced by process parameters.

8. Successful and reproducible welds of Mo were achieved only with a fast spindle deceleration and an adjusted, soft transition from friction pressure to forge pressure. Further, the spindle deceleration was initiated simultaneously with the increase of axial pressure, a so-called "forging into the turning spindle."

9. A slight variation of welding speed lead to large differences in the resulting total upsets. It was shown that the difference of upsets occurred in the transition phase from the friction stage to the forge stage, where the maximum upset rates varied largely.

10. In the TZM experiments, reproducible variations of the process parameters friction pressure, forge pressure, forge pressure gradient, and deceleration rate were possible. The main influence of welding speed on upset—similar to Mo—was observed as well.

11. The microstructure of both Mo and TZM was sound in most successful experiments, while a minimum upset of at least 4 mm appeared to be necessary to expel all surface contaminations into the flash. The hardness maps revealed an even distribution in Mo and a slight increase in the contact zone in TZM.

The strong plasticization behavior and sudden upsetting was the main issue of Mo and TZM in RFW. One reason is the high thermal diffusivity of Mo compared to steel; a low specific heat capacity and a high thermal conductivity results in a large volume exceeding the shear strength and contributing to the deformation during the process. This resulted in a high power demand and only a short time frame for the transition from the friction phase into the forge phase. To design an appropriate welding process for Mo and TZM, these circumstances have to be taken into account.

The simulation of the RFW process, on the other hand, proved to be especially challenging, since the deformation behavior of Mo close to the melting temperature was unknown and could only be estimated by extrapolating the flow stress. Further, in absence of an appropriate heat generation model, the heat input was derived from experimentally recorded values. Further simplifications implied a 2.5d model disregarding rotational shear deformation and stress. The establishing temperature field showed good agreement, although the deformation contour and calculated axial force deviated.

5.3 Fusion welding

Electron beam welding is a high power beam welding process with an energy density several magnitudes above conventional arc welding processes. Therefore, the energy input during welding TZM sheets could be minimized. Experiments in 2 mm and 5 mm TZM sheets were conducted, starting with a parameter optimization of butt welds without filler metal. Since the melting and re-solidification in a fusion welding process, inevitably leads to inferior mechanical properties in Mo and TZM [1, 14, 123], an approach was to investigate and develop suitable filler metals for TZM. The following was revealed:

1. With a parameter optimization in EBW the property impairing effects can be minimized in TZM butt welds. It was found that a high welding speed with low beam power resulted in smaller grains in the fusion zone, a smaller and more fine-grained heat affected zone and better tensile properties than at low welding speeds and/or high beam powers.

2. The hardness of the FZ and HAZ dropped compared to the as-received base metal. Nevertheless, the best welds achieved tensile strengths above fully recrystallized TZM, which was the benchmark for the EB welds. However, an almost full loss of ductility was observed, where the specimens failed in a brittle manner at neglectable fracture elongation.

3. Based on the process parameters for TZM butt welds, a filler metal insertion by a wire feed into the weld pool was introduced and facilitated.

a) A direct deposition of the filler metal was possible only in 2 mm sheet welds. In 5 mm sheets the higher necessary beam power for full penetration destabilized the filler metal transition into the weld pool.

b) A multiple-step process with prior filler metal deposition onto the seam preparation and subsequent welding was developed to minimize the beam forces on the filler metal during transition.

4. Vanadium was chosen as a filler metal due to its full solubility in Mo and high strength of the Mo–V solid solution crystal. An assessment of welds with V filler showed that the hardness of the base metal could be sustained, but it increased the tendency to brittle failure even further. Cracks occurred even during welding and could only partly be suppressed.

5. Vacuum arc cast (VAC) TZM was tested as filler metal, because the VAC process results in even lower residual oxygen contents than powder metallurgically produced TZM. This potential advantage, however, proved to be unfounded, as no improvement in ductility was observed.

6. A novel cored wire filler was developed in the course of this project, composed of a pure Mo envelope and a pure Mo powder core.

   a) The microsections showed a sound microstructure and the hardness measurements revealed an almost constant hardness from the base metal through the HAZ into the FZ. Continuous porosity was observed by X-ray imaging along the edges of the weld bead.

   b) Bending tests showed promising results of welds that achieved the required 100° bending angle. The nature of this profound increase in ductility, however, was not identified.

   c) The base metal hardness of the TZM sheets used in the welds with cored wire was much lower than in the batch of TZM sheets in the butt welds and solid wire experiments. Therefore, it was concluded that the base metal condition most likely plays an important role in the resulting weld quality.

   d) To improve the weldiability of TZM sheets, it may be suitable to investigate the influence of the base metal condition further and possibly to narrow down the specification ranges. Especially the specified hardness range from 220–320 HV1 seems too large for reproducible welding.

EBW is a welding technology with vast possibilities for welding molybdenum, molybdenum alloys, and refractory metals in general. Especially the approach by a custom filler metal bears enormous potential.

5.4 Outlook

In the present work, advances in the weldability of molybdenum and TZM were pursued. Apart from the results and findings, limitations of the understanding as well as potentials for further research were encountered:

Hot deformation Concerning the hot deformation behavior of molybdenum, compression tests were only executed up to 1,700°C. To further the characterization, experiments up to the melting

temperature of 2,620°C are required to assess molybdenum's hot deformation behavior comprehensively. In respect to friction welding, torsion deformation tests could also aid the understanding and show effects in rotary shear deformation. The modeling of flow curves should be approached on a more physically based level to include effects like recrystallization, recovery, and the connected work hardening and softening.

Rotary friction welding The characterized friction welding behavior of molybdenum pointed out key issues, mainly the fast upsetting and the high power demand. To confirm the proposed up-scale of the parameters, RFW of larger cross sections should be validated experimentally. The FSW machine at the institute has limited capacity for RFW processes, therefore experiments should be carried out on suitable and state-of-the-art friction welding machines. Then, a further investigation of process parameters and the underlying physics of the process is possible.

Simulation of RFW The simulation of RFW in its current setup lacks the ability to depict the welding process reliably. It contains several inconsistencies, above all a proper model for the heat generation. Given a reliable flow stress and a heat generation model as demonstrated in literature [101], the simulation may yield reasonable results which could enable a prediction of the welding behavior to some extent.

Electron beam welding The benchmark for EB-welded TZM was fully recrystallized base metal. Although it was shown that the resulting properties of the weld can be improved by suitable process parameters, they still missed their desired goal. Custom alloying of the weld could solve the issues metallurgically. First experiments with vanadium and vacuum arc cast TZM filler wire showed no improvement of the weld properties. However, an investigation of different conditions of the TZM base metal is suggested to determine the influence of the base metal on weldability.

Molybdenum cored wire filler metal Finally, the newly developed cored wire bears an enormous potential. Easily adaptable core compositions enable comprehensive experiments with selected additions of alloying elements to improve the ductility and the mechanical properties of the fusion zone. Given the conclusions in literature, carbon [31], boron [34], titanium [29], or zirconium [126] are the most evident elements to enhance the welding results.

Bibliography

[1] E. M. Savitskii and G. S. Burkhanov. *Physical Metallurgy of Refractory Metals and Alloys.* Springer US, Boston, MA, 1970.

[2] David Rowe. Heat Treating / Thermal Equipment: Refractory Metals. *Heat treating progress*, pages 56–60, December 2003.

[3] John A. Shields. Applications of Molybdenum Metal and its Alloys. 2013.

[4] Arnold Holleman and Egon Wiberg. *Lehrbuch der Anorganischen Chemie.* Berlin, 102nd edition, 2007.

[5] William D. Callister. *Fundamentals of Materials Science and Engineering.* John Wiley & Sons, 2001.

[6] M. S. Leitman, B. N. Nikonov, and V. V. Tregubenko. Refractory metals for alloying: Molybdenum. *Steel in Translation*, 37(12):1024–1027, dec 2007.

[7] Andrzej Ambroziak. Friction welding of molybdenum to molybdenum and to other metals. *International Journal of Refractory Metals and Hard Materials*, 29(4):462–469, jul 2011.

[8] Geoffrey W. Meetham and Marcel H. Van de Voorde. *Materials for High Temperature Engineering Applications.* Engineering Materials. Springer Berlin Heidelberg, Berlin, Heidelberg, 2000.

[9] *Molybdenum for Nuclear Energy Applications: a Perspective.* Climax Molybdenum Company, New York, NY, 1965.

[10] W. Behr and U. Reisgen. Innovatives Elektronenstrahlschweißen hochschmelzender Metalle. *Materialwissenschaft und Werkstofftechnik*, 38(7):504–509, jul 2007.

[11] Nicole Kinsman. Molybdenum metal coatings punch above their weight. *MolyReview 2/2014*, 2014.

[12] Plansee SE. *Molybdän Werkstoffeigenschaften und Anwendungen*, 2013.

[13] M. K. Miller, E. A. Kenik, M. S. Mousa, K. F. Russell, and A. J. Bryhan. Improvement in the ductility of molybdenum alloys due to grain boundary segregation. *Scripta materialia*, 46(2002):299–303, 2002.

[14] B. Tabernig and N. Reheis. Joining of molybdenum and its application. *International Journal of Refractory Metals and Hard Materials*, 28(6):728–733, nov 2010.

[15] Norbert Enzinger. FFG Projektantrag metal JOINing, 2014.

[16] Daniel de Pretis. *Rotational Friction Welding of Titanium-Zirconium-Molybdenum (TZM).* Master's thesis, Graz University of Technology, 2014.

[17] J. J. Wang, Y. Li, and D. Zheng. Progress of research on welding for molybdenum alloys. *High Temperature Materials and Processes*, 33(3):193–200, jan 2014.

[18] W. Martienssen and H. Warlimont. *Springer Handbook of Condensed Matter and Materials Data*. Springer Berlin Heidelberg, 2005.

[19] Sophie Primig. *Recovery and Recrystallization Behavior of Technically Pure Molybdenum*. Doctoral thesis, Montanuniversität Leoben, 2012.

[20] A. J. Bryhan. Joining of Mo Base Metal and Factors Which Influence Ductility. *Welding Research Council Bulletin*, 312:1–21, 1986.

[21] Fathi Habashi. *Handbook of Extractive Metallurgy*, volume III. 1997.

[22] S. Primig, H. Leitner, H. Clemens, A. Lorich, W Knabl, and R. Stickler. On the Recrystallization Behavior of Technically Pure Molybdenum. *International Journal of Refractory Metals and Hard Materials*, 1:1–9, 2009.

[23] B. Pegel. Stacking Faults on {110} Planes in the B.C.C. Lattice. *Physica Status Solidi (B)*, 28(2):603–609, 1968.

[24] Y. D. Vishnyakov. Stacking faults in the crystal structure. *Metallurgiya, Moscow*, page 127, 1970.

[25] J. S. Hirschhorn. Stacking faults in the refractory metals and alloys — A review. *Journal of the Less Common Metals*, 5(6):493–509, dec 1963.

[26] J. B. Brosse, R. Fillit, and M. Biscondi. Intrinsic intergranular brittleness of molybdenum. *Scripta Metallurgica*, 15:619–923, 1981.

[27] D. F. Stein. The effect of orientation and impurities on the mechanical properties of molybdenum single crystals. *Canadian Journal of Physics*, 45(2):1063–1074, feb 1967.

[28] James H. Bechtold and Howard Scott. Mechanical Properties of Arc-Cast and Powder Metallurgy Molybdenum. *Journal of The Electrochemical Society*, 98(12):495, 1951.

[29] T. Mrotzek, A. Hoffmann, and U. Martin. Hardening mechanisms and recrystallization behaviour of several molybdenum alloys. *International Journal of Refractory Metals and Hard Materials*, 24(4):298–305, 2006.

[30] A. Kumar and B. L. Eyre. Grain Boundary Segregation and Intergranular Fracture in Molybdenum. *Proceedings of the Royal Society of London. Series A, Mathematical and Physical Sciences.*, 370:431–458, 1980.

[31] Fumio Morito. Tensile properties and microstructures of electron beam welded molybdenum and TZM. *Journal of the Less-Common Metals*, 146:337–346, 1989.

[32] T. Mrotzek, U. Martin, and A. Hoffmann. High temperature deformation behavior of the molybdenum alloy TZM. *Journal of Physics: Conference Series*, 240, 2010.

[33] M. K. Miller and A. J. Bryhan. Effect of Zr, B and C additions on the ductility of molybdenum. *Materials Science and Engineering A*, 327(1):80–83, 2002.

[34] D. Scheiber, R. Pippan, P. Puschnig, and L. Romaner. Ab initio search for cohesion-enhancing impurity elements at grain boundaries in molybdenum and tungsten. *Modelling and Simulation in Materials Science and Engineering*, 24(8):1–12, 2016.

[35] Rebecca Janisch and Christian Elsässer. Segregated light elements at grain boundaries in niobium and molybdenum. *Physical Review B - Condensed Matter and Materials Physics*, 67(22):1–11, 2003.

[36] K. Leitner, D. Scheiber, S. Jakob, S. Primig, H. Clemens, E. Povoden-Karadeniz, and L. Romaner. How grain boundary chemistry controls the fracture mode of molybdenum. *Materials and Design*, 142:36–43, 2018.

[37] D. Scheiber, L. Romaner, F. D. Fischer, and J. Svoboda. Kinetics of grain boundary segregation in multicomponent systems – The example of a Mo-C-B-O system. *Scripta Materialia*, 150:110–114, 2018.

[38] A. S. Drachinskiy, A. V. Krainikov, and V. N. Slyunyaev. Interrelation of Impurity Enrichment of Grain Boundaries and the Cold-Shortness Point During Annealing of Molybdenum. *Phys. Met. Metall.*, 66(3):111–119, 1988.

[39] E. Z. Silva, H. Kestler, and H. R. Z. Sandim. Particle-stimulated nucleation of recrystallization in the hot-deformed molybdenum alloy MZ-17. *International Journal of Refractory Metals and Hard Materials*, 73:74–78, jun 2018.

[40] O. Engler, X. W. Kong, and P. Yang. Influence of particle stimulated nucleation on the recrystallization textures in cold deformed Al-alloys Part I—Experimental observations. *Scripta Materialia*, 37(11):1665–1674, dec 1997.

[41] R. P. de Siqueira, H. R. Zschommler Sandim, and D. Raabe. Particle Stimulated Nucleation in Coarse-Grained Ferritic Stainless Steel. *Metallurgical and Materials Transactions A*, 44(1):469–478, jan 2013.

[42] S. P. Samoilov and A. O. Cherniavsky. Work Softening and Low Cycle Fatigue of Molybdenum Alloy under Force-Controlled Loading and Elevated Temperatures. *Materials Science Forum*, 870:219–225, sep 2016.

[43] A. Chaudhuri, A. Sarkar, and S. Suwas. Investigation of stress-strain response, microstructure and texture of hot deformed pure molybdenum. *International Journal of Refractory Metals and Hard Materials*, 73:168–182, 2018.

[44] J. M. Dickinson and L. S. Richardson. The Constitution of Rhenium-Molybdenum Alloys. *Transactions of the American Society for Metals*, 51:1055–1066, 1959.

[45] L. Brewer and R. H. Lamoreaux. Molybdenum: Physico-Chemical Properties of Its Compounds and Alloys. *Atomic Energy Review*, (Special Issue No. 7, Part II):244–249, 1980.

[46] P. Franke and D. Neuschütz. Mo-V (Molybdenum - Vanadium). In *Binary Systems. Part 5: Binary Systems Supplement 1*, chapter 2, pages 1–4. Springer Berlin Heidelberg, Berlin, Heidelberg, 2007.

[47] Fumio Morito. Characteristics of EB-Weldable Molybdenum and Mo-Re Alloys. *The Journal of The Minerals, Metals & Materials Society (TMS)*, 45(6):54–58, 1993.

[48] M. Nagae, T. Yoshio, J. Takada, and Y. Hiraoka. Improvement in Recrystallization Temperature and Mechanical Properties of a Commercial TZM Alloy through Microstructure Control by Multi-Step Internal Nitriding. *Materials Transactions*, 46(10):2129–2134, 2005.

[49] C. H. Cadden and B. C. Odegard. Refractory metal joining for first wall applications. *Journal of Nuclear Materials*, 283-287(II):1253–1257, 2000.

[50] Mel M. Schwartz. Friction Welding. In *Metals Joining Manual*, pages 6.1–6.51. McGraw-Hill Book Company, 1979.

[51] V. M. Felix and D. A. Wells. Friction welding molybdenum-rhenium alloy. US Patent 5,261,592, 1993.

[52] Steven G. Caldwell, Heinrich Kestler, and Nikolaus Reheis. Secondary Operations and Quality Control for Refractory Metal Powders. In *ASM Handbook*, volume 7, pages 620–624. 2015.

[53] S. Nemat-Nasser, W. G. Guo, and M. Q. Liu. Experimentally-base micromechanical modeling of dynamic response of molybdenum. *Scripta materialia*, 40(7):859–872, 1999.

[54] Gordon R. Johnson and William H. Cook. A constitutive model and data for metals subjected to large strains, high strain rates and high temperatures. In *Proc. of 7th International Symposium on Ballistics*, pages 541–547, 1983.

[55] Frank J. Zerilli and Ronald W. Armstrong. Dislocation-mechanics-based constitutive relations for material dynamics calculations. *Journal of Applied Physics*, 61(5):1816–1825, 1987.

[56] H. Mecking and U.F. Kocks. Kinetics of flow and strain-hardening. *Acta Metallurgica*, 29(11):1865–1875, nov 1981.

[57] Jingyi Cheng, Sia Nemat-Nasser, and Weiguo Guo. A unified constitutive model for strain-rate and temperature dependent behavior of molybdenum. *Mechanics of Materials*, 33(11):603–616, 2001.

[58] F. H. Abed and G. Z. Voyiadjis. A consistent modified Zerilli-Armstrong flow stress model for BCC and FCC metals for elevated temperatures. *Acta Mechanica*, 175(1-4):1–18, 2005.

[59] Jianli He, Fei Chen, Bo Wang, and Luo Bei Zhu. A modified Johnson-Cook model for 10%Cr steel at elevated temperatures and a wide range of strain rates. *Materials Science and Engineering A*, 715:1–9, 2018.

[60] H. Lim, C. C. Battaile, J. D. Carroll, B. L. Boyce, and C. R. Weinberger. A physically based model of temperature and strain rate dependent yield in BCC metals: Implementation into crystal plasticity. *Journal of the Mechanics and Physics of Solids*, 74:80–96, 2015.

[61] C. Y. Gao, W. R. Lu, L. C. Zhang, and H. X. Yan. A constitutive description of the thermo-viscoplastic behavior of body-centered cubic metals. *Materials and Design*, 36:671–678, 2012.

[62] A. M. Lennon and K. T. Ramesh. The thermoviscoplastic response of polycrystalline tungsten in compression. *Materials Science and Engineering A*, 276(1-2):9–21, 2000.

[63] G. P. Škoro, J. R. J. Bennett, T. R. Edgecock, and C. N. Booth. Yield strength of molybdenum, tantalum and tungsten at high strain rates and very high temperatures. *Journal of Nuclear Materials*, 426(1-3):45–51, 2012.

[64] Riqiang Liang and Akhtar S. Khan. A critical review of experimental results and constitutive models for BCC and FCC metals over a wide range of strain rates and temperatures. *International Journal of Plasticity*, 15(9):963–980, 1999.

[65] M. Scapin, C. Fichera, F. Carra, and L. Peroni. Experimental investigation of the behaviour of tungsten and molybdenum alloys at high strain-rate and temperature. *EPJ Web of Conferences*, 94:01021, sep 2015.

[66] C. Chen, H. Yin, I. S. Humail, Y. Wang, and X. Qu. A comparative study of a back propagation artificial neural network and a Zerilli-Armstrong model for pure molybdenum during hot deformation. *International Journal of Refractory Metals and Hard Materials*, 25(5-6):411–416, 2007.

[67] C. Schimpf, T. Mrotzek, and U. Martin. Thermally activated flow stress component of the Mo alloy TZM determined by constitutive models. *International Journal of Refractory Metals and Hard Materials*, 28(6):716–721, 2010.

[68] Martina Scapin. Mechanical characterization and modeling of the heavy tungsten alloy IT180. *International Journal of Refractory Metals and Hard Materials*, 50:258–268, 2015.

[69] Kenneth Levenberg. A method for the solution of certain non-linear problems in least squares. *Quarterly of Applied Mathematics*, 2(2):164–168, jul 1944.

[70] Thomas Williams and Colin Kelley. gnuplot 5.2 - An Interactive Plotting Program, 2017.

[71] Vadim Ivanovich Vill'. *"Friction welding of metals" translated from Russian.* American Welding Society, 1962.

[72] Manufacturing Technology, Inc. *Friction welding*, 1999.

[73] Hans J. Fahrenwaldt, Volkmar Schuler, and Jürgen Twrdek. *Praxiswissen Schweißtechnik.* Vieweg+Teubner, Wiesbaden, 5th edition, 2014.

[74] R. Weiss. Residual stresses and strength of friction welded ceramic/metal joints. *Welding Journal*, 77:115s–122s, 1998.

[75] M. Maalekian, E. Kozeschnik, H. P. Brantner, and H. Cerjak. Comparative analysis of heat generation in friction welding of steel bars. *Acta Materialia*, 56(12):2843–2855, 2008.

[76] R. Nandan, T. DebRoy, and H. K. D. H. Bhadeshia. Recent advances in friction-stir welding – Process, weldment structure and properties. *Progress in Materials Science*, 53(6):980–1023, 2008.

[77] L. E. Murr. A Review of FSW Research on Dissimilar Metal and Alloy Systems. *Journal of Materials Engineering and Performance*, 19(8):1071–1089, feb 2010.

[78] V. R. Dave, M. J. Cola, and G. N. Hussen. Heat generation in the inertia welding of dissimilar tubes. *Welding Journal*, 80(10):246s – 252s, 2001.

[79] KUKA Systems homepage. http://www.kuka-systems.com, November 2014.

[80] Mehran Maalekian. Friction welding – critical assessment of literature. *Science and Technology of Welding and Joining*, 12(8):738–759, nov 2007.

[81] DIN EN ISO 15620 Reibschweißen von metallischen Werkstoffen, 2000.

[82] Horst Czichos and Karl-Heinz Habig. *Tribologie-Handbuch*. 2010.

[83] Dirk Bartel. *Simulation von Tribosystemen*. Vieweg+Teubner, Wiesbaden, 2010.

[84] Dewan M. Nuruzzaman and Mohammad A. Chowdhury. Effect of Load and Sliding Velocity on Friction Coefficient of Aluminum Sliding Against Different Pin Materials. *American Journal of Materials Science*, 2(1):26–31, feb 2012.

[85] M. A. Chowdhury and M. K. Khalil. The effect of sliding speed and normal load on friction and wear property of aluminum. *International Journal of Mechanical and Mechatronics Engineering*, 11(01):45–49, 2011.

[86] Jacek K. Leśniewski and Andrzej Ambroziak. Modelling the friction welding of titanium and tungsten pseudoalloy. *Archives of Civil and Mechanical Engineering*, 15(1):142–150, jul 2014.

[87] F. D. Duffin and A. S. Bahrani. Frictional behaviour of mild steel in friction welding. *Wear*, 26(1):53–74, oct 1973.

[88] Wenya Li, Achilles Vairis, Michael Preuss, and Tiejun Ma. Linear and rotary friction welding review. *International Materials Reviews*, 61(2):71–100, 2016.

[89] X. Li, J. Li, F. Jin, J. Xiong, and F. Zhang. Effect of rotation speed on friction behavior of rotary friction welding of AA6061-T6 aluminum alloy. *Welding in the World*, 62(5):923–930, 2018.

[90] Andrzej Ambroziak. Temperature distribution in friction welded joints of dissimilar refractory metals. *Advances in Manufacturing Science and Technology*, 26(3):39–54, 2002.

[91] Ahmet Can, Mümin Şahin, and Mahmut Küçük. Modelling of Friction Welding. *Unitech Gabrovo International Scientific Conference*, pages 135–142, 2010.

[92] Saleem Ullah Khosa. *Mathematical Modeling of Friction Stir Spot Welding Process*. Doctoral thesis, Graz University of Technology, 2014.

[93] Hanswalter Giesekus. *Phänomenologische Rheologie*. Springer Berlin Heidelberg, 1994.

[94] Q. Z. Zhang, L. W. Zhang, W. W. Liu, X. G. Zhang, W. H. Zhu, and S. Qu. 3D rigid viscoplastic FE modelling of continuous drive friction welding process. *Science and Technology of Welding and Joining*, 11(6):737–743, 2006.

[95] Mehran Maalekian. Thermal Modeling of Friction Welding. *ISIJ International*, 48(10):1429–1433, 2008.

[96] Osborne Reynolds. On the Theory of Lubrication and its Application to Mr. Beauchamp Tower's Experiments, including an Experimental Determination fo the Viscosity of Olive Oil. *Philosophical Transactions of the Royal Society of London*, 177:157–234, 1886.

[97] John A. Roubidoux and Patricio F. Mendez. Innovation in Materials Processing Using Scaling Principles. 2006.

[98] Patricio F. Mendez, Karem E. Tello, and Thomas J. Lienert. Scaling of coupled heat transfer and plastic deformation around the pin in friction stir welding. *Acta Materialia*, 58(18):6012–6026, 2010.

[99] C. M. Sellars and W. J. McTegart. On the mechanism of hot deformation. *Acta Metallurgica*, 14(9):1136–1138, 1966.

[100] Pierre J. Carreau. Rheological Equations from Molecular Network Theories. *Transactions of the Society of Rheology*, 16(1):99–127, mar 1972.

[101] D. Schmicker, K. Naumenko, and J. Strackeljan. A robust simulation of Direct Drive Friction Welding with a modified Carreau fluid constitutive model. *Computer Methods in Applied Mechanics and Engineering*, 265:186–194, oct 2013.

[102] D. Schmicker, K. Naumenko, and J. Strackeljan. A holistic Approach on the Simulation of Rotary-Friction-Welding. pages 148–150. epubli GmbH, 2015.

[103] B. S. Yilbaş and A. Z. Şahin. *Friction Welding: Thermal and Metallurgical Characteristics*. SpringerBriefs in Applied Sciences and Technology. Springer Berlin Heidelberg, Berlin, Heidelberg, 2014.

[104] Mümin Şahin and Cenk Mısırlı. *Mechanical and Metalurgical Properties of Friction Welded Aluminium Joints*. InTech, dec 2012.

[105] Florian Pixner. *Rotary Friction Welding (RFW) of Molybdenum*. Master's thesis, Graz University of Technology, 2018.

[106] M. Kessler, C. Suenger, C. Wunderling, and M. F. Zaeh. Simulation of Inertia Friction Welding of Tempering Steel AISI 4140. In *Mathematical Modelling of Weld Phenomena 11*, Graz, 2015. Verlag der Technischen Universität Graz.

[107] Florian Pixner, Markus Stütz, Josef Wagner, Nikolaus Reheis, and Norbert Enzinger. Comparing Molybdenum and Steel in Rotary Friction Welding using an FSW Machine. In *22. Erfahrungsaustausch Reibschweissen*. GSI SLV München, 2017.

[108] Helmut Schultz. *Electron Beam Welding*. Elsevier, 1994.

[109] Ulrich Dilthey. *Schweißtechnische Fertigungsverfahren 1: Schweiß- und Schneidtechnologien*. Springer Berlin Heidelberg, 3rd edition, 2006.

[110] Christopher Dawes. *Laser welding: A practical guide*. Abington Publishing, Cambridge, 1992.

[111] V. Adam, U. Clauß, D. von Dobeneck, T. Krüssel, and T. Löwer. *Elektronenstrahlschweißen – Grundlagen einer faszinierenden Technik*. pro-beam AG & Co. KGaA, 2011.

[112] A. Chatterjee, S. Kumar, R. Tewari, and G. K. Dey. Welding of Mo-Based Alloy Using Electron Beam and Laser-GTAW Hybrid Welding Techniques. *Metallurgical and Materials Transactions A*, 47(3):1143–1152, mar 2016.

[113] C.-T. Chi, C.-G. Chao, T.-F. Liu, and C.-C. Wang. Optimal parameters for low and high voltage electron beam welding of AZ series magnesium alloys and mechanism of weld shape and pore formation. *Science and Technology of Welding and Joining*, 13(2):199–211, feb 2008.

[114] Peter Petrov and Svilen Sabchevski. Parameters Used for Electron Beam Welding – A Comparative Study. In *Proc. of 8th International Conference on Beam Technology*, number 2, pages 90–94, 2010.

[115] Daniel Rosenthal. The Theory of Moving Sources of Heat and Its Application to Metal Treatments. *Transactions of the American Society for Metals ASME*, 68:849–865, 1946.

[116] Florian W. Stiefler. *Einfluss der Oberflächenrauheit auf die Nahtqualität beim Elektronenstrahlschweißen*. Master's thesis, Graz University of Technology, 2014.

[117] J. L. Barreda, F. Santamaría, X. Azpiroz, A. M. Irisarri, and J. M. Varona. Electron beam welded high thickness Ti6Al4V plates using filler metal of similar and different composition to the base plate. *Vacuum*, 62(2-3):143–150, 2001.

[118] J. P. Oliveira, B. Panton, Z. Zeng, C. M. Andrei, Y. Zhou, R. M. Miranda, and F. M. Braz Fernandes. Laser joining of NiTi to Ti6Al4V using a Niobium interlayer. *Acta Materialia*, 105:9–15, 2016.

[119] N. Enzinger, P. Loidolt, C. Wiednig, M. Stütz, and C. Sommitsch. Electron beam welding of thick-walled copper components. *Science and Technology of Welding and Joining*, 22(2):127–132, 2016.

[120] M. Stummer, M. Stütz, A. Aumayr, and N. Enzinger. Electron beam welding of copper using plasma spraying for filler metal deposition. *Welding in the World*, pages 1–10, aug 2018.

[121] J. Zhao, B. Zhang, X. Li, and R. Li. Effects of metal-vapor jet force on the physical behavior of melting wire transfer in electron beam additive manufacturing. *Journal of Materials Processing Technology*, 220:243–250, 2015.

[122] ISO 15609-3 Specification and qualification of welding procedures for metallic materials – Welding procedure specification – Part 3: Electron beam welding, 2004.

[123] Marie Kolarikova, Kolarik Ladislav, and Petr Vondrous. Welding of Thin Molybdenum Sheets by EBW and GTAW. *Annals of DAAAM*, 23(1):1005–1008, 2012.

[124] J. Wadsworth, G. R. Morse, and P. M. Chewey. The Microstructure and Mechanical Properties of a Welded Molybdenum Alloy. *Materials Science and Engineering*, 59:257–273, 1983.

[125] B. V. Cockeram, E. K. Ohriner, T. S. Byun, M. K. Miller, and L. L. Snead. Weldable ductile molybdenum alloy development. *Journal of Nuclear Materials*, 382(2-3):229–241, dec 2008.

[126] T. Wang, Y. Zhang, S. Jiang, X. Li, B. Zhang, and J. Feng. Stress relief and purification mechanisms for grain boundaries of electron beam welded TZM alloy joint with zirconium addition. *Journal of Materials Processing Technology*, 251(August 2017):168–174, 2018.

[127] Y. Zhang, T. Wang, S. Jiang, B. Zhang, Y. Wang, and J. Feng. Microstructure evolution and embrittlement of electron beam welded TZM alloy joint. *Materials Science and Engineering A*, 700(April):512–518, 2017.

[128] Z. Sun and R. Karppi. The application of electron beam welding for the joining of dissimilar metals: an overview. *Journal of Materials Processing Technology*, 59:257–267, 1996.

[129] Paul Burgardt, Stanley W. Pierce, and Matthew John Dvornak. Definition of Beam Diameter for Electron Beam Welding. Technical report, Los Alamos National Laboratory, 2016.

[130] DIN EN ISO 9692-1 Welding and allied processes – Types of joint preparation – Part 1: Manual metal arc welding, gas-shielded metal arc welding, gas welding, TIG welding and beam welding of steels, 2003.

[131] Christian Bonnet. Welding Products. In Régis Blondeau, editor, *Metallurgy and Mechanics of Welding: Processes and Industrial Applications*, chapter 5, pages 169–206. ISTE Ltd, London, UK, 2nd edition, 2008.

[132] Diogo Oliveira. *Electron Beam Welding of TZM Plates*. Master's thesis, Universidade Nova de Lisboa, 2015.

[133] T. Kadokura, Y. Hiraoka, Y. Yamamoto, and K. Okamoto. Change of Mechanical Property and Fracture Mode of Molybdenum by Carbon Addition. *Materials Transactions*, 51(7):1296–1301, 2010.

[134] Plansee SE. *TZM sheet product specification*, August 2018. PSE-605-PS-048 Rev. 01.